NUMERICAL MODELING OF THE DYNAMICS AND HEAT TRANSFER OF IMPACTING SPRAYS FOR A WIDE RANGE OF PRESSURES

by

Roy Jean Issa

B.S. in Mechanical Engineering, University of Tennessee, 1988

M.S. in Mechanical Engineering, University of Tennessee, 1989

Submitted to the Graduate Faculty of

School of Engineering in partial fulfillment

of the requirements for the degree of

Doctor of Philosophy

University of Pittsburgh

2003

UNIVERSITY OF PITTSBURGH

SCHOOL OF ENGINEERING

This dissertation was presented

by

Roy Jean Issa

It was defended on

September 25, 2003

and approved by

Shi-Chune Yao, Ph.D., Professor, Mechanical Engineering, Carnegie Mellon University

Giovanni Galdi, Ph.D., Professor, Mechanical Engineering

Laura Schaefer, Ph.D., Assistant Professor, Mechanical Engineering

Dissertation Director: Minking Chyu, Ph.D., Professor & Chairman, Mechanical Engineering

ABSTRACT

NUMERICAL MODELING OF THE DYNAMICS AND HEAT TRANSFER OF IMPACTING SPRAYS FOR A WIDE RANGE OF PRESSURES

Roy Jean Issa, Ph.D.

University of Pittsburgh, 2003

A numerical model is developed to simulate the impingement of liquid sprays on surfaces heated at temperatures ranging from nucleate to film boiling. The droplets are modeled in the Lagrangian frame of reference, and are dispersed stochastically in the continuous gas phase. The model is based on the fundamental basics of single droplet impingements extended to full sprays, where the overall heat transfer process is broken down into its basic components: conduction associated with the droplet contact, bulk air convection, and surface radiation. Droplet dynamics at the wall are modeled based on an empirical correlation relating the droplet incoming to outgoing Weber number. Droplet contact heat transfer is modeled using an effectiveness parameter for the heat transfer that is a function of the droplet Weber number. This attempt of numerically modeling the droplet-wall dynamics with multiple wall collisions and the droplet contact heat transfer has not been addressed before in a numerical model. Simulations are

presented for: single-stream droplet impactions, multiple-streams droplet impactions, and conical sprays.

The model is tested at atmospheric pressure using experimental data for nozzles that dispense non-uniform droplets. Favorable comparison with the test data is demonstrated. The model capability is then extended to simulate high and sub-atmospheric ambient pressure conditions with a proper accounting of the droplet-wall interaction and air-mist heat transfer mechanism. At high and sub-atmospheric pressures, the model was tested against experiments for single stream impactions at various pressures.

Spray simulation conducted for a wide range of pressures reveals the following important issues regarding to the droplet dynamics, heat transfer and vaporization: 1) At higher pressures, the larger the droplet size, the better is the droplet-wall impaction, while for sub-atmospheric pressures, larger droplets have a detrimental effect due to their ballistic impaction. 2) At higher pressures, the Leidenfrost point shifts to a higher temperature that leads to an increase in the droplet wetting capability, and to a higher heat transfer effectiveness. 3) At higher pressures, more vapor is generated from each droplet impaction on the surface, resulting also in an increase in the heat transfer effectiveness.

DESCRIPTORS

Contact heat transfer

Droplet coefficient of restitution

Droplet rebound

Droplet sub-cooling

Droplet Weber number

Heat flux

Heat transfer effectiveness

High-pressure conditions

Non-wet cooling

Spray

Sub-atmospheric pressure conditions

Thermal boundary layer

Wall impaction

Wet cooling

TABLE OF CONTENTS

LIST OF FIGURES

NOMENCLATURE

Notation	Description	Units
A_d	Droplet cross-sectional area	m^2
C_D	Drag coefficient	
c	Target specific heat constant	J/kg.K
$c_{p,d}$	Droplet specific heat constant	J/kg.K
$c_{p,v}$	Vapor specific heat constant	J/kg.K
d	Droplet diameter	μm (or mm)
$\bar{d}$	Average droplet diameter in the Rosin-Rammler distribution	μm (or mm)
d_{max}	Droplet maximum spread diameter	μm (or mm)
d_{noz}	Nozzle orifice diameter	mm (or m)
dT	Change in temperature	^oC
dt	Time step	s
Y_{noz}	Nozzle vertical distance from the plate	mm
E_{ki}	Droplet kinetic energy at location i	J
E_{si}	Droplet surface energy at location i	J
E_{diss}	Energy viscous dissipation	J
e_n	Normal coefficient of restitution	
e_t	Tangential coefficient of restitution	
F	Rate of momentum exchange term	N

F_D	Drag force coefficient	1/s
$\vec{F}$	External force per unit droplet mass acting on the droplet	m/s^2
G	Liquid mass flux	$kg/m^2.s$
$\vec{g}$	Gravitational acceleration	m/s^2
H	Droplet enthalpy	J
h	Convection heat transfer coefficient	$W/m^2.K$
h_a	Air convection heat transfer coefficient	$W/m^2.K$
I	Radiation intensity	$W/m^2.sr$
i	Index notation	
j	Index notation	
k_a	Air thermal conductivity	W/m.K
M	Rate of mass exchange term	kg/s
M_d	Mass fraction of droplets with diameter greater than d	
m	Target mass	kg
m_d	Mass of the droplet in the control volume	kg
m_{do}	Initial mass of the droplet	kg
m_v	Vapor mass	kg
$\dot{m}_a$	Air mass flow rate	kg/s
$\dot{m}_d$	Mass flow rate of the droplet	kg/s
$\dot{m}_{do}$	Initial mass flow rate of the droplet	kg/s
$\dot{m}_w$	Water mass flow rate	kg/s
$\overline{m}_d$	Average mass of the droplet in the control volume	kg

N	Frequency of droplet impingements	drops/s
n	Spread parameter for Rosin-Rammler distribution	
P	Operating pressure	atm (or Pa)
P_c	Critical pressure	atm (or Pa)
Pr_a	Air Prandtl number	
Q	Rate of heat exchange term	J/s
q_c	Droplet contact heat flux	W/m^2
q_{CHF}	Critical heat flux	W/m^2
q_{min}	Minimum heat flux (@ Leidenfrost temperature)	W/m^2
$q_{partial}$	Droplet heat transfer for partial evaporation	J
$q_{100\%}$	Droplet heat transfer for complete evaporation	J
R	Gas constant	kJ/kg.K
Re	Reynolds number	
S_Φ	General source term	
$S_{\Phi d}$	Source term due to the presence of the droplets	
T_a	Air temperature	^oC
T_{CHF}	Temperature at the critical heat flux point	^oC
T_d	Droplet temperature	^oC
T_{Leiden}	Leidenfrost temperature	^oC
T_{liq}	Liquid temperature	^oC
T_{ref}	Reference temperature for enthalpy	^oC
T_{sat}	Liquid saturation temperature	^oC
T_w	Wall temperature	^oC

t_c	Time taken by the droplet to reach maximum spread at the wall	s
$\vec{U}$	Transport velocity vector	m/s
$\vec{v}_d$	Droplet velocity vector	m/s
$\vec{v}_a$	Air velocity vector	m/s
v_i	Droplet impinging velocity at surface	m/s
$v_{i,n}$	Normal component of the droplet impinging velocity	m/s
$v_{i,t}$	Tangential component of the droplet impinging velocity	m/s
v_o	Droplet rebounding velocity at surface	m/s
$v_{o,n}$	Normal component of the droplet rebounding velocity	m/s
$v_{o,t}$	Tangential component of the droplet rebounding velocity	m/s
We	Droplet Weber number	
We_{cr}	Critical Weber number at which droplet disintegration occurs	
We_n	Normal impinging droplet Weber number	
x	x-coordinate	
y	y-coordinate	
z	z-coordinate	

Greek Symbols

α	Surface inclination angle	deg.
ε	Droplet contact heat transfer effectiveness	
ε_d	Droplet emissivity	
θ	Droplet contact angle at the surface	deg.

θ_i	Droplet impinging angle (angle between the droplet motion direction and the normal to the surface at the point of impact)	deg.
θ_o	Droplet rebounding angle	deg.
θ_R	Radiation temperature	K
θ_s	Nozzle spray angle (spray cone angle)	deg.
ΔH	Total heat removal of the droplet	J/kg
Δh_{fg}	Latent heat of vaporization	J/kg
Δm_d	Change in the mass of the droplet	kg
Δt	Time step	s
ρ_a	Air density	kg/m^3
ρ_d	Droplet mass density	kg/m^3
μ_d	Droplet dynamic viscosity	kg/m.s
ν_a	Air kinematic viscosity	m^2/s
σ	Stefan-Boltzmann constant	$W/m^2.K^4$
σ_d	Droplet surface tension	N/m
Γ	Diffusivity	m^2/s
Φ	Dependent variable	
ϕ	Dissipation function	
$\forall$	Droplet volume	m^3
δ	Droplet height	m
β_{max}	Droplet maximum spread at the wall	
∇	Gradient operator	

Subscripts

1	before droplet impaction (also is used to refer to large droplets)
2	at droplet maximum spread on the wall (also is used to refer to small droplets)

ACKNOWLEDGEMENTS

I would like to thank Professor Minking Chyu for his guidance during my doctoral studies at the University of Pittsburgh. I would like to express my appreciation to Professor S. C. Yao at Carnegie Mellon University for providing me with a great deal of support throughout my research years. His many helpful discussions and valuable comments are greatly appreciated. Thanks also go to Professors Giovanni Galdi and Laura Schaefer for taking time to serve on my Ph.D. dissertation committee. My deepest gratitude and everlasting appreciation goes to my wonderful parents, John and Viola Issa. Without their continuous support and many encouragements it would have been impossible for me to go through this program. I owe my doctorate degree to them.

1.0 INTRODUCTION

Intense cooling methods have been widely used in many industrial applications, especially those requiring rapid cooling from high temperatures. In the hot strip rolling mill, temperature control of the strip on the runout table continues to be the subject of research after years of experimental investigations and experience with different cooling systems. The metallurgical properties of the strip and the surface oxide formation depend greatly on the manner in which heat is extracted from the strip. In the conventional hot strip mill where medium to thin strips are produced (2-10 mm in thickness), cooling on the runout table is normally achieved using laminar water jets [1-4]. In spite of their low cooling efficiency, such methods are necessary because they provide sufficient force for the water to penetrate through the vapor layer covering the strip, which normally travels at relatively high speeds. However, these cooling methods are not appropriate for very thin strips of metal where the high impacting force by the jet may cause a detrimental effect on the strip shape in addition to the low cooling efficiency.

In thin strip casting (1-3 mm in thickness) a new type of cooling system based on Mist Jets promises to be the most efficient method for cooling due to the increase in the surface contact area between the liquid and the metal. Cooling by mist jets has several other advantages. It provides uniformity in cooling that leads to improvement in the material properties and the flatness of the rolled product. It is also cost effective because it optimizes the amount of water consumption in the mill, and reduces the expenses associated with water recycling and filtration. In order to provide flexibility in controlling the strip temperature, mist headers may also be

connected to hydraulic actuators, shown in Figure 1.1, that rotate the headers to various angular positions to maintain the strip within a desired temperature range.

Mist cooling has also found application in other areas such as gas turbines (Figure 1.2) [5-8], and electronic chips (Figure 1.3) [9-11]. Experiments have been conducted on the internal cooling of gas turbine airfoils by injecting mist with the compressed air. The results show significant enhancement in the cooling process, whereas an injection of 5% water mist in air can enhance the heat transfer by about 20-30% [5]. The advantage of the air-mist can result in a reduction in the consumption of the compressed air that is conventionally required to cool the airfoils by almost 50%. Experimental studies are also being conducted to enhance the cooling of computer chips [10]. Current computer chips generate heat fluxes between 50-100 W/cm^2, while high performance computer chips in future are projected to experience power densities greater than 100 W/cm^2. Therefore, there is a continuous demand on the technology providing the most adequate cooling. Cooling by air convection has its limitation. This is because forced air convection at room temperature has a maximum heat flux between 2-3 W/cm^2. Although air-cooling continues to be the commercially and widely used method for cooling electronic chips, significant research have shown that higher heat fluxes can be accommodated through the use of mist cooling. This is because water has superior thermo-physical properties. Depending on the liquid mass flux, mist cooling can generate cooling heat fluxes between 100-1200 W/cm^2 at atmospheric pressure conditions.

In spray cooling, the cooling medium is a mixture of air and water droplets. An air stream of high velocity accelerates the water droplets. A schematic of a typical spray nozzle is shown in Figure 1.4. A wide variety of commercial air-mist nozzles can be obtained from Spraying Systems [12]. Such nozzles contain two flow chambers: a pressurized liquid water chamber,

and a pressurized air chamber. The discharging water and air streams collide towards the center of the opening of the conical cap. The pressurized air surrounds and impinges on the liquid flowing from the orifice and thus atomizes the liquid film. There are several factors that affect the droplet size such as the spraying pressure, and the air-to-liquid flow capacity. Smaller droplet sizes in the spray can be achieved by either increasing the air pressure while decreasing the liquid pressure, or by increasing the air flow rate while decreasing the liquid flow rate. An increase in the pressure difference between the liquid and air results in an increase in the relative velocity between them. This leads to an increase in the shear force acting on the liquid film, which produces finer droplets. A similar effect can be seen by increasing the air-to-liquid flow rate ratio.

Spray cooling heat transfer has been mainly experimental in nature. A substantial amount of experiments on mist cooling has been performed using single droplet impaction and full sprays. Pederson [13], Kendall and Rohsenow [14], Senda et al. [15], and McGinnis and Holman [16] have studied single droplet heat transfer. Their findings were very valuable in understanding the cooling effectiveness produced from single impaction. The authors investigated a wide range of surface temperatures that extended from the nucleate boiling to the film boiling range. Other researchers including Sozbir and Yao [17], Chang and Yao [18], Ortiz and Gonzalez [19], Ohkubo and Nishio [20], and Pais et al. [21] have made heat transfer measurements using full sprays. They used air-mist nozzles that produced a spectrum of droplet diameters. In all those experiments, both for single droplet impaction and air-mist sprays, it was found that the heat transfer is dependent on important parameters that include the droplet size, surface temperature, and the droplet Weber number. Also, all the above experiments were conducted at an atmospheric pressure condition.

A very limited number of experiments have been performed at either high ambient pressures or sub-atmospheric pressures. Unfortunately, none of those experiments were conducted for full spray conditions. Those experiments have been performed essentially either for single droplet impingements, or for a single sessile (stationary) droplet on a hot surface. Halvorson [22] conducted experiments for a single stream of impinging water droplets in the nucleate boiling heat transfer mode at ambient pressures extending from 0.1 atm to 2 atm. For heat transfer in the film boiling range, Testa and Nicotra [23] studied single droplet impingement at sub-atmospheric pressures (0.1-1 atm), while Emmerson and Snoek [24, 25] studied the evaporation of stationary water droplets on heated surfaces at pressures ranging from 1 to 5 atm.

Very few models that can predict the spray behavior have been developed. The existing models do not consider the droplet bouncing behavior at the wall, but only track the droplets up to the point where they make contact with the surface. They also do not calculate for the partial evaporation and the heat transfer effectiveness as the droplets impact. In the research for diesel spray impingement onto the cylinder walls, experiments have been conducted using high-speed photography to examine the distribution pattern of the spray and the fundamental spray parameters such as the wall spray height, and the wall spray radius. Sakane et al. [26], Mirza [27], Katsura et al. [28], Senda et al. [29], Saito et al. [30], and Guerrasi and Champoussin [31] have all conducted experiments on diesel spray-wall interaction. The common disadvantage made by those researchers is that their studies were mostly conducted at room surface temperatures. In addition, the models were often based on experiments conducted at atmospheric pressure. Therefore, a model that can handle the effect of a wide range of pressures (sub-atmospheric, atmospheric, and high-pressure) is of tremendous value to the spray cooling research. Also, the lack of sufficient experimental data for high pressure and sub-atmospheric

applications makes it very valuable to have a model that can realistically predict the heat transfer process and the parameters that affect it.

There are two primary objectives for this research. The first objective is to establish a numerical model to study the mist cooling on heated metallic surfaces at atmospheric conditions. The model should be able to simulate for various boundary conditions, the droplet dynamic behavior when contacting the wall, and the droplet wall contact heat transfer. The attempt to simulate the dynamic behavior of the droplets with multiple droplet-wall collisions, and the effect of the droplet impinging Weber number on the droplet heat transfer effectiveness has not been addressed before in a numerical model. The current model is to be based on the fundamental basics of single droplet impaction extended to full sprays, where the overall heat transfer process can be broken down into its basic component processes: conduction associated with the droplet contact with the heated surface, bulk air convection, and radiation from the surface. The model would then be validated by comparing the numerical simulations against experimental data. The second objective is to extend the simulation capability to high and sub-atmospheric pressures with a proper accounting of the droplet-wall interaction and air-mist heat transfer mechanism. The understanding of the droplet dynamics and heat transfer at high and sub-atmospheric pressures is scarce. The challenges behind this research are to obtain a valuable basic understanding of the parameters that affect the heat transfer enhancement over the wide range of operating pressures.

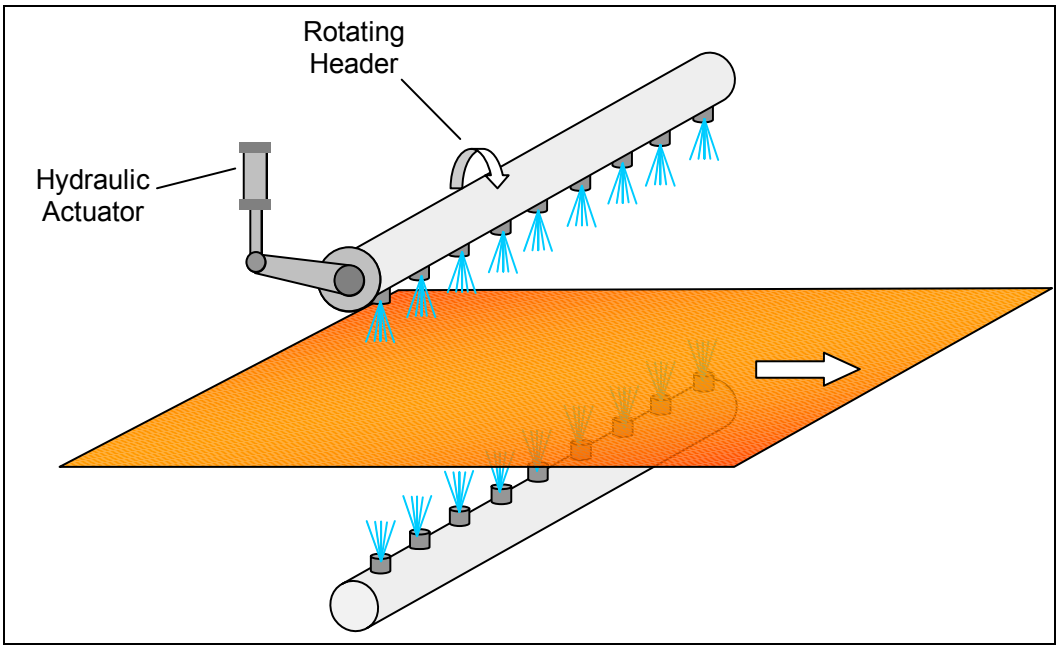

Figure 1.1 Spray cooling in the hot strip mill

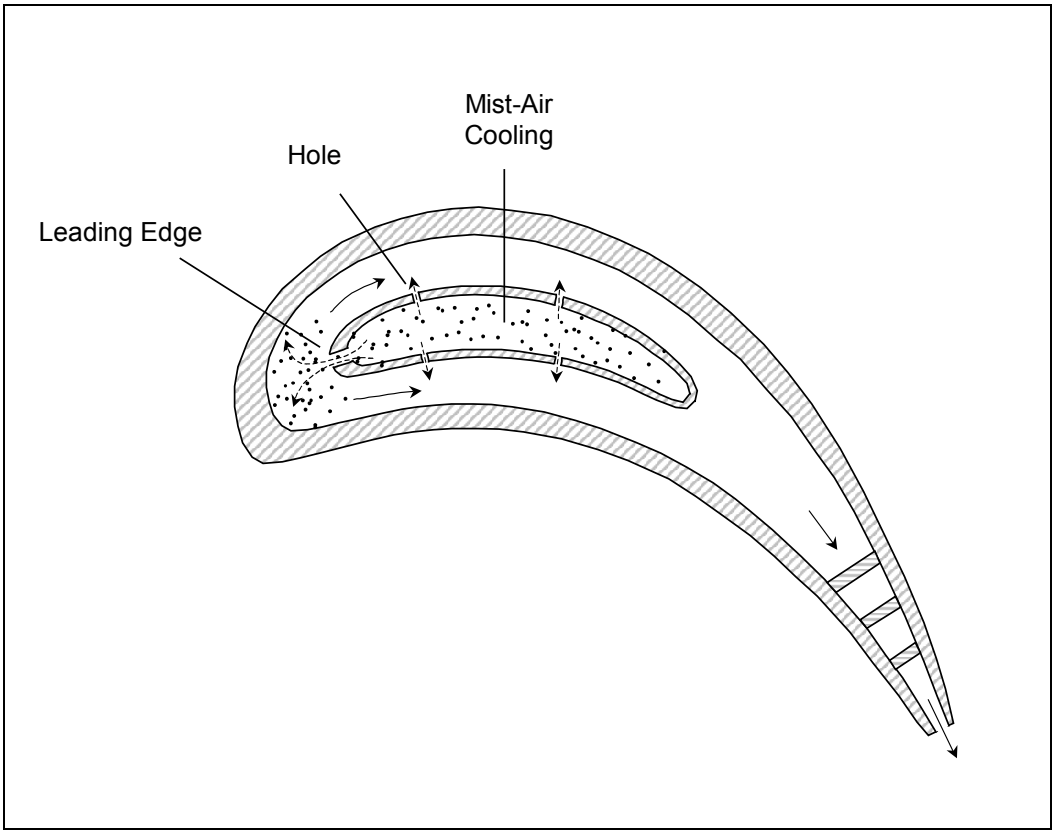

Figure 1.2 Mist cooling of the airfoil in a gas turbine

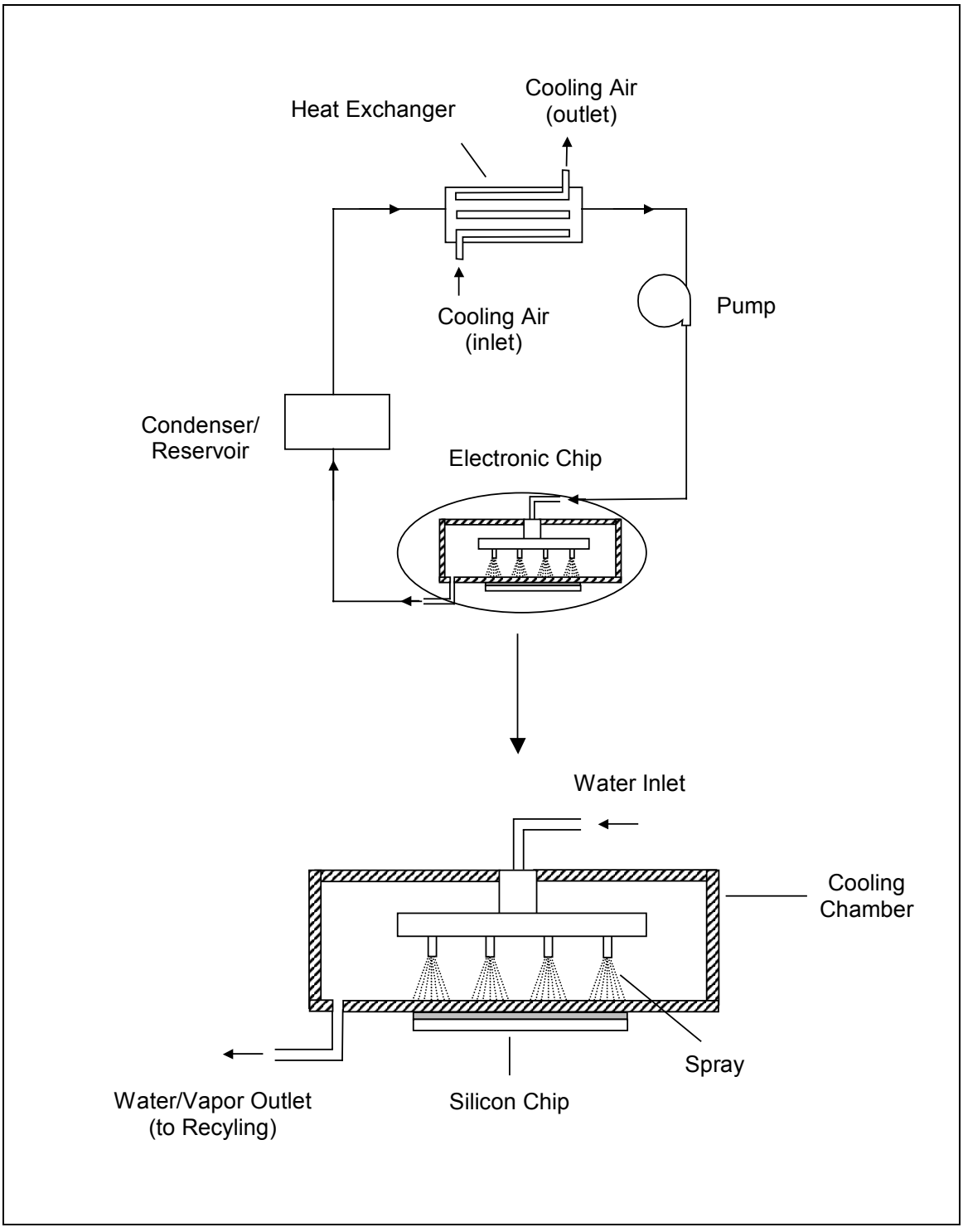

Figure 1.3 Closed loop spray cooling of electronic chips

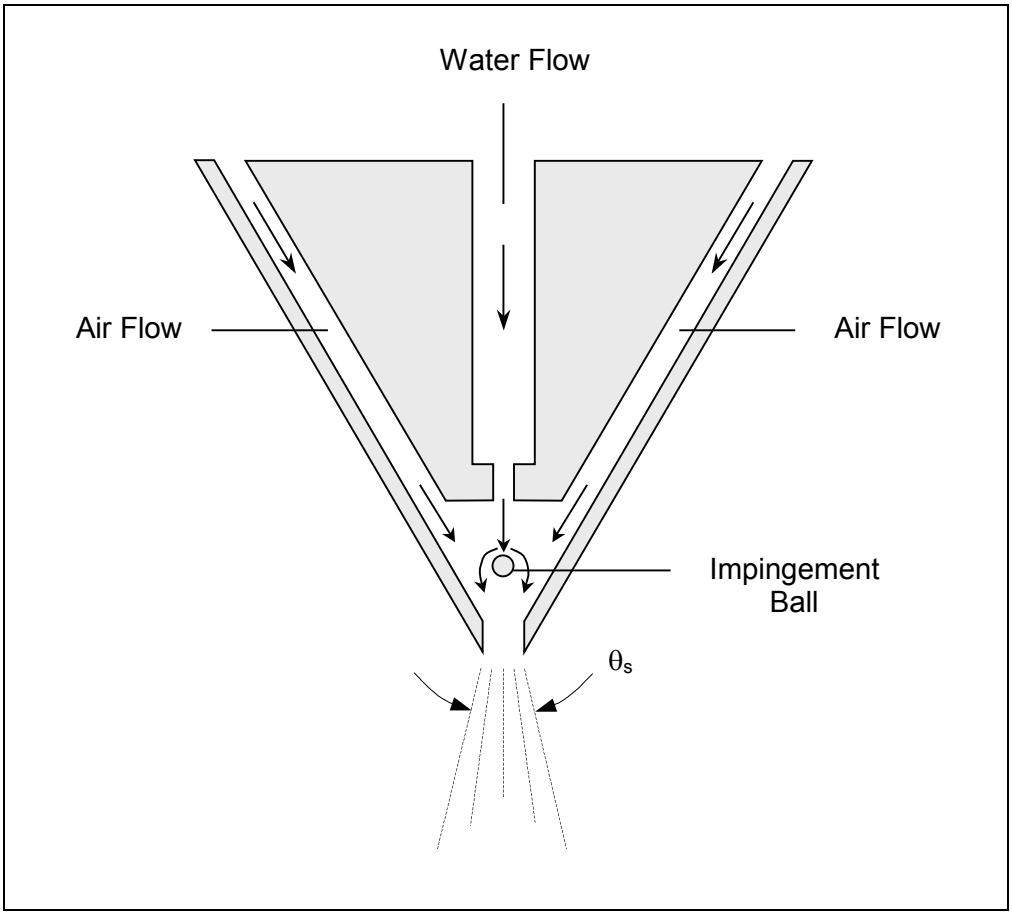

Figure 1.4 Configuration of a spray nozzle

2.0 DROPLET INTERACTION WITH THE WALL

2.1 Modes of Droplet Impaction

Droplet impingement on the surface can be classified according to the following three main modes of impaction (as seen in Figure 2.1):

a) Stick Mode:

This occurs when the droplet approaches the surface with a very low impinging Weber number. On impact, the droplet would adhere to the surface in a nearly spherical form [32].

b) Rebound Mode:

In this mode, the droplet bounces off the wall after impact. The droplet exhibits both elastic and plastic behaviors. For very small impact energies, the droplet reflects perfectly elastically at the wall. This means that the reflection angle is approximately equal to the impinging angle. As the droplet impact energy increases, the droplet starts to exhibit plastic behavior at the wall, and the reflection angle becomes considerably larger than the impinging angle. High-speed photography for droplet impingement on a heated surface reveals the following [33, 34, 35]. During impaction, the droplet spreads radially on the heated surface in the form of a flattened disk. After the droplet reaches a maximum spread diameter, it then begins to recoil backwards towards its center. This happens because of the surface tension effect at the droplet periphery. The droplet then rebounds from the surface as a long and narrow mass. In experiments [33, 34, 35], it is seen that as the droplet bounces off the surface, the droplet shape changes due to the

difference in the velocity between its top and bottom parts. The droplet will rebound without breaking up as long as the impinging droplet Weber number is less than the critical Weber number at which the droplet will start to disintegrate.

c) Break-up Mode:

Break-up mode occurs when the droplet impacts the surface at an incoming Weber number equal or greater than the critical Weber number. It has been also found that the number of disintegrated droplets increases with the increase in the Weber number [36, 37]. This is because the impact energy and the deformation of the droplet increase with the Weber number. Experimental results show the droplet disintegration to occur in one of the following two ways [36, 37]:

- The droplet can break up into smaller parts during the recoil process, but subsequently coalesces with each other, and rebounds. This occurs for low Weber numbers, but above the critical one.
- The droplet can disintegrate during the spreading process, and the disintegrated parts move outwards away from each other. This type of break-up mode occurs for impinging Weber numbers that are much higher than the critical one.

The surface temperature can have a strong influence on the droplet breakup [38]. For instance, the boiling regime can induce breakup even at a very low impacting energy. In this case, droplets would disintegrate due to the rapid liquid boiling on the hot wall accompanied by the formation of gas bubbles blowing through the liquid droplet. If the conditions are favorable for droplets to break-up, then depending on the heat transfer mode, various secondary droplet sizes can be formed. Nucleate boiling results in very fine secondary droplet formation, while

transition boiling results in fine droplet formation, and film boiling results in large size droplet formation.

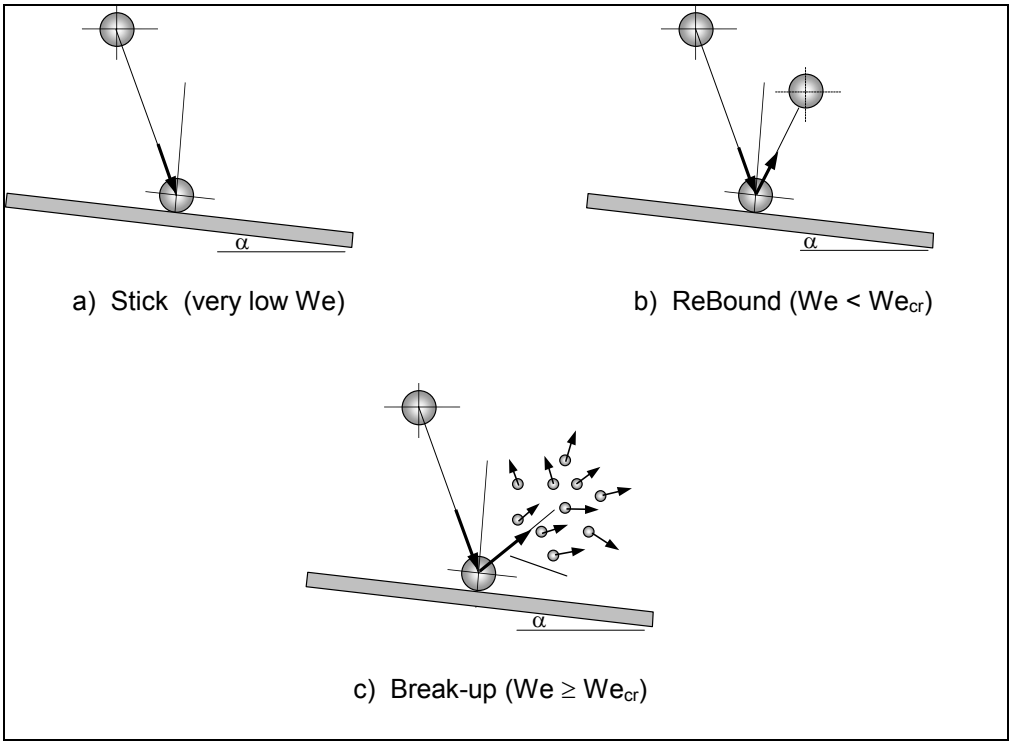

Figure 2.1 Modes of droplet impaction at the wall

2.2 The Influence of the Droplet Weber Number

There are several factors that influence the droplet impaction mode at the wall as will be discussed in the next section. However, one factor, which is the Weber number, is considered to be the governing parameter for the droplet deformation. The droplet Weber number is a measure of the relative importance of the droplet kinetic energy to its surface energy. The droplet kinetic energy is a function of the droplet speed and its diameter. Figure 2.2 shows two droplets of the same liquid material with identical impinging Weber numbers. The smaller droplet, which has a

diameter d_2 impinges on the surface with a higher speed than the droplet with diameter d_1, but the net result after the impact is that both droplets would deform, spread and rebound from the wall in a similar fashion. Droplets with higher impact energies tend to spread more at the surface. The droplet spread is influenced by its surface tension. A decrease in the droplet surface tension results in an increase in the droplet spread at the wall, and vise versa.

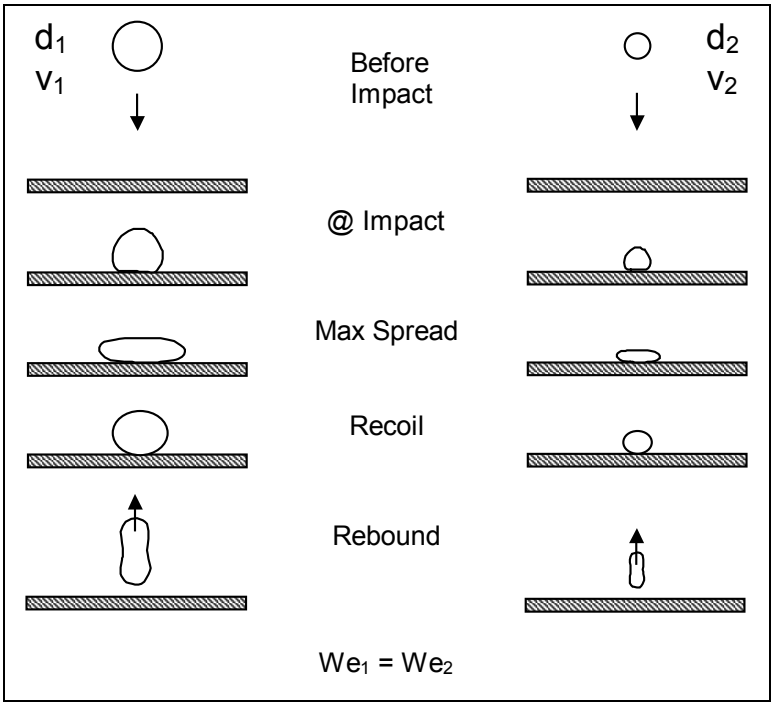

Figure 2.2 The influence of Weber number on droplet rebound

2.3 Modeling of the Droplet Rebound at Atmospheric Pressure

The change in the droplet speed and its direction during the impaction at the wall (shown in Figure 2.3) can be quantitatively measured by the normal and tangential coefficient of restitution. The normal component defines the amount of momentum in the normal direction that is retained after the impact, while the tangential component defines the amount of momentum that is retained in the horizontal direction. The normal and tangential coefficients of restitution can be expressed as follows:

$$e_n = \frac{v_{o,n}}{v_{i,n}} \quad , \quad e_t = \frac{v_{o,t}}{v_{i,t}} \tag{2-1}$$

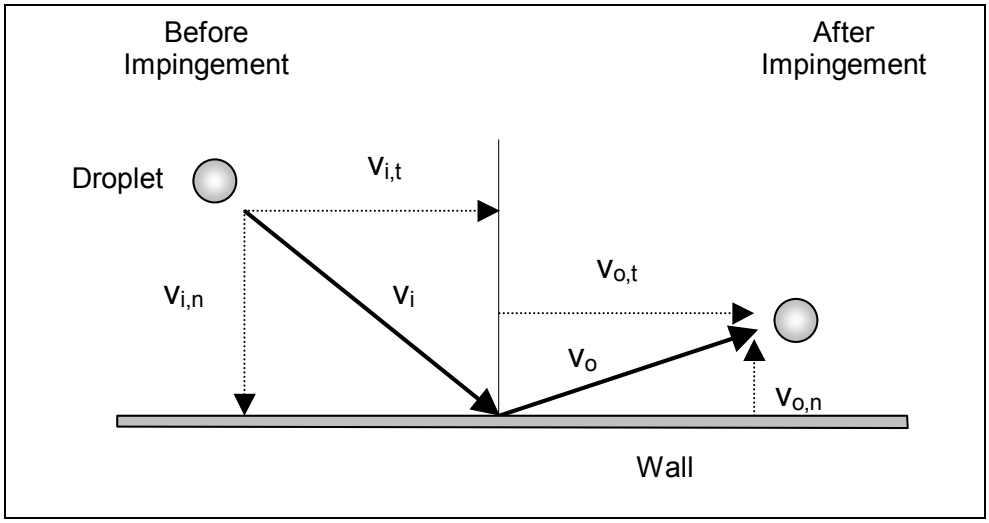

Figure 2.3 Schematic of droplet impingement on the wall

Wachters and Westerling [35], Naber and Farrell [38], Hatta et al. [37], and Karl et al. [39], have experimentally investigated the normal coefficient of restitution of impinging droplets. Figure 2.4 explains the nature of impact dynamics [35]. At low incoming normal Weber

numbers, the droplets rebound elastically from the wall. As the approach velocity is increased, the normal velocity component of the rebounding droplets decreases sharply because of the radial spread of the droplets over the heated surface. As the rebound velocity becomes very low, the droplet impact mode becomes close to plastic. Only Naber and Farrell [38] studied the normal and tangential coefficient of restitution. They measured the normal and tangential ejected Weber number as a function of the impinging normal Weber number.

The critical Weber number at which droplet disintegration occurs is dependent upon the surface material properties especially thermal conductivity, surface roughness, surface temperature, and droplet impingement angle. Wachters and Westerling [35] investigated droplet impaction on a polished gold surface heated to 400 ^{o}C, and inclined at 30^{o} angle to the incoming droplets of 2 mm in diameter. The critical Weber number was about 80. Hatta et al. [37] studied droplet collision on Inconel alloy and stainless steel plates heated to 500 ^{o}C using water droplets of diameters between 300 and 700 μm. The critical Weber number was 50 for the Inconel alloy plate and 45 for the stainless steel plate. Karl et al. [39] used water with droplet diameters of 90 μm impinging at angles ranging from 60^{o} to 80^{o}. For impinging angles less than 70^{o}, the critical Weber number remained constant, while for angles greater than 70^{o}, the critical Weber number increased due to friction. Naber and Farrell examined water droplets with 105 and 310 μm diameters impinging on a stainless steel surface beaded to a uniform surface roughness and heated to temperatures below and above the Leidenfrost point. Their observed critical Weber number was 24.

Experimental data gathered from the above sources are presented in Figure 2.5. They show the relationship between the droplet normal coefficient of restitution (ratio of rebounding to

impinging normal velocity) and the impinging normal Weber number. The following empirical expression is a best fit through the data:

$$e_n = 1 - 0.1630 We_n^{0.3913} \tag{2-2}$$

Where,

$$We_n = \frac{\rho_d v_{i,n}^2 d}{\sigma_d} \tag{2-3}$$

Experiments performed by Karl and Frohn [40] for surfaces heated above the Leidenfrost temperature show the loss of the droplet momentum tangential to the wall to be negligible compared to the loss of the momentum normal to the wall. They show that the loss of the tangential momentum is only about 5%. Naber and Farrell [38] showed the ejected tangential Weber number remained zero for impinging normal Weber numbers up to 20, and increased to 0.4 for an impinging normal Weber number of 70. Recent models for fuel spray-wall impingement in diesel engines have assumed a fixed value of 0.71 for the tangential coefficient of restitution [41]. This was based on the method developed by Matsumoto and Saito [42] for small particles impinging on a wetted surface. In the current study, Karl and Frohn assumption of a negligible loss in the droplet tangential momentum at temperatures close to the Leidenfrost was adopted; thus, the droplet tangential coefficient of restitution was assumed to be 1 in all the simulations.

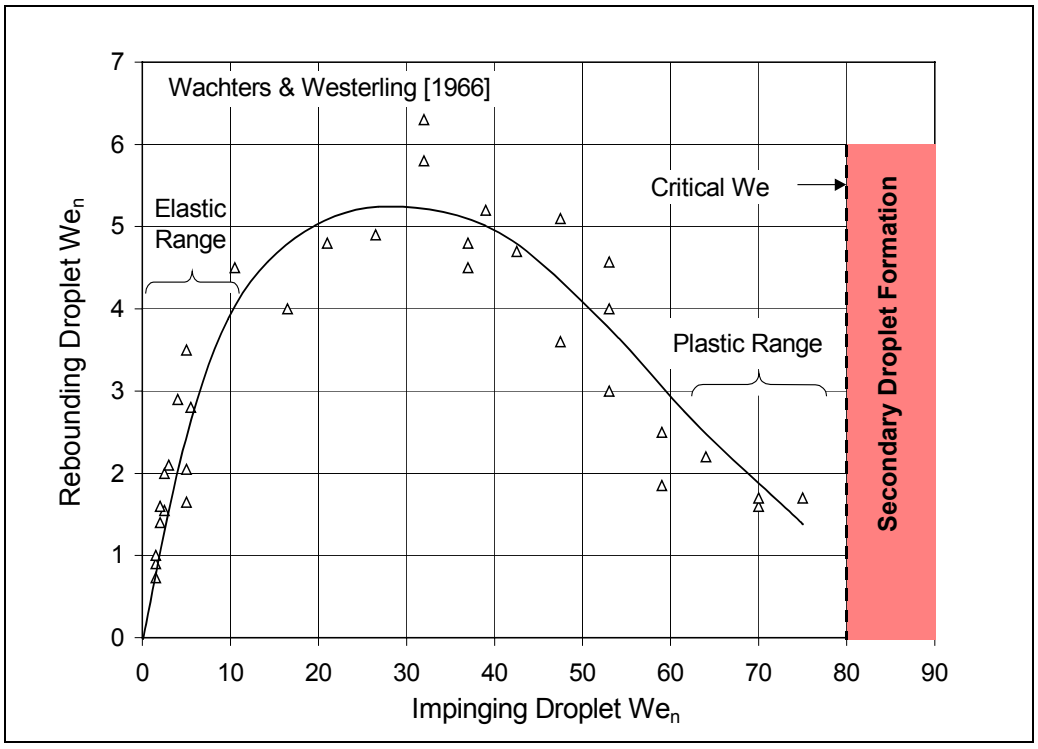

Figure 2.4 Relationship between impinging and rebounding normal Weber number [35]

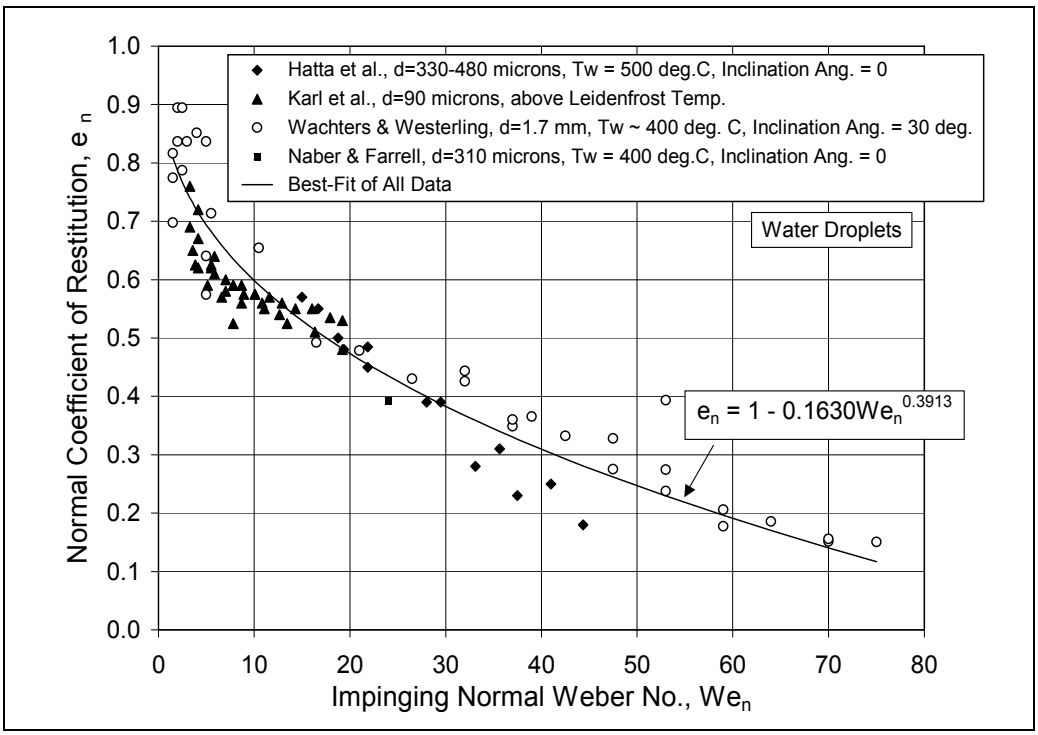

Figure 2.5 Droplet coefficient of restitution as function of the normal Weber number at above Leidenfrost temperature

2.4 Droplet Spread at the Wall

2.4.1 Theory

The droplet spread at the wall is calculated from the droplet deformation on impact. The droplet deformation is a process of energy transformation between kinetic and surface energies. The following analysis is based on the work done by Chandra and Avedisian [34]. Let the subscript 1 denote the stage before the droplet impacts the surface, and the subscript 2 denote the stage when the droplet reaches maximum spread on the surface. The droplet kinetic energy (E_{k1}) before impact can be expressed as follows:

$$\begin{aligned} E_{k_1} &= \left(\frac{1}{2}\rho_d v_1^2\right)\left(\frac{1}{6}\pi d^3\right) \\ &= \frac{1}{12}\pi\rho_d v_1^2 d^3 \end{aligned} \tag{2-4}$$

Where v_1 and d are the droplet velocity and diameter before impact. After impact, the kinetic energy reduces by the deforming droplet, and approaches zero as the droplet reaches a maximum spread diameter, d_{max}. The droplet surface energy at stage 1, E_{s1}, is:

$$E_{s_1} = \pi d^2 \sigma_d \tag{2-5}$$

The droplet surface energy at stage 2, E_{s2}, was given by Ford and Furmidge [43] as:

$$E_{s_2} = \left(\frac{1}{4}\pi d_{max}^2\right)\sigma_d(1-\cos\theta) \tag{2-6}$$

Where θ is the droplet contact angle at the surface. This is defined as the angle between the tangent line at the liquid-gas interface (at the point where the meniscus begins) and the horizontal surface. The energy consumed by the viscous dissipation of the droplet, E_{diss}, in going from stage 1 to stage 2 can be calculated from the following relationship:

$$E_{diss} = \int_0^{t_c} \int_{\forall} \phi \, d\forall \, dt \approx \phi \forall t_c \tag{2-7}$$

Where $d\forall$ is the incremental liquid volume and dt is the incremental time. t_c is the time it takes the droplet height, δ, to decrease from its maximum value of d to 0 assuming the droplet impinging velocity remains constant at v_1. This is based on mass conservation assuming the droplet spreads into a cylindrical disk. The dissipation function, ϕ, can be approximated from:

$$\begin{aligned} \phi &= \mu_d \left(\frac{\partial v_i}{\partial x_j} + \frac{\partial v_j}{\partial x_i} \right) \frac{\partial v_i}{\partial x_j} \\ &= \mu_d \left(\frac{\partial v}{\partial y} \right)^2 \\ &\approx \mu_d \left(\frac{v_1}{\delta} \right)^2 \end{aligned} \tag{2-8}$$

Chandra and Avedisian [34] approximated the volume of the viscous layer as:

$$\forall = \frac{1}{4} \pi d_{max}^2 \delta \tag{2-9}$$

The time t_c taken by the droplet to spread from stage 1 to stage 2 can be approximated by:

$$t_c = \frac{d}{v_1} \tag{2-10}$$

The dissipated energy can then be shown as:

$$E_{diss} = \frac{1}{4} \pi \mu_d \frac{v_1}{\delta} d d_{max}^2 \tag{2-11}$$

Applying the conservation of energy between stages 1 and 2, we get:

$$E_{k_1} + E_{s_1} = E_{s_2} + E_{diss} \tag{2-12}$$

Let us define the droplet maximum spread, β_{max}, as follows:

$$\beta_{max} = \frac{d_{max}}{d} \tag{2-13}$$

The following relationship can then be obtained:

$$\frac{3}{2}\frac{We}{Re}\beta_{max}^4 + (1-\cos\theta)\beta_{max}^2 - (\frac{1}{3}We + 4) = 0 \tag{2-14}$$

As Re approaches infinity, the droplet maximum spread simplifies to:

$$\beta_{max} \approx \sqrt{\frac{(1/3We + 4)}{(1-\cos\theta)}} \tag{2-15}$$

According to Fiedler and Naber [44], the contact angle θ can be considered fixed at 180^o for temperatures above Leidenfrost. The contact angle reduces to around 40^o as the temperature drops closer to the critical heat flux temperature.

2.4.2 Comparison Between Theory and Experimental Data

The maximum spread of the droplet diameter on a hot surface was experimentally investigated by several researchers. Empirical correlations were proposed mainly as function of the droplet impinging Weber number. Akao et al. [45] studied droplet spreading using liquids such as water and ethanol on a copper surface heated to 400 ^{o}C. The droplets ranged in diameter from 2.1 to 2.9 mm. They proposed the following correlation:

$$\beta_{max} = 0.613We^{0.39} \tag{2-16}$$

Ueda et al. [46] used water droplets of 0.94 to 2.5 mm in diameter impinging on stainless steel and copper plates heated at 300 ^{o}C. Their empirical expression was:

$$\beta_{max} = 0.87\left(\frac{We}{6} + 2\right)^{0.5} \tag{2-17}$$

Hatta et al. [37] used much smaller droplets in their experiment ranging from 0.33 to 0.6 mm in diameter. Their test surface, which was made of Inconel alloy, was heated to 500 ^{o}C. Their experimental data yield the following expression:

$$\beta_{max} = 0.093 We^{0.74} + 1 \tag{2-18}$$

Figure 2.6 shows a comparison between the empirical correlations and the theoretical expression for the droplet maximum spread at the wall. The above expressions by the different researchers [37, 45, 46] were in good agreement with each other. The prediction of the droplet maximum spread by the theoretical expression was higher than any of the experimental data, but it is interesting to see that it was not too far off.

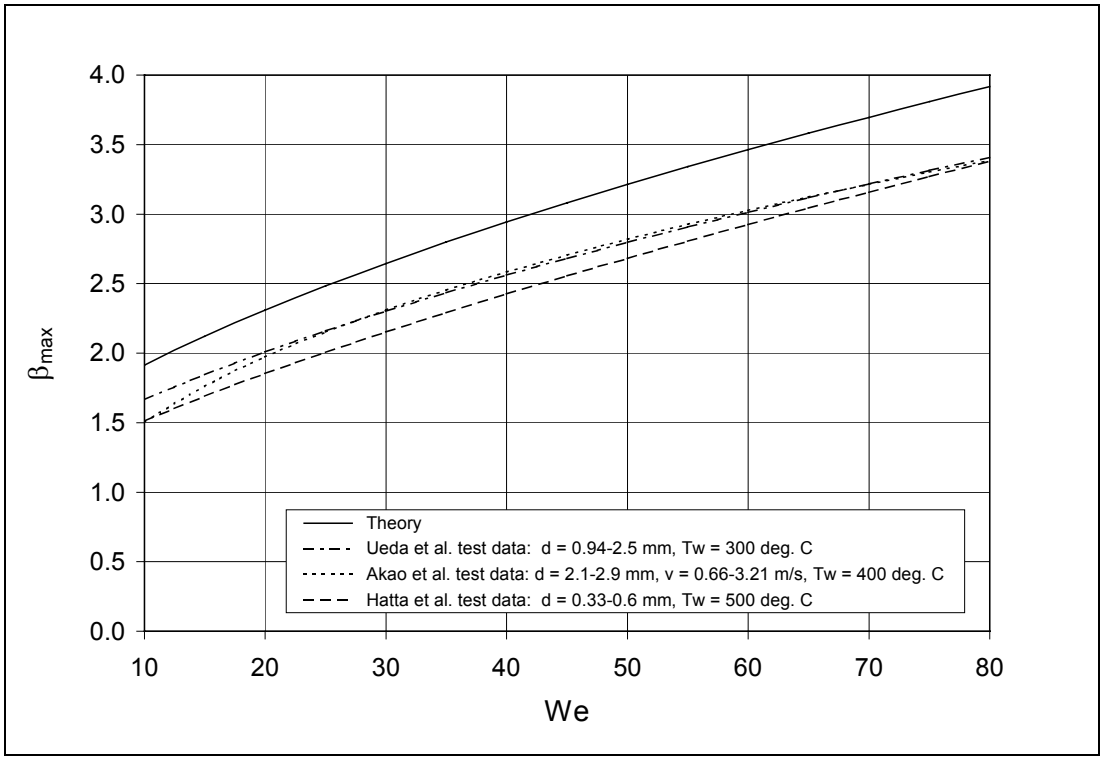

Figure 2.6 Droplet maximum spread
(A comparison between theory and experimental data)

2.5 Modeling of the Droplet Rebound at High Pressure

Experiments conducted for single droplet impingements on heated surfaces at atmospheric pressures show that during impaction, the droplet spreads in the form of a flattened disk along the surface, and then recoils as a result of the droplet surface tension before finally rebounding. An increase in the droplet maximum spread would result in an increase in the droplet momentum loss due to the increase in the energy dissipation at the surface. This energy dissipation is associated with both the spreading of the droplet and the recoiling process where the recoiling process is directly affected by the spreading. Therefore, any increase in the droplet spread would result in a decrease in the droplet coefficient of restitution.

The droplet maximum spread was theoretically shown to be a function of Weber number according to equation (2-15). As the ambient pressure increases, both the droplet density and surface tension decrease with the rate of decrease in the surface tension much larger than the rate of decrease in the droplet density. As a result, at high pressure, the droplet will deform and spread more. However, the increase in the droplet spread is not very significant. Figure 2.7 shows the variation in the droplet maximum spread with ambient pressure. For instance, the increase in the droplet spread with respect to the atmospheric condition case is only about 16% at an ambient pressure of 20 atm, and 34% at 50 atm. For a very low sub-atmospheric pressure of 0.006 atm, the droplet spread decreases by about 7%. Even though this will lead to a slight decrease in the droplet coefficient of restitution at high pressures, and a very slight increase in the coefficient of restitution at low pressures, this variation can be considered not to be very significant. Therefore, the correlation between the droplet coefficient of restitution and the droplet Weber number that was developed for atmospheric conditions can still be applicable with sufficient accuracy for higher ambient pressures, and for sub-atmospheric pressures.

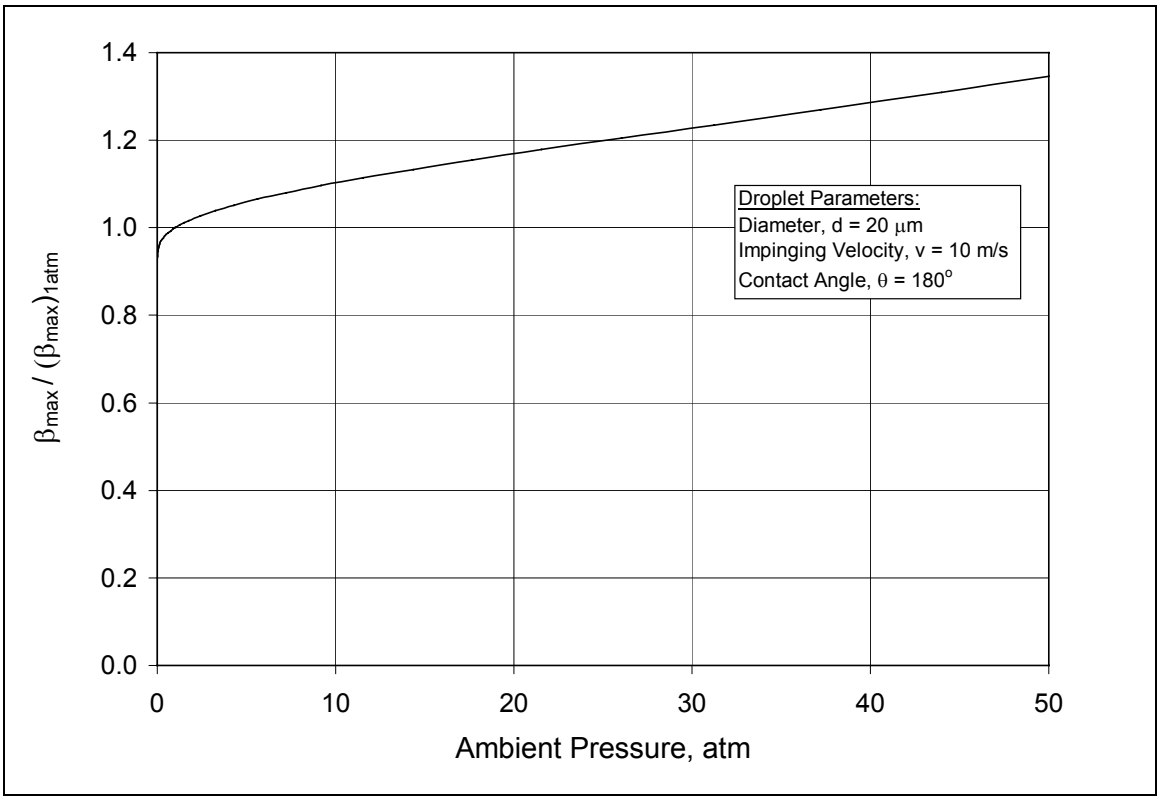

Figure 2.7 Droplet maximum spread versus ambient pressure

3.0 MODELING OF THE SPRAY HEAT TRANSFER

3.1 Droplet Heat Transfer at Atmospheric Conditions

There are three modes of heat transfer associated with spray cooling (Figures 3.1 and 3.2) [47]: 1) conduction due to the droplets contact with the surface, 2) convection associated with the bulk air flow and the droplet cooling of the thermal boundary layer, and 3) radiation exchange between the heated wall and the two phase air-water spray mixture. Contact heat transfer of the impinging droplets can be classified into two types:

- Heat transfer with wetting contact occurring at lower surface temperatures
- Heat transfer with non-wetting contact occurring at higher surface temperature

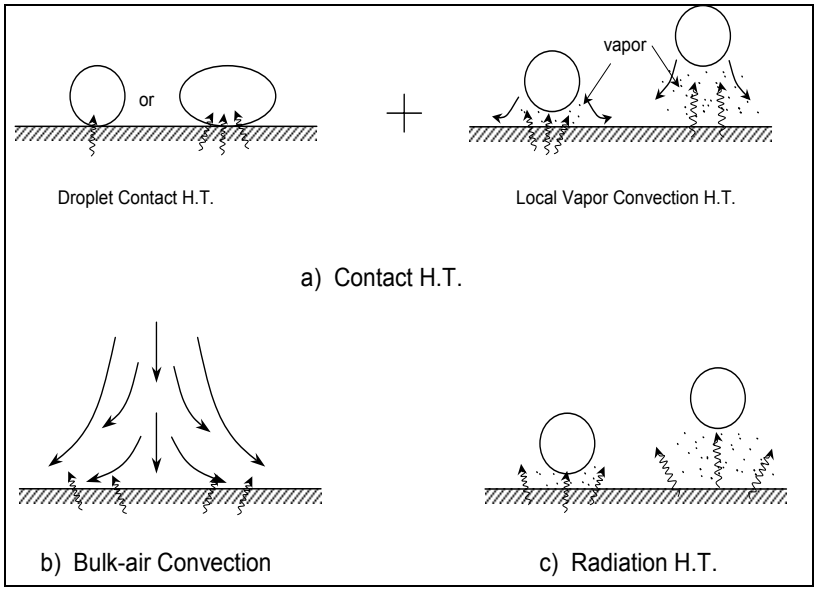

Figure 3.1 Basic mechanisms for spray heat transfer

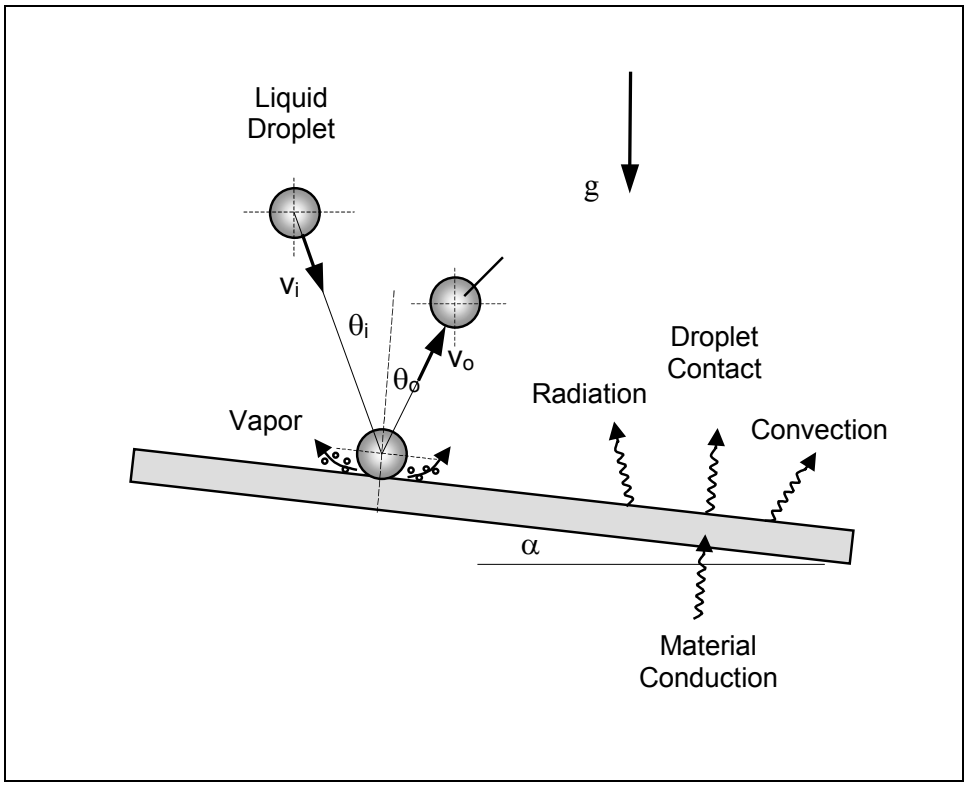

Figure 3.2 Spray cooling heat transfer modes

3.1.1 Wetting and Non-Wetting Droplet Heat Transfer

At wetting heat transfer, the droplets can be in continuous or semi-continuous direct contact with the wall. After an initial period of heat transfer by transient conduction, the droplets enter into either nucleate or transition boiling regimes. In this case, the droplet incoming Weber number may have a weak effect on enhancing the droplet breakup. Wet cooling results in a significant drop in the surface temperature due to its highly cooling efficiency.

In non-wet cooling, also referred to as film boiling, a significant amount of water vapor is generated between the hot surface and the droplet, thus preventing direct contact. Since vapor has a very low thermal conductivity, it acts as an insulation between the surface and the incoming spray; therefore, lowering the cooling efficiency. In this cooling regime, the incoming

droplet velocity (or Weber number) has a significant influence on the cooling efficiency. For low velocities, droplets cannot penetrate through the film layer. For high velocities, droplets can penetrate through the film layer, and more surface contact can be established. This enhances the cooling efficiency.

3.1.2 Parameters Affecting Droplet Contact Heat Transfer

The droplet diameter affects the Weber number, and has a strong influence on the cooling efficiency. A small diameter would cause an increase in the cooling effectiveness as compared to a larger diameter. This is due to the large surface coverage area achieved when using fine mist [48]. However, very fine mist may cause an adverse effect if the droplets are not large enough to hit the surface and as a result may be carried away by the air jet stream.

Beside the surface temperature and droplet Weber number (which is a function of diameter and velocity), there are other secondary factors influencing the heat transfer effectiveness but not as influential as the preceding ones. These include: droplet impingement frequency, surface inclination angle, droplet impinging angle, surface material and surface roughness.

The effect of the droplet impingement frequency and surface material is influenced by the surface temperature, while the droplet impingement angle and the surface roughness influence the impinging normal Weber number and the critical Weber number, respectively. For surface temperatures below Leidenfrost point, the heat transfer effectiveness decreases as the droplet impingement frequency increases due to the interference between the liquid film layer and the droplets. This effect weakens at temperatures above the Leidenfrost point because the vapor film layer prevents the droplets from making contact [15]. An increase in the droplet impingement angle (angle between the droplet motion direction and the normal to the surface) on a horizontal

surface lowers the normal component of the Weber number and the heat transfer effectiveness [49]. This also has a favorable effect on decreasing the interference between the impinging droplets. The same effect is seen if the surface is titled at an angle with respect to the impinging droplets. Highly conductive material, on another hand, increases the heat transfer rate for surface temperatures below the Leidenfrost point. However, above the Leidenfrost temperature, the high thermal conductivity acts in promoting vapor film generation which leads to isolating the droplets from the surface at a much faster rate [36]. Finally, surface roughness acts favorably in enhancing the heat transfer rate because the droplet breaks up into many parts at a Weber number much lower than the critical Weber number for a smooth surface [36].

3.1.3 Correlations for Droplet Contact Heat Transfer Effectiveness

Pederson (d = 200-400 μm, θ_i = 0 deg., v = 2-10 m/s, N = 10,816 drops/s) [13], Senda et al. (d = 350, 482 μm, θ_i = 0-60 deg., v = 3.2, 5 m/s, N = 50-848 drops/s) [15], and McGinnis and Holman (d = 2844-3835 μm, θ_i = 6-74 deg., v = 1.05-5.1 m/s) [16] have experimentally determined the heat transfer rate for a single stream of water droplets impinging on a heated metal plate by subtracting the heat transfer rate with impinging droplets from the heat transfer rate without the droplets. This net effect excluded the bulk air convective effect, but included the local convective effect due to the entrainment of the air around the droplet.

The heat transfer associated with the droplet contact with the heated surface can be empirically evaluated using an effectiveness parameter. This heat transfer effectiveness is defined as the ratio of the actual heat transfer induced by the droplet to the maximum possible heat transfer that can be achieved. The maximum release of heat from the droplet consists of three parts: 1) the pre-boiling cooling potential when the droplet arrives to the surface at a

temperature lower than the saturation temperature, 2) the release of heat when the droplet completely vaporizes at the saturation temperature, and 3) the superheating of the vapor to the surface temperature. The droplet heat transfer effectiveness can be expressed as [48]:

$$\varepsilon = \frac{q_c}{G\left[\Delta h_{fg} + c_{p,d}(T_{sat} - T_d) + c_{p,v}(T_w - T_{sat})\right]} \tag{3-1}$$

Where,

$$q_c = \left(mc\frac{dT}{dt}\right)_{\text{with droplets}} - \left(mc\frac{dT}{dt}\right)_{\text{no droplets}} \tag{3-2}$$

The droplet heat transfer effectiveness has been found to be strongly dependent on the droplet impinging speed as shown in Figures 3.3 and 3.4 for the wetting and non-wetting boiling regimes, respectively. A similar effect can also be seen if the data is plotted against the droplet impinging normal Weber number as shown in Figures 3.5 and 3.6. The contact heat transfer effectiveness increases significantly as the approach droplet velocity or the droplet impinging normal Weber number increases. The strong dependence on the surface temperature is also clearly visible. The heat transfer effectiveness is at its peak in the nucleate boiling region, but decreases significantly in the film-boiling region. A best fit through the data in Figures 3.5 and 3.6 result in the following expressions for the droplet contact heat transfer effectiveness:

For Non-Wetting Contact:

$$\varepsilon = 3.771\text{x}10^{-3}\,We_n^{0.691}e^{-9.079\text{x}10^{-4}We_n} \tag{3-3}$$

For Wetting Contact:

$$\varepsilon = 9.844\text{x}10^{-2}\,We_n^{0.3428} \tag{3-4}$$

Since the literature data were obtained at the critical maximum (Figure 3.5) and critical minimum (Figure 3.6) droplet contact heat fluxes, the heat transfer effectiveness between these points was interpolated and is presented in Figure 3.7 as function of both We_n and T_w. This figure shows the same trend behavior depicted by the boiling curve of water and is used to calculate for the droplet contact heat transfer effectiveness. Based on the above literature review, the following expression for the droplet contact heat transfer effectiveness is obtained as function of We_n for the temperature range between transition to film boiling:

$$\varepsilon = \left(0.10 + 5.2\text{x}10^{-4}\,We_n\right)\cos\frac{\pi}{470}\left[(T_w - T_d) - 130\right] + 8.6\text{x}10^{-4}\,We_n + 0.12 \qquad (3\text{-}5)$$

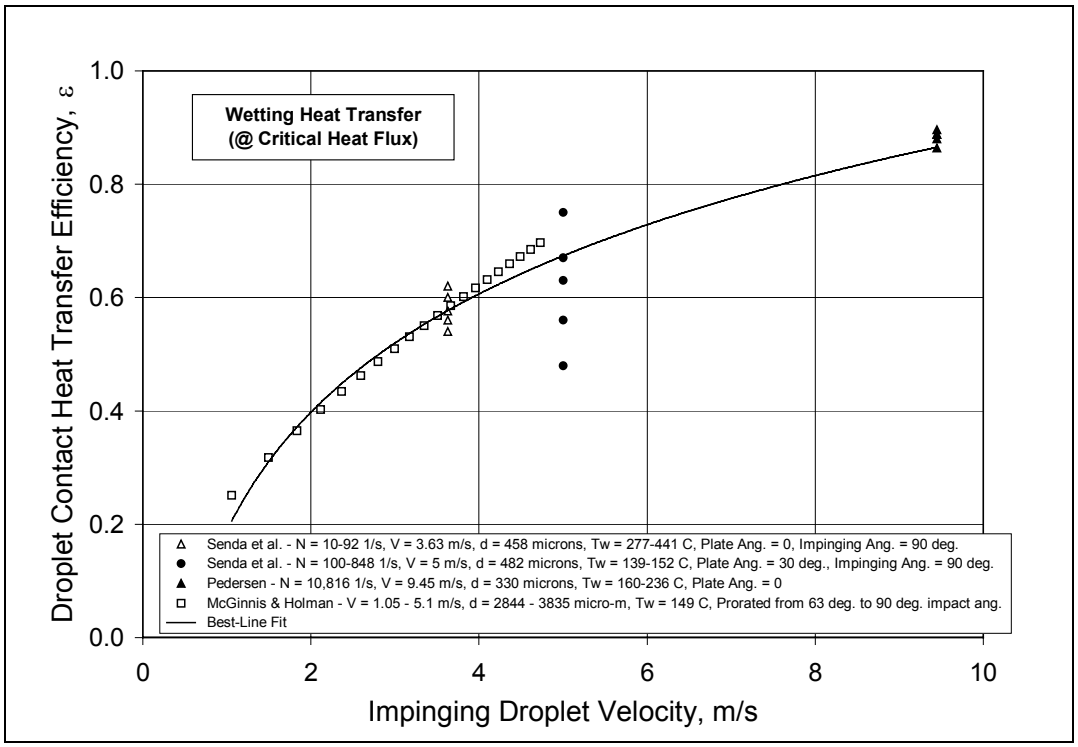

Figure 3.3 Droplet contact heat transfer effectiveness versus impinging speed for wet cooling

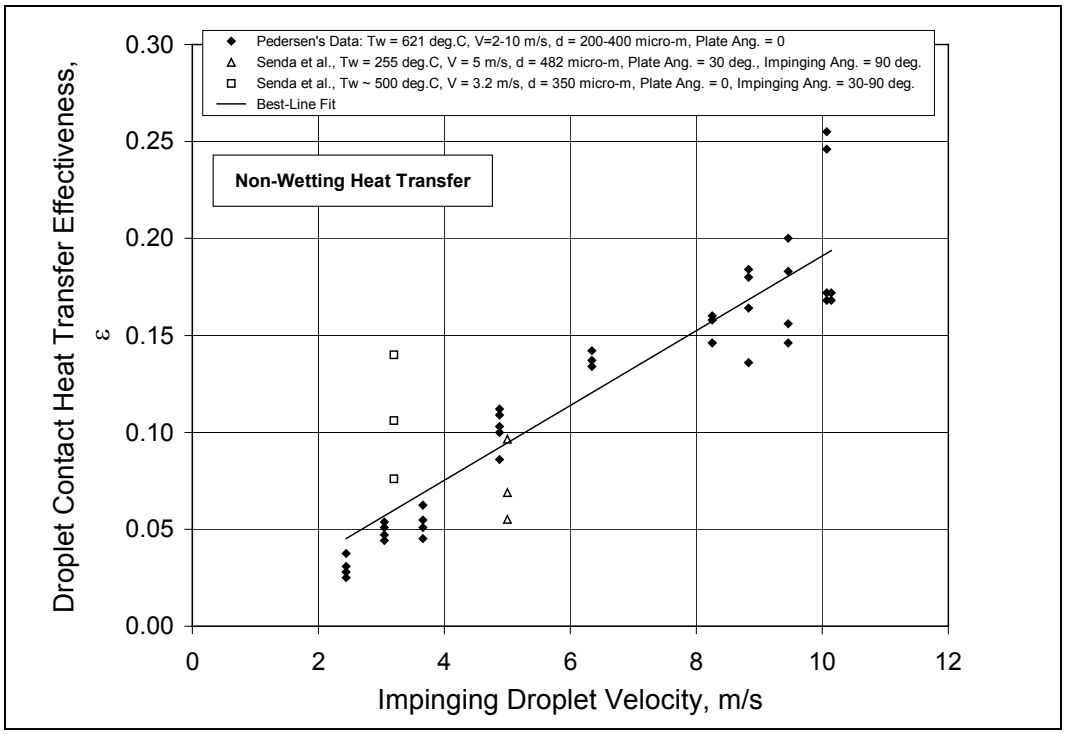

Figure 3.4 Droplet contact heat transfer effectiveness versus impinging speed for non-wet cooling

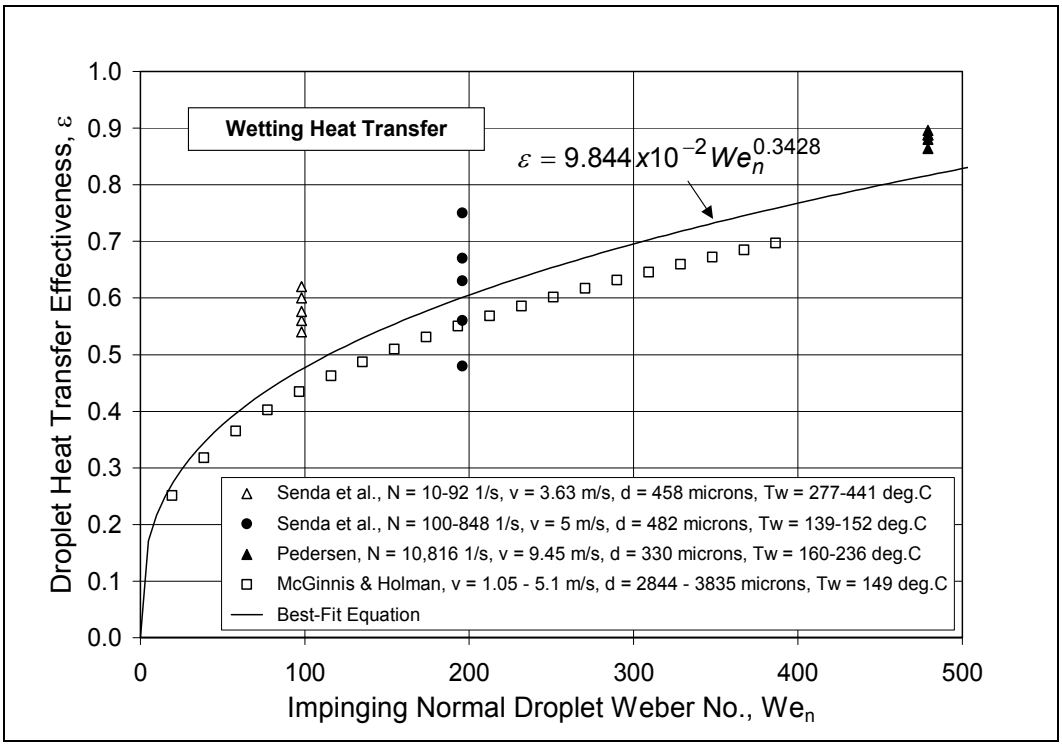

Figure 3.5 Droplet contact heat transfer effectiveness versus impinging Weber number for wet cooling

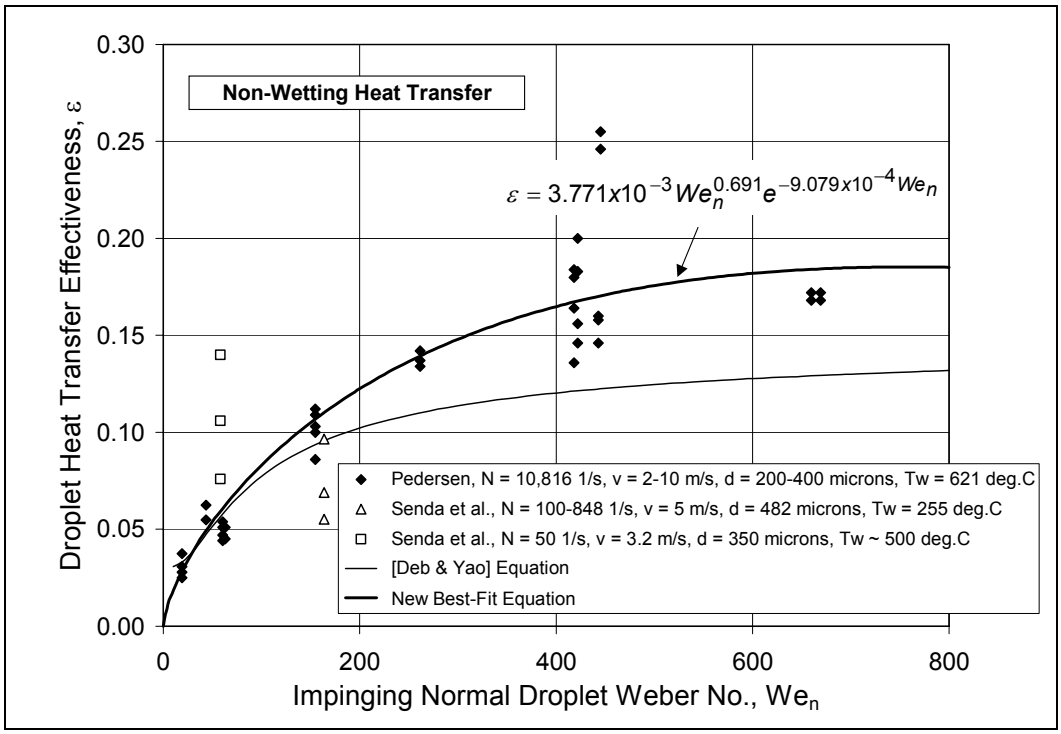

Figure 3.6 Droplet contact heat transfer effectiveness versus impinging Weber number for non-wet cooling

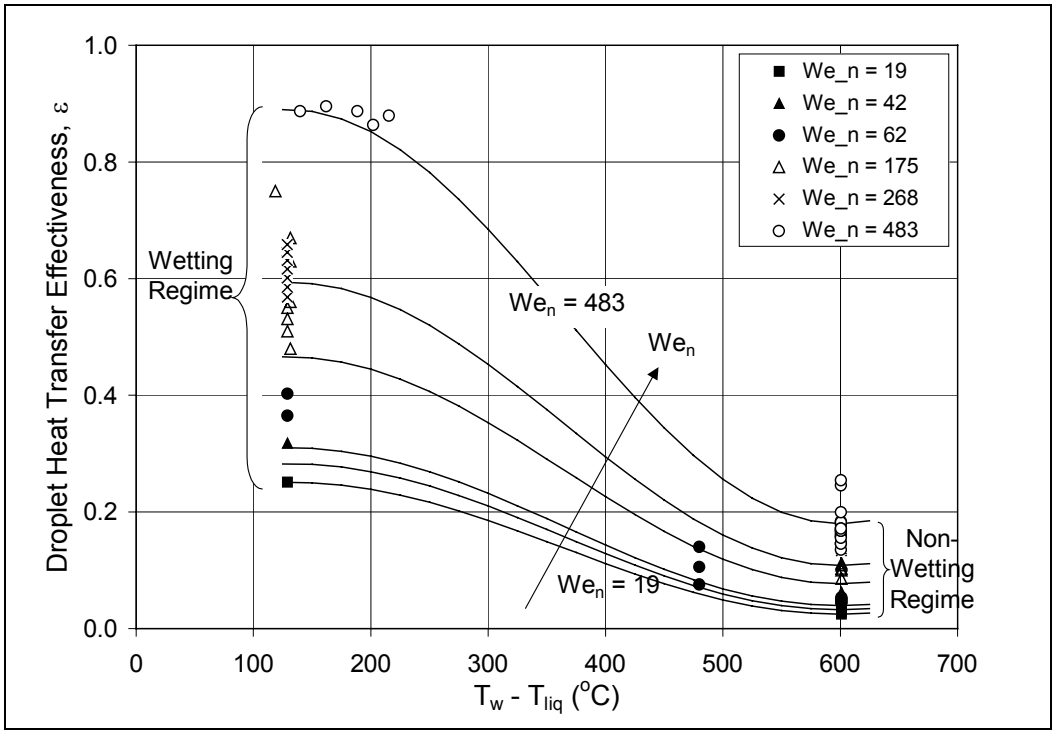

Figure 3.7 Droplet contact heat transfer effectiveness in the transition to film boiling region

3.2 Droplet Heat Transfer at High Ambient Pressures

3.2.1 Effect of Pressure on Droplet Sub-cooling

An important issue that arises at high-pressure conditions is the effect of the sub-cooling by the impinging water droplet. At atmospheric conditions, it is observed that the sub-cooling of the droplet has a negligible effect on the droplet contact heat transfer effectiveness. For water droplets evaporating at atmospheric conditions, the enthalpy of vaporization (h_{fg}) is the major factor of the heat absorption by the droplet. As the pressure increases, the effect of the pressure on the saturation temperature and the enthalpy of vaporization for water become significant. As shown in Figure 3.8, when the pressure increases, h_{fg} reduces significantly. Therefore, a large portion of the heat absorbed is now being used to increase the droplet temperature towards the saturation temperature. Because of the increase in the saturation temperature of water, the effect of the droplet sub-cooling becomes more evident at high pressures. The total heat removal by the droplet is calculated according to the following equation:

$$\begin{aligned}\Delta H &= (\text{Droplet Subcooling}) + (\text{Enthalpy of Vaporization}) + (\text{Vapor Superheating}) \\ &= c_{p,d}(T_{sat} - T_d) + \Delta h_{fg} + c_{p,v}(T_w - T_{sat})\end{aligned} \tag{3-6}$$

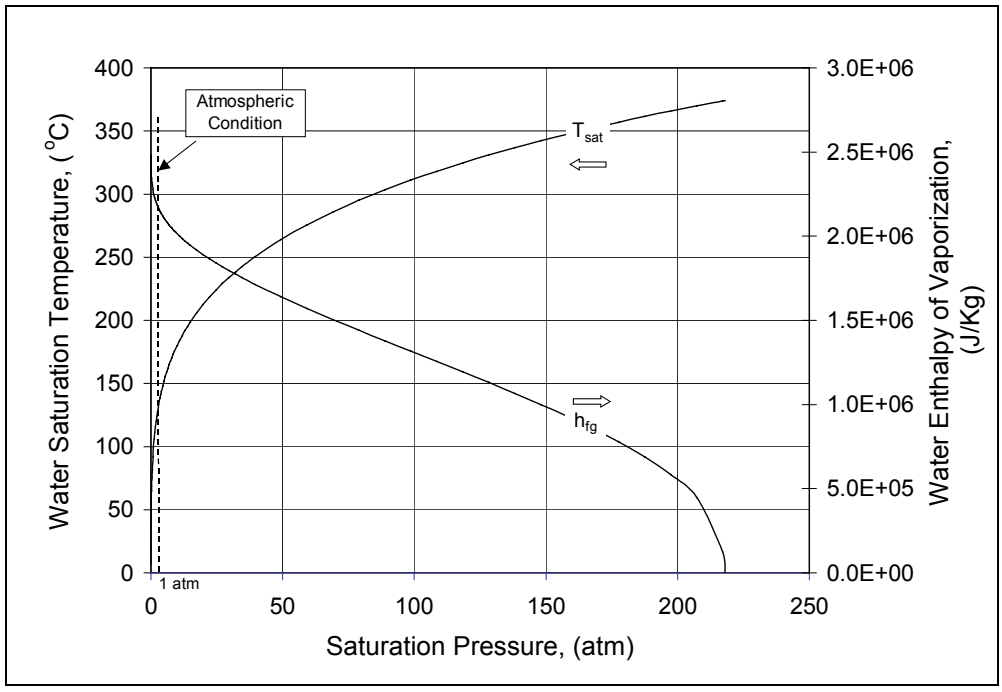

Figure 3.8 Effect of pressure on the water saturation temperature and enthalpy of vaporization

3.2.2 Effect of Pressure on the Leidenfrost Temperature

High-pressure conditions significantly alter the droplet cooling efficiency on heated surfaces. The effects of pressure on the evaporation time and on the Leidenfrost temperature of discrete water droplets deposited on metallic plates have been studied by Emmerson and Snoek [24, 25]. Figure 3.9 shows their results for water droplets on a stainless plate [25]. The chamber pressure ranged from 1 atm (14.7 psi) up to 5.1 atm (75 psi), and the water droplet size on the plate was estimated to be 3.8 mm. The Leidenfrost temperature was shown to increase significantly with the ambient pressure. In his experiments, Emmerson also showed the Leidenfrost temperature to vary with the pressure at different rates based on the surface material, such as the thermal diffusivity of the surface material, the surface emissivity, and the surface tension between the liquid droplet and the metal. Figure 3.9 also shows that the maximum evaporation time of the

droplet decreases as the Leidenfrost temperature increases. This result leads to higher droplet contact cooling effectiveness. The most distinguishing feature between the Leidenfrost temperature of water and that of other fluids is that the Leidenfrost temperature of water can exceed the critical temperature, while other fluids do not exceed that. At the critical point, the water temperature is 374 ^{o}C, and the water pressure is 22 MPa (3208 psi). As shown in Figure 3.10, for water droplets on a brass surface, the Leidenfrost temperature can exceed the critical temperature as the ambient pressure increases above 0.7 MPa but it tends back to the critical temperature at the critical pressure.

Testa and Nicotra [23] studied the influence of sub-atmospheric pressures on the Leidenfrost temperature for a single stream of water droplets impinging on a Molybdenum strip. The droplet size was about 2 mm, and the pressure in the vacuum chamber ranged from 1 atm down to 0.065 atm. Testa and Nicotra conducted their experiments for the case where the droplets fully rebounded from the surface, and also for the case where some residual wetting occurred. Figure 3.11 shows the variation in the Leidenfrost temperature (with respect to the conditions at 1 atm) as function of the ambient pressure for a wide range of pressures extending from sub-atmospheric to several multiples of atmospheres. The following empirical expression is a best-fit through the data:

$$T_{Leiden} - (T_{Leiden})_{1atm} = 7.024 + 123\log_{10}(P/P_{1atm}) + 36\log_{10}(P/P_{1atm})^2 \qquad (3\text{-}7)$$

Where T_{Leiden} is the Leidenfrost temperature, and P is the ambient pressure.

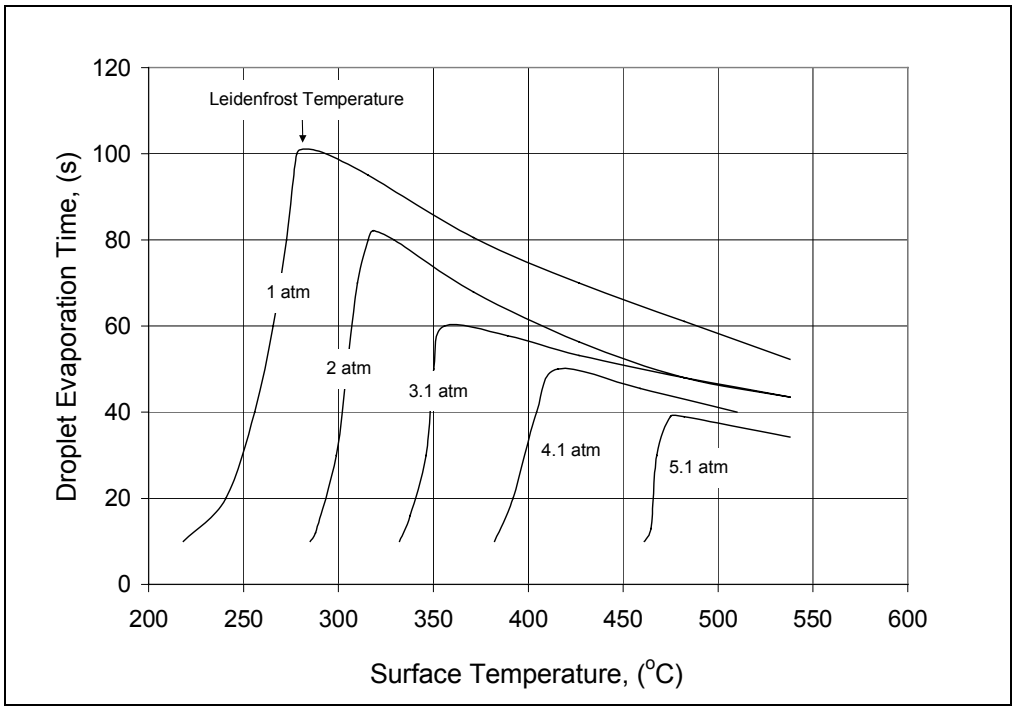

Figure 3.9 Effect of pressure on the evaporation time and Leidenfrost temperature (Water droplets on stainless steel plate [25])

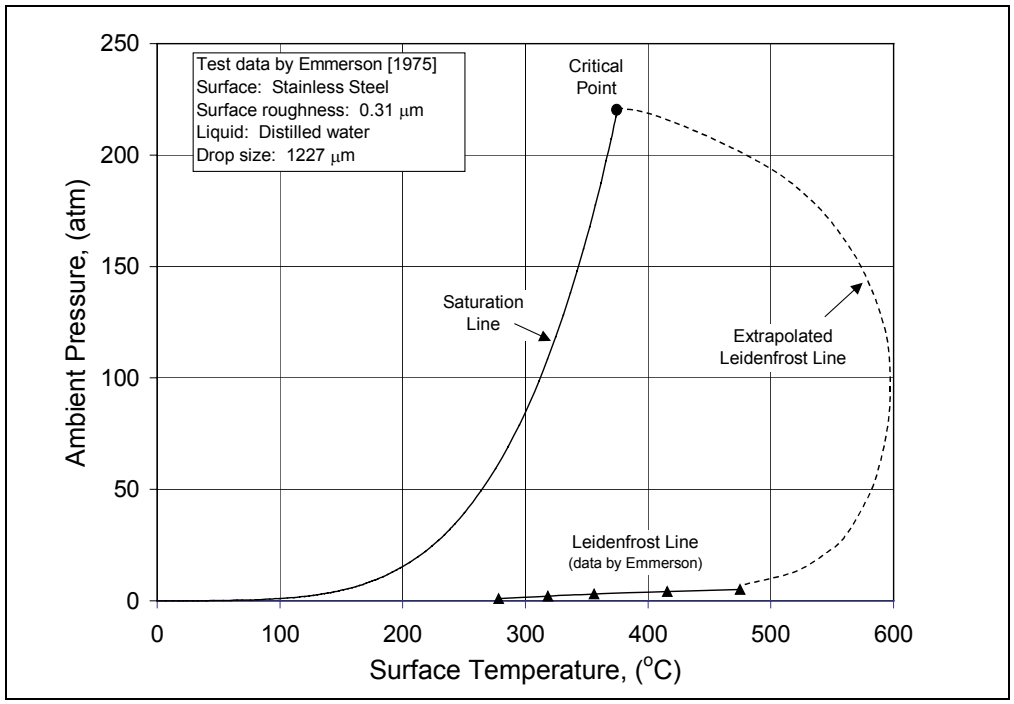

Figure 3.10 Predicted Leidenfrost line for water droplets on brass [24]

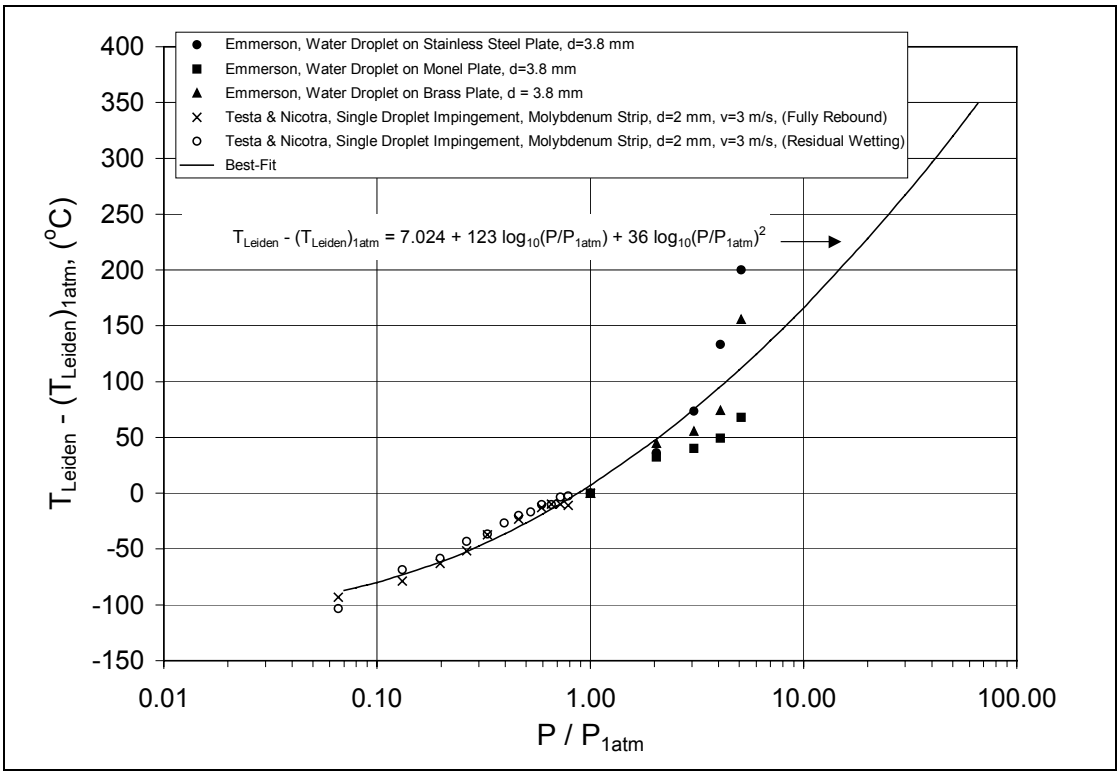

Figure 3.11 Variation in the Leidenfrost temperature with ambient pressure

3.2.3 Effect of Pressure on the Temperature at the Critical Heat Flux

Halvorson conducted experiments on the droplet impact cooling using a sealed chamber with ambient pressures of 0.1, 0.2, 0.5, 1.0, and 2.0 atm [22]. The air and water temperatures were close to 20 ^{o}C. Halvorson used three different sizes of gauge needles that produced droplet diameters ranging from 2.3 mm to 3.9 mm. The droplet frequencies ranged from 2 to 15 droplets per second, and the droplet impact velocity was about 1.3 m/s. In all the experiments, the droplet mass flux ranged from 0.15 kg/m^2.s to 1.6 kg/m^2.s. The heated surface was a nickel-plated end of a copper cylinder placed vertically. The surface was heated to temperatures where critical heat fluxes from the droplets impaction were obtained. The temperature at which the critical heat flux occurred ranged between 75 ^{o}C and 150 ^{o}C, with the lowest temperatures occurring at

the lowest pressures. Compared with the experiments conducted at 1 atm, the experiments at 2 atm show a 20 ^{o}C increase in water subcooling due to the change in water saturation temperature, while the experiments conducted at 0.1 atm show about 55 ^{o}C decrease in water subcooling. Figure 3.12 shows the variation in the critical heat flux temperature (with respect to the conditions at 1 atm) as function of the ambient pressure for a wide range of pressures. The following correlation for the critical heat flux temperature, T_{CHF}, is obtained:

$$T_{CHF} - (T_{CHF})_{1atm} = -2.031 + 68.44\log_{10}(P/P_{1atm}) + 30.27\log_{10}(P/P_{1atm})^2 + 15.5\log_{10}(P/P_{1atm})^3 \quad (3\text{-}8)$$

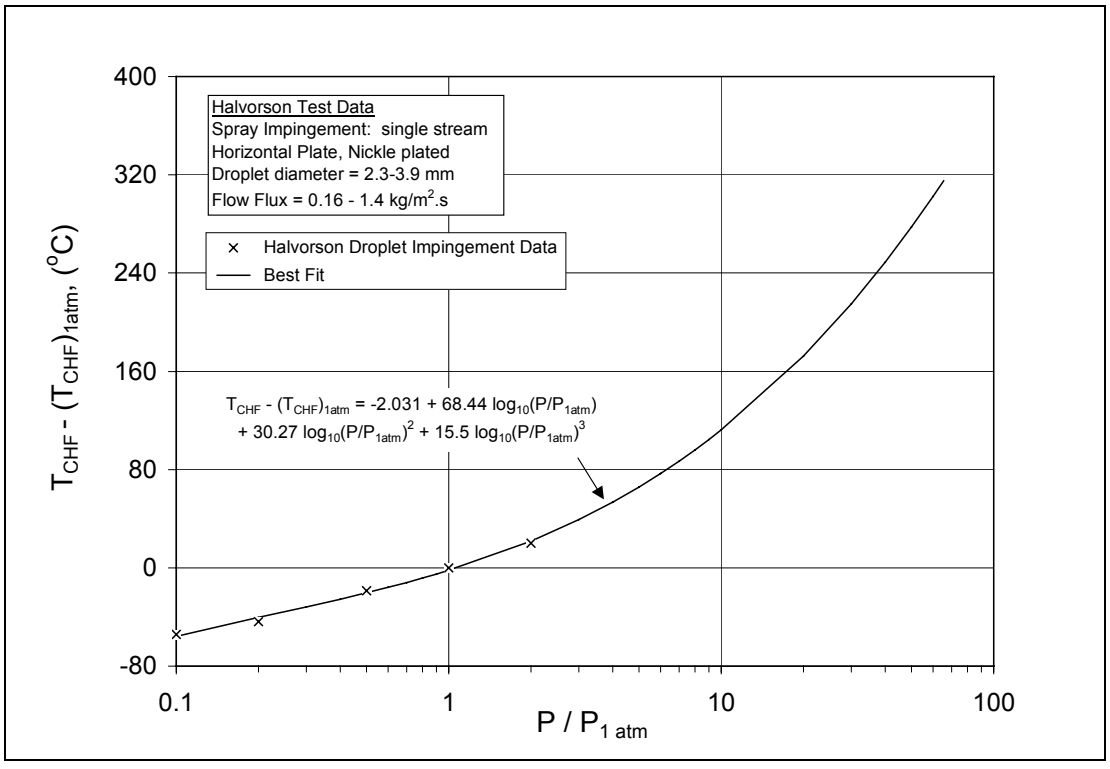

Figure 3.12 Variation in the temperature at the critical heat flux with ambient pressure

3.2.4 Effect of Pressure on the Minimum Heat Flux

Experiments conducted by Emmerson [24, 25] for water droplets deposited on flat surfaces show that the droplet evaporation time decreases with the increase in ambient pressure (Figure 3.9). The data demonstrate that the minimum heat flux corresponds to the maximum lifetime of the droplet. Figure 3.13 corresponds to the data obtained from Figure 3.9. The heat flux was calculated as function of the droplet evaporation lifetime and the total heat removal by the droplet. Figure 3.14 shows the effect of the ambient pressure on the minimum heat flux. The heat flux and the pressure are normalized with respect to the ambient conditions. For sub-atmospheric pressures, the data in Figure 3.14 is based on the experiments conducted by Testa and Nicotra [23] for single droplet impingements, while for pressures above atmospheric, the data is based on the experiments by Emmerson for water droplets deposited on metallic plates. A best-fit through the data results in the following correlations between the minimum heat flux, q_{min}, and the ambient pressure:

For $P \geq P_{1atm}$,

$$\frac{q_{min}}{(q_{min})_{1atm}} = 1.0 + 1.762 \log_{10}(P / P_{1atm}) \tag{3-9}$$

For $P \leq P_{1atm}$,

$$\frac{q_{min}}{(q_{min})_{1atm}} = 0.504 e^{0.667(P/P_{1atm})} \tag{3-10}$$

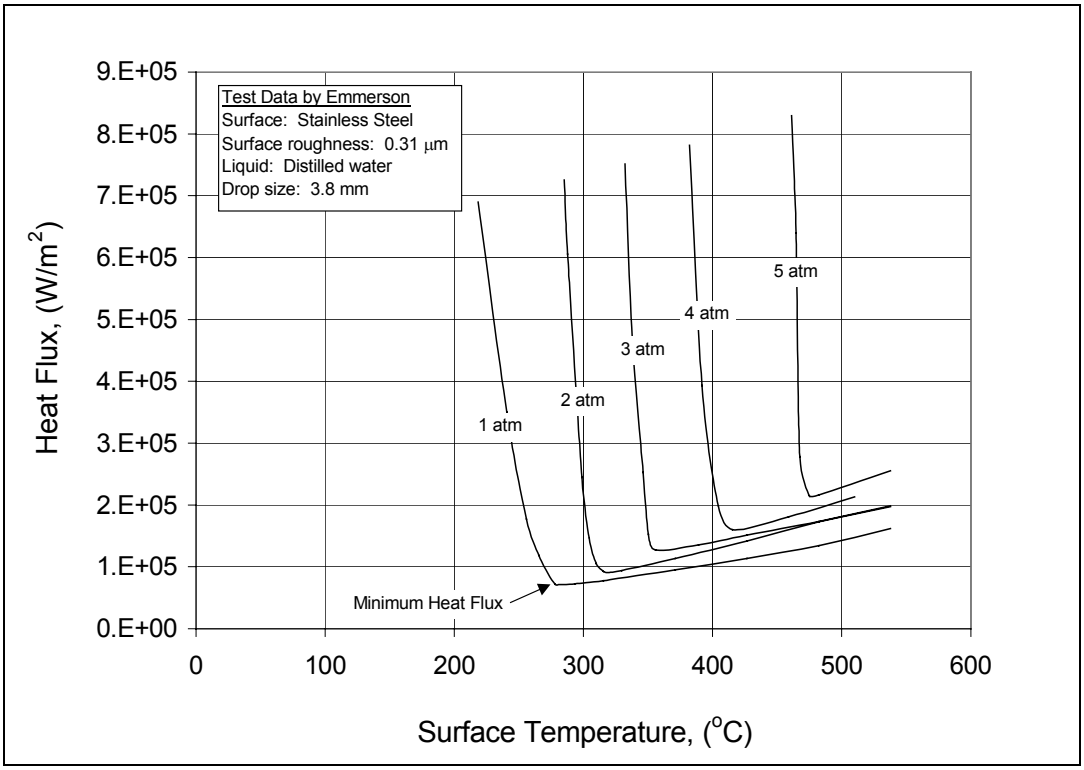

Figure 3.13 Effect of ambient pressure on the heat flux in the transition to film boiling range

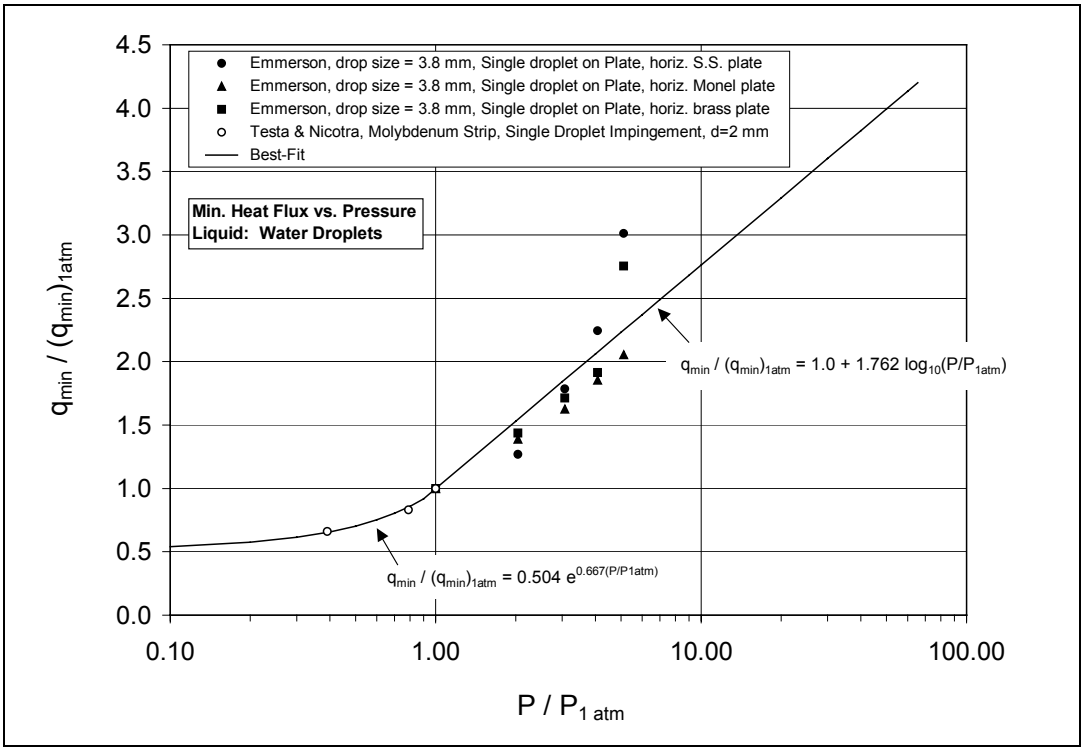

Figure 3.14 Minimum heat flux as function of ambient pressure

3.2.5 Effect of Pressure on the Critical Heat Flux

Halvorson's experimental data for a single stream of water droplets impinging on a heated plate with wetting contact show that the critical heat flux increases with ambient pressure. The high ambient experiments conducted at 2 atm were shown to produce about 15% increase in the critical heat flux compared to the experiments at atmospheric pressure, while the experiments conducted at the lowest ambient pressure of 0.1 atm were shown to produce a decrease of about 50% in the critical heat flux. It is worth mentioning also that the decrease in the critical heat flux is coupled with the decrease in saturation temperature. Figure 3.15 shows the critical heat flux as function of the ambient pressure. Again, the heat flux and the pressure are normalized with respect to atmospheric conditions. The following empirical correlation for the critical heat flux, q_{CHF}, is a best-fit through the data:

$$\frac{q_{CHF}}{(q_{CHF})_{latm}} = 0.985 + 0.412\log_{10}(P/P_{latm}) - 0.0797\log_{10}(P/P_{latm})^2 \qquad (3\text{-}11)$$

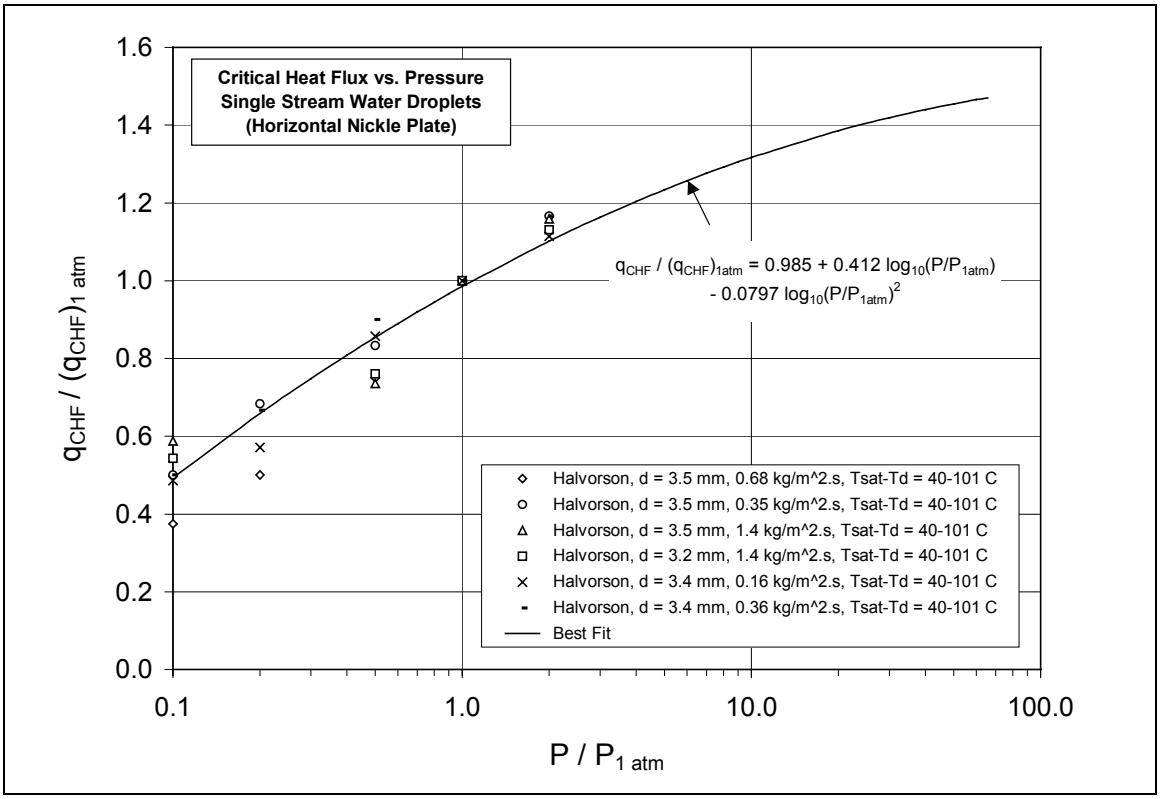

Figure 3.15 Critical heat flux as function of ambient pressure

3.2.6 Comparison with Pool Boiling

Cichelli and Bonilla [50], and Bonilla and Perry [51] obtained data on the maximum pool boiling heat flux from a horizontal chromium plated surface at pressures ranging from atmospheric to near critical (Figure 3.16). They conducted the experiments using a variety of liquids such as: water, ethanol, benzene, acetone, butanol, propane, n-pentane, and n-heptane. It was found that in the majority of those experiments, the maximum in the peak heat flux occurred somewhere between one-forth and one-third of the liquid critical pressure. For water, this is between 54 and 73 atm. The maximum heat transfer rate in pool boiling tends to zero as the pressure approaches zero. This is attributed to the very low vapor density that causes the amount of heat removal to significantly diminish at zero pressures. On the other hand, as the pressure

approaches the critical point, nucleate boiling ceases to be stable. The surface becomes bounded by vapor that acts as insulation between the liquid and the surface. At the critical pressure, the vapor density approaches the liquid density; thus, making the buoyancy force, which is proportional to the difference between the two densities and the driving force for nucleate boiling, to completely vanish.

Comparison between the pool boiling (Figure 3.16) and the single droplet critical heat flux (Figure 3.15) shows both curves increase sharply with pressure especially at the low pressures. Since test data for single droplets impaction on hot surfaces is not currently available at extreme high pressures, it is then fair to assume that the ambient pressure at which the peak in the critical heat flux occurs for pool boiling is also the same for single droplet heat transfer.

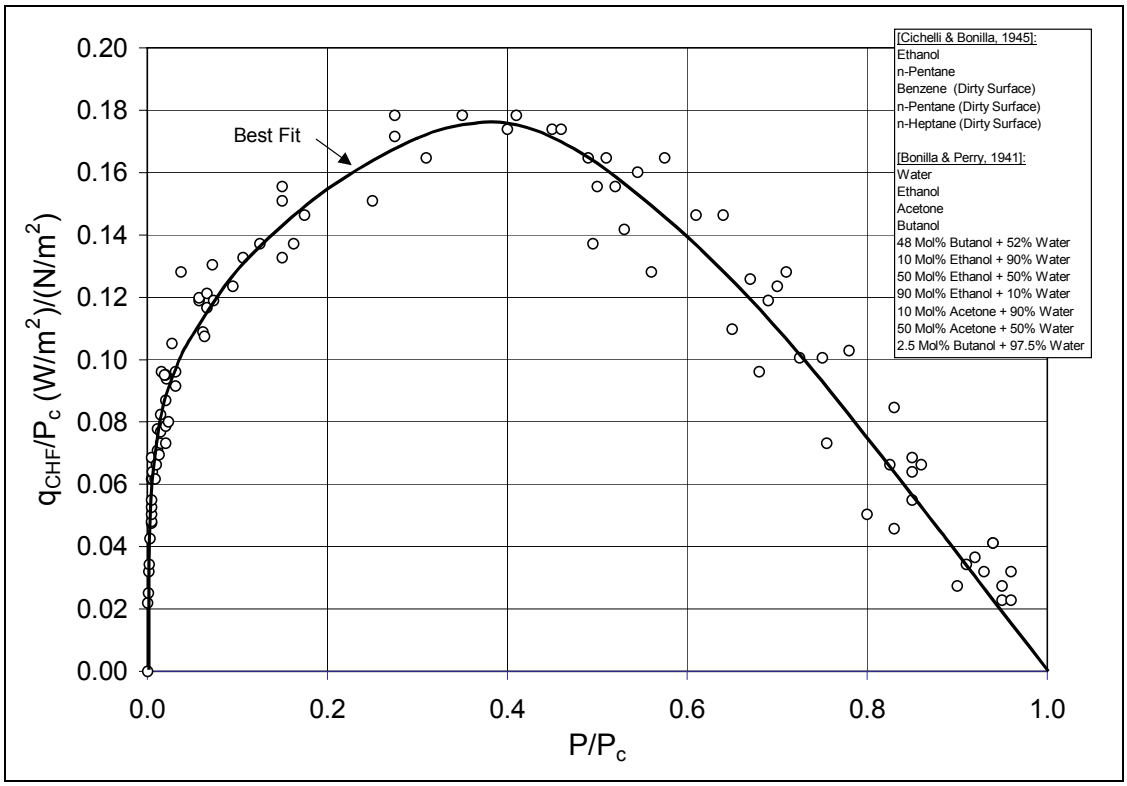

Figure 3.16 Pool boiling critical heat flux versus pressure [50]

3.2.7 Heat Transfer Effectiveness at Various Pressures

Several attempts were made by different researchers [52-58] to simulate the spray-wall interaction and heat transfer in high-pressure engine applications. The common disadvantage made by those researchers is that their studies were all conducted at relatively low surface temperatures (or room temperature). Another disadvantage is that even though these models were developed for engine-like conditions, they were based on experiments conducted at atmospheric conditions. Therefore, a model that can handle the high-pressure effects is needed and is of tremendous value to the research in high-pressure applications.

An understanding and predictability of the droplet-wall contact heat transfer effectiveness is needed for high pressure spraying environments. It was discussed earlier that the Leidenfrost temperature (Figure 3.11), and the temperature at the critical heat flux (Figure 3.12) increase with the ambient pressure. Furthermore, it was shown that the heat flux corresponding to the Leidenfrost point (Figure 3.14), and the critical heat flux (Figure 3.15) also increases with pressure. Using the results from those figures, the predictability of the droplet contact heat transfer effectiveness can be extended from the atmospheric pressure conditions to higher pressures, and also to sub-atmospheric pressures. At high pressures, the boiling curve associated with the droplet heat transfer would be modified as follows. Film boiling regime would be shifted further to a high temperature range as the pressure increases. As a result, a heat transfer mode that would be in the film boiling at atmospheric pressure would now occur closer to the nucleate boiling region for high ambient pressures. The high pressure would then significantly increase the droplet heat transfer effectiveness. At sub-atmospheric pressures, film boiling region would be shifted further to a lower temperature region as the pressure decreases. As a result, a heat transfer mode that would be in the nucleate boiling region would now occur in the

transition to film boiling region. The droplet heat transfer effectiveness would then significantly decrease. A new set of droplet contact boiling curves similar to that shown in Figure 3.7 (for atmospheric pressure condition) can be obtained for various pressures. Figures 3.17, 3.18, and 3.19 shows three sets of droplet heat transfer effectiveness curves at 0.1 atm, 5 atm and 50 atm, respectively.

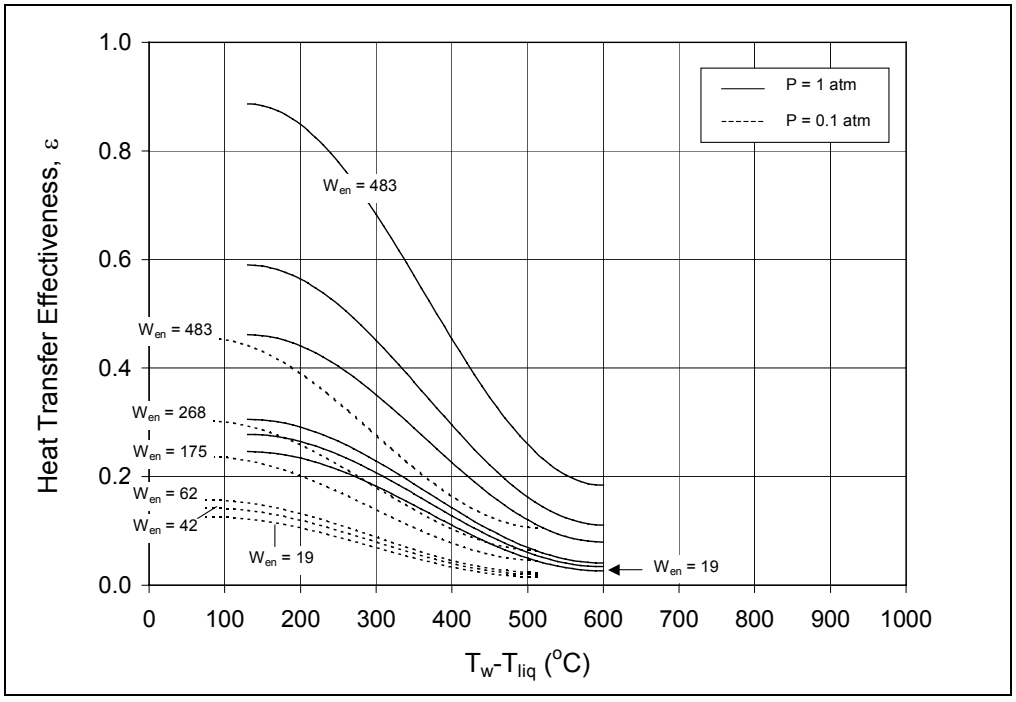

Figure 3.17 Comparison in droplet contact heat transfer effectiveness between 1 atm and 0.1 atm ambient pressures

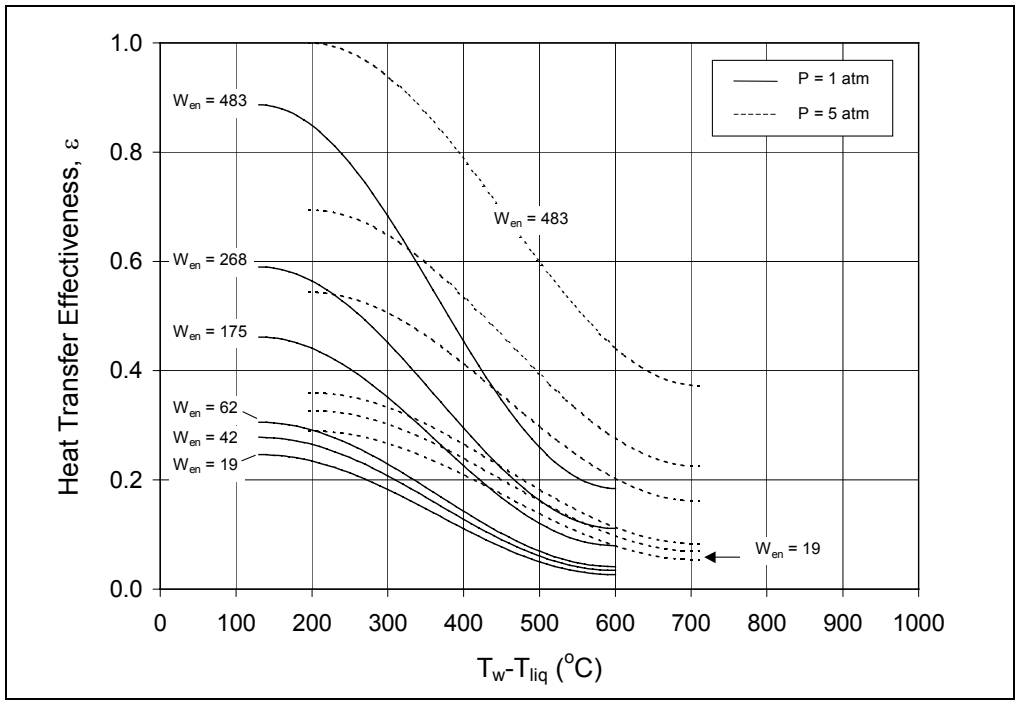

Figure 3.18 Comparison in droplet contact heat transfer effectiveness between 1 atm and 5 atm ambient pressures

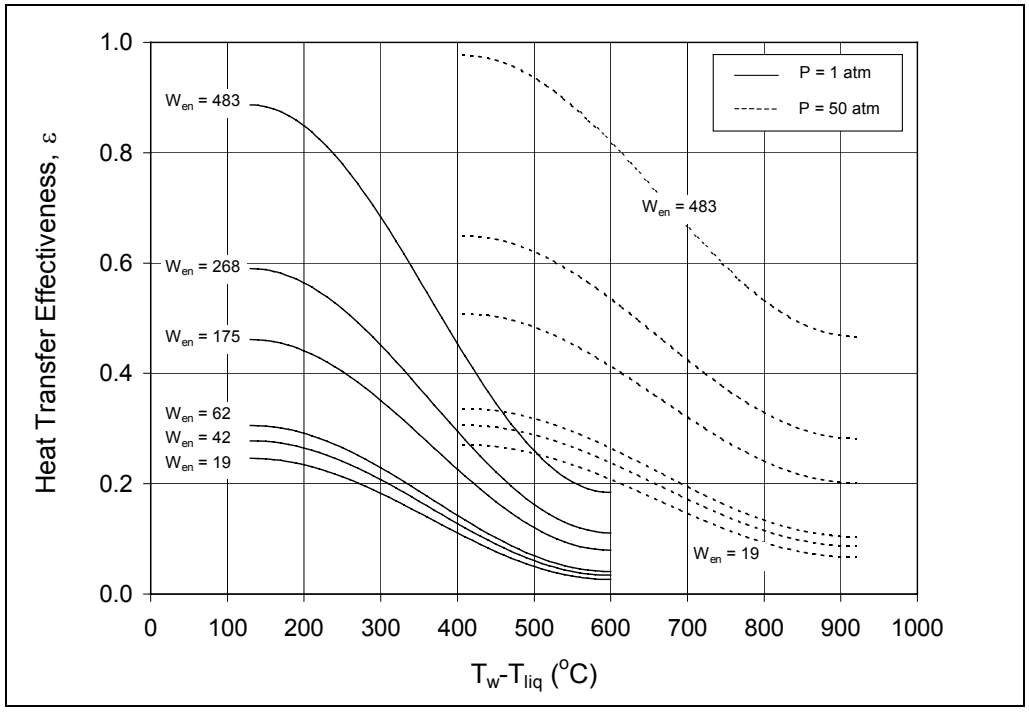

Figure 3.19 Comparison in droplet contact heat transfer effectiveness between 1 atm and 50 atm ambient pressures

4.0 NUMERICAL SCHEME

4.1 Description of the Computation Scheme

Numerical computations are performed using FLUENT software, which is a commercially available toolbox for CFD modeling. The modeling of the spray consists of a mixture of two phases: an air medium that is also referred to as the continuous phase, and the water droplets that is also referred to as the discrete phase. The conservation of mass, momentum, enthalpy, turbulent kinetic energy, and turbulent kinetic energy dissipation formulate the equations for the convective transport of the gas phase. The source terms in these equations represent the effect of the droplets phase. The droplets are dispersed in the continuous phase and are traced stochastically in the Lagrangian frame. The turbulence continuous phase model uses the two equations in the k-ε method which is expressed in Eulerian coordinates. The effect of the gas turbulence on the droplets is obtained by adding a velocity fluctuation to the mean gas velocity while tracing the droplets. The fluctuating velocity components, which are discrete piecewise functions of time, have their random value constant over an interval of time given by the characteristic lifetime of the eddies. A first-order upwind scheme is applied to the momentum, turbulent kinetic energy, and turbulent kinetic energy dissipation, while the SIMPLE (Semi-implicit Method for Pressure-Linked Equations) algorithm [59] is employed to enhance the velocity-pressure coupling. A control volume based approach is used to convert the governing equations into algebraic equations that can then be numerically solved.

In this model, steady state flow conditions are simulated. It is assumed that no droplet interaction occurs. Thus dilute spray conditions prevail. Also it is assumed that the incoming Weber number is small enough for the droplets not to splatter. The droplet dynamics and contact heat transfer is modeled using the empirical correlations presented earlier. An axi-symmetric model and a 3-D model are created in FLUENT to simulate the spray flow over a heated plate that has a diameter of 101.6 mm. The nozzle is situated at the center of the plate at a distance of 40 mm. A 75 x 60 quadrilateral mesh was generated as shown in Figure 4.1. Weighting factors were used to concentrate the grid mesh at the center of the computation domain, and also near the plate surface. Sufficient grid refinement at the wall was necessary to capture the wall interaction event and to ensure computational stability. During impaction, the droplet mass is recalculated based on the droplet contact heat transfer empirical correlations, and the excess mass that is the difference between the incoming droplet mass and the re-calculated mass is released as saturated vapor at the nearest cells to the wall.

The boundary conditions for the computation domain are as follows (Figure 4.2). Velocity inlet boundaries are applied for the water droplets and the air. The plane for these boundaries is considered to be at a small distance below the nozzle exit plane. The water droplets are released from this plane with a flow that is conical in shape. It is assumed that the water stream at this location has been fully atomized. This simplification is necessary to avoid the need for a complicated model of the nozzle where flow conditions are difficult to simulate. At the vertical edges of the computation domain, pressure outlet boundaries are applied. The wall boundary represented by the strip is assumed to be at a fixed temperature.

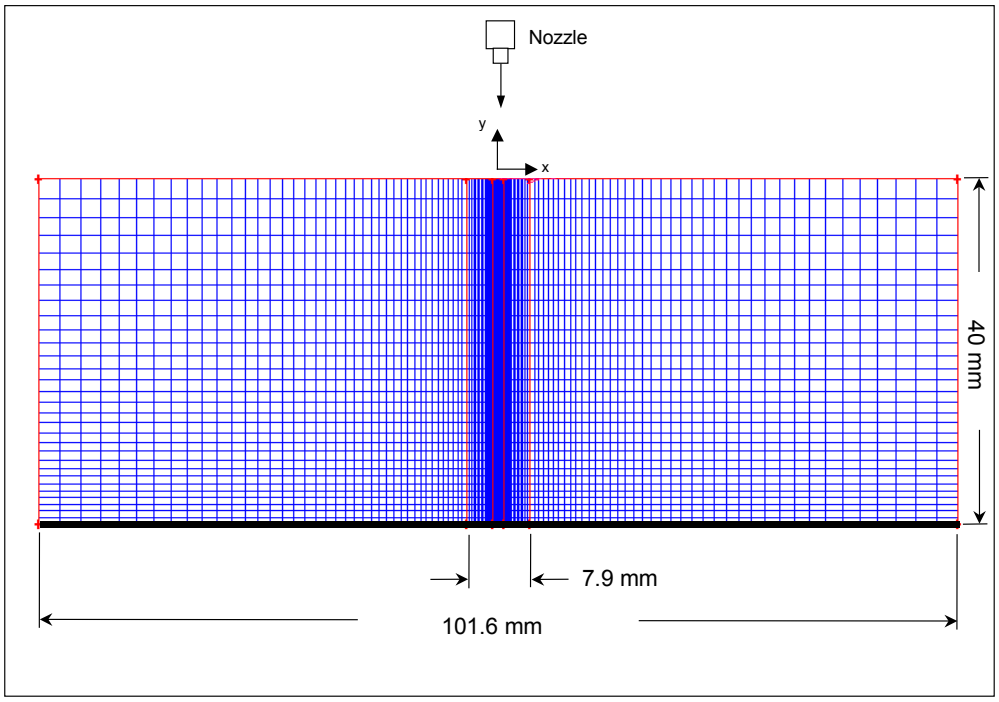

Figure 4.1 Grid mesh of the computation domain

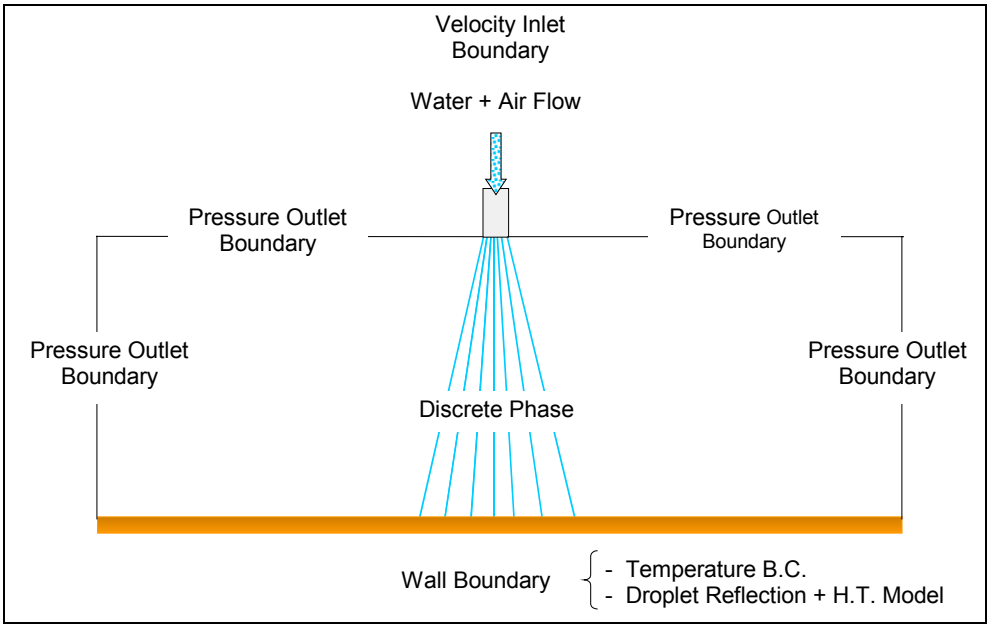

Figure 4.2 Model boundary conditions

4.2 Model Assumptions

The following is a summary list of the model's assumptions:

- An axi-symmetric and 3-D computational flow domain
- Steady state conditions
- Single stream of droplets, multiple streams of droplets, and conical full spray are used
- Uniform strip temperature
- Stationary strip
- Dilute to intermediate dense spray flow flux (0-8 $kg/m^2.s$)
- No droplet-to-droplet interaction at the wall
- 2-way coupling between the continuous phase (gas phase) and the discrete phase (droplets)
- Relatively low impinging Weber numbers such that no droplet disintegration occurs. The droplet outgoing velocity and direction is evaluated based on a coefficient of restitution parameter from experimental data.
- The droplet contact heat transfer effectiveness is calculated as function of the surface temperature and ambient pressure using the empirical correlations obtained from experimental data.
- No droplet deformation or spread at impact
- Negligible scale buildup on the strip at high temperatures
- Temperature dependant thermal and physical properties for the plate, air, and water
- Surface radiation is included in the model

4.3 Numerical Scheme Governing Equations

4.3.1 Gas Phase General Transport Equation

The general form of the gas phase equation for the energy, momentum, turbulence kinetic energy, and energy dissipation rate of the turbulent kinetic energy are represented as follows:

$$\frac{\partial}{\partial t}\left(\rho_a \Phi\right) + \nabla.\left(\rho_a \vec{U}\Phi\right) = \nabla.\left(\Gamma \nabla \Phi\right) + S_\Phi + S_{\Phi d} \tag{4-1}$$

Where Φ = 1, v_x, v_y, v_z, h, k and ε stands for the continuity, x-momentum, y-momentum, z-momentum, energy (static enthalpy), turbulent kinetic energy, and turbulent dissipation rate. In the context of this equation, h, k, and ε should not be confused with the heat transfer coefficient, conductivity and heat transfer effectiveness, respectively. ρ_a is the density of the continuous phase, and Γ is the effective diffusivity. $\vec{U}$ is the transport velocity vector. S_Φ is a general source term, and $S_{\Phi d}$ is a source term associated with the presence of the droplets.

4.3.2 The Compressible Form of the Gas Law

For a compressible flow, the ideal gas equation is written as:

$$\rho_a = \frac{P}{RT_a} \tag{4-2}$$

where P is the operating pressure. R is the gas constant, and T_a is the gas phase temperature as computed from the energy equation.

4.3.3 Droplet Force Balance Equation

The trajectory of the droplet is solved by integrating the force balance on the droplet, where the inertial force is balanced by the drag force, gravitational force and an external force [60]. This is expressed in the Lagrangian approach as follows:

$$\frac{d\vec{v}_d}{dt} = F_D(\vec{v}_a - \vec{v}_d) + \frac{\vec{g}(\rho_d - \rho_a)}{\rho_d} + \vec{F} \tag{4-3}$$

Where $\vec{v}_a$ is the velocity of the continuous phase, and $\vec{v}_d$ is the velocity of the droplet. Also, ρ_d and ρ_a are the densities of the droplet and the continuous phase, respectively. $\vec{g}$ is the gravitational acceleration, and $\vec{F}$ is an external force per unit droplet mass acting on the droplet. The drag force coefficient, F_D, is given by:

$$F_D = \frac{18\mu_d}{\rho_d d^2}\frac{C_D\,Re}{24} \tag{4-4}$$

Where the Reynolds number, Re, is defined as:

$$Re = \frac{\rho_a d|v_d - v_a|}{\mu_a} \tag{4-5}$$

and C_D is the drag coefficient applied on smooth spherical particles. It is given according to the expressions by Morsi and Alexander [61]:

$$C_D = \frac{24}{Re}, \quad Re < 0.1$$

$$C_D = \frac{22.73}{Re} + \frac{0.0903}{Re^2} + 3.69, \quad 0.1 < Re < 1$$

$$C_D = \frac{29.17}{Re} - \frac{3.89}{Re^2} + 1.22, \quad 1.0 < Re < 10 \tag{4-6}$$

$$C_D = \frac{46.5}{Re} - \frac{116.67}{Re^2} + 0.6167, \quad 10 < Re < 100$$

$$C_D = \frac{98.33}{Re} - \frac{2778}{Re^2} + 0.3644, \quad 100 < Re < 1000$$

$$C_D = \frac{148.62}{Re} - \frac{4.75x10^4}{Re^2} + 0.357, \quad 1000 < Re < 5000$$

4.3.4 Heat Transfer to the Droplet

The droplet temperature is calculated by applying an energy balance on the droplet. The sensible heat change in the droplet is balanced by the convective, radiative, and latent heat transfer between the droplet and the gas phase medium as follows [60]:

$$m_d c_{p,d} \frac{dT_d}{dt} = hA_d(T_a - T_d) + \frac{dm_d}{dt}\Delta h_{fg} + A_d \varepsilon_d \sigma(\theta_R^4 - T_d^4) \tag{4-7}$$

Where m_d is the droplet mass, $c_{p,d}$ is the droplet specific heat constant, T_d is the droplet temperature, T_a is the gas phase temperature, Δh_{fg} is the latent heat of vaporization, ε_d is the droplet emissivity, and σ is the Stefan-Boltzmann constant. θ_R is the radiation temperature given by:

$$\theta_R = \left(\frac{I}{4\sigma}\right)^{1/4} \tag{4-8}$$

Where I is the radiation intensity.

4.3.5 Coupling Between the Discrete and Gas Phase

The following terms appear as source terms in the gas phase transport equation due to the heat, mass, and momentum transfer between the droplets and the gas phase medium [60]. They are calculated as the droplets pass through each control volume in the computation domain:

Momentum Exchange:

$$F = \sum \left(\frac{18\mu_d C_D \, Re}{24\rho_d d^2} (v_d - v_a) \right) \dot{m}_d \Delta t \tag{4-9}$$

Heat Exchange:

$$Q = \left[\frac{\overline{m}_d}{m_{do}} c_{P,d} \Delta T_d + \frac{\Delta m_d}{m_{do}} \left(-\Delta h_{fg} + \int_{T_{ref}}^{T_d} c_{p,d} dT \right) \right] \dot{m}_{do} \tag{4-10}$$

Mass Exchange:

$$M = \frac{\Delta m_d}{m_{do}} \dot{m}_{do} \tag{4-11}$$

The coupling between the liquid droplet phase and the gas phase medium is accomplished as follows. The equations for the gas phase are solved prior to the injection of the droplets. The equations for the liquid droplet phase are then introduced, and the trajectories for the droplets are calculated. The effect of the discrete droplets onto the gas phase is then considered by resolving the gas phase equations with the newly calculated source terms associated with the presence of the droplets. The droplets trajectories are then recalculated based on the modified results of the gas phase equations. This procedure is repeated until a converged solution is reached where both the solution of the gas phase medium and the liquid droplets stops changing.

4.3.6 User-Defined Functions

The calculations for the droplet dynamic interaction with the wall, and the droplet-wall contact heat transfer effectiveness are introduced into FLUENT through user-defined functions. The User-defined functions are written in the C programming language. They are then complied using a “makefile” which invokes the system C compiler, and builds a native object code library. The object code library is linked to FLUENT executable software during runtime.

5.0 NUMERICAL SIMULATION FOR ATMOSPHERIC CONDITIONS

5.1 Spray Dynamics

To illustrate the droplet-wall interaction using the correlation derived for the coefficient of restitution as function of the impinging droplet normal Weber number, a simple case for single droplet impaction is presented as shown in Figure 5.1. A single droplet with a diameter of 150 μm is injected at a velocity of 5.5 m/s in still air, and the droplet trajectory is traced along the surface. Assuming the droplet does not break-up at those conditions, the impinging Weber number is high at the first impact, but reduces drastically after that until finally the droplet drifts away along the surface. Secondary impacts have low impacting energy which makes the droplet bounces almost elastically at the wall.

The air jet stream and the droplet size have a major influence on the droplet behavior at the wall. Figure 5.2 shows a stream of water droplets of diameters 10, 73, 137, and 200 μm injected into an air stream with a velocity of 7 m/s. The drag force is seen to have a strong influence on the droplet terminal velocity. Large droplets result in high terminal velocity and make it to the surface, while small droplets drift away. Moreover, the droplet size influences the frequency of impingements at the wall. Larger droplets retain enough momentum after impact to rebound and impinge again on the surface. The airflow stream also has an effect on the frequency of impingements, and the droplet rebound height. If the air velocity were to be very low, the

droplets would impinge on a much smaller area than they would if the air velocity is high. With higher air velocity, the droplets rebound height would be much lower because the air stream tends to push the droplets closer to the wall.

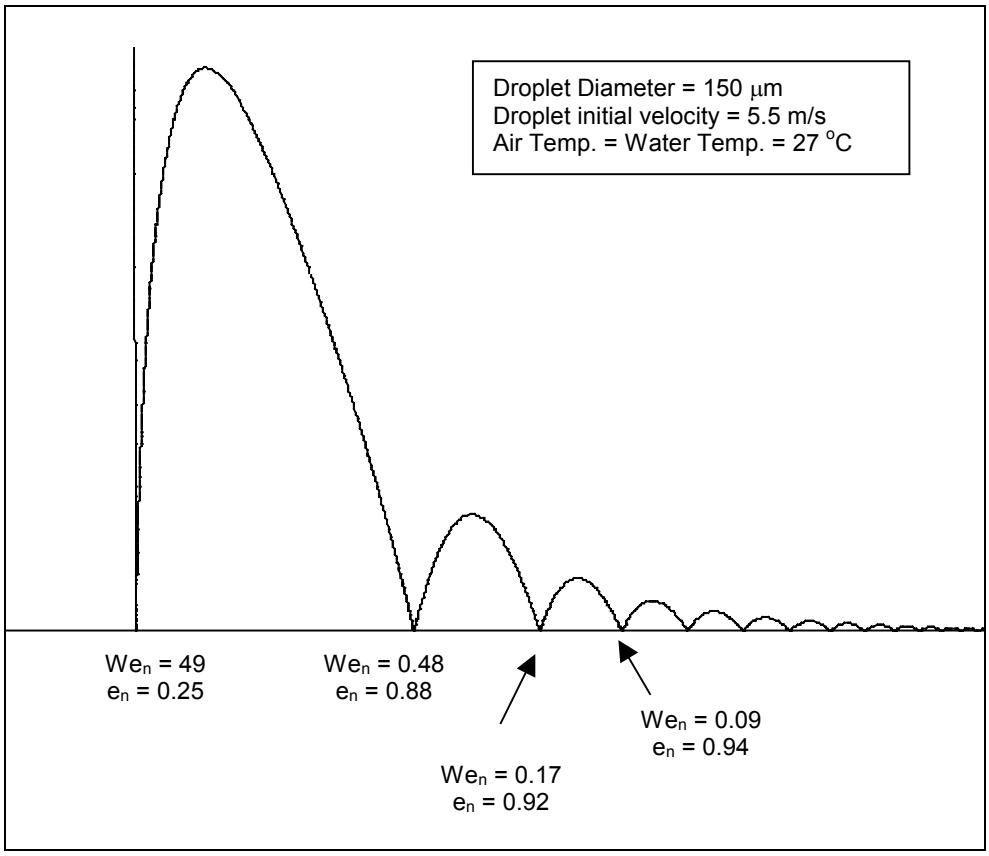

Figure 5.1 Effect of the multiple impingements on the droplet Weber number

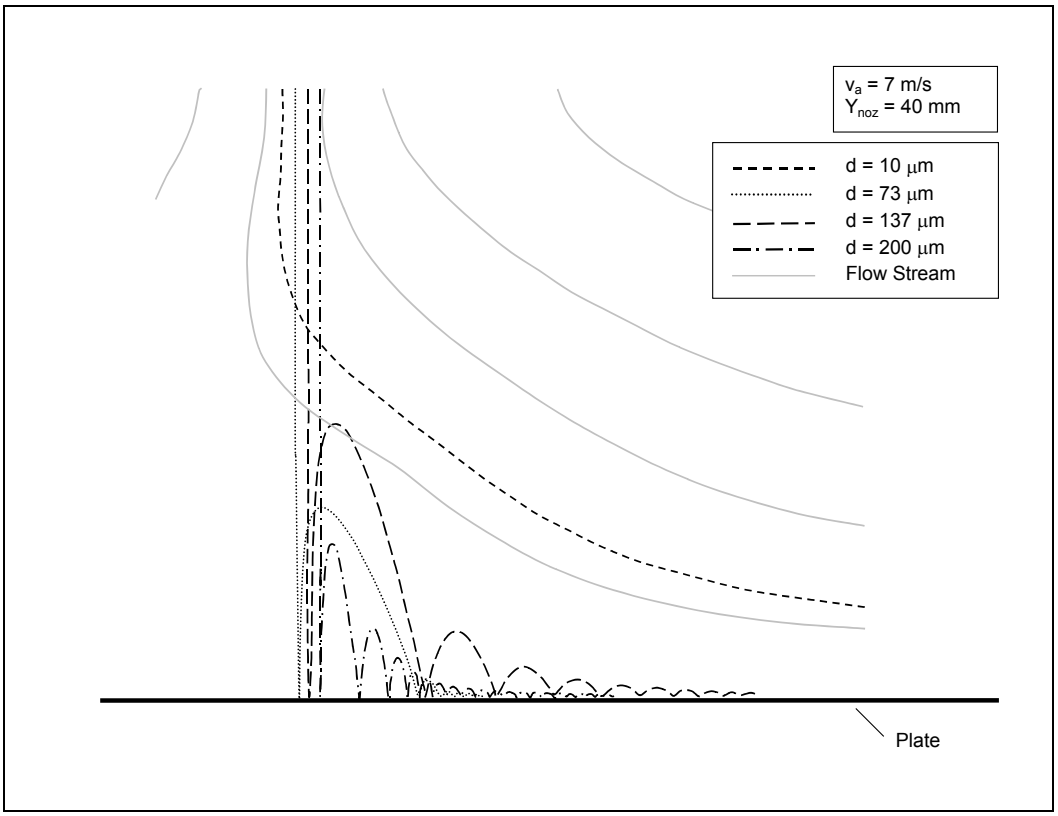

Figure 5.2 Surface interaction with various droplet diameters

Spray contact pressure is important in practical applications such as the descaling of the strip in the hot rolling mill. Figure 5.3 shows a full conical spray using a cone angle of 13^o, and uniform droplets size of 100 μm. The water to air mass flow rate ratio is one to one. Figure 5.4 shows the flow streamlines, and Figure 5.5 shows the bulk-air velocity profile in the vertical direction (y-direction). Figure 5.6 shows the bulk-air static contact pressure at the wall. Simulation results for several cases, presented in Figure 5.7, show the effect of the impinging spray angle on the contact pressure. The impinging spray angle is defined as the angle that the spray makes with the normal to the surface at the point of impact. The contact pressure is resolved into two components: bulk air, and droplets contact pressure. Results are shown for a dilute and for a dense spray. In the dilute case, the spray flow flux was 3.25 $kg/m^2.s$, and in the

dense spray case, the spray flow flux was 25 kg/m^2.s. The effect of the droplet contact pressure is larger than the bulk air contact pressure for dense sprays, while the opposite is true for dilute sprays. Theoretically, an impinging spray angle of θ_i should cause the contact pressure to decrease by a factor of $\cos^2\theta_i$ (shown by the theoretical line in Figure 5.7) because of the spray angle effect on the coverage area, and the normal component of the incoming velocity. It would be then reasonable to expect the droplets contact pressure to reduce by 50% if the impinging spray angle increases to 45^o from 0^o. However, simulation results show the contact pressure to be much lower for the dense case, while very close to 50% for the dilute case. A possible justification for this is the weak effect of droplets interference for dilute sprays.

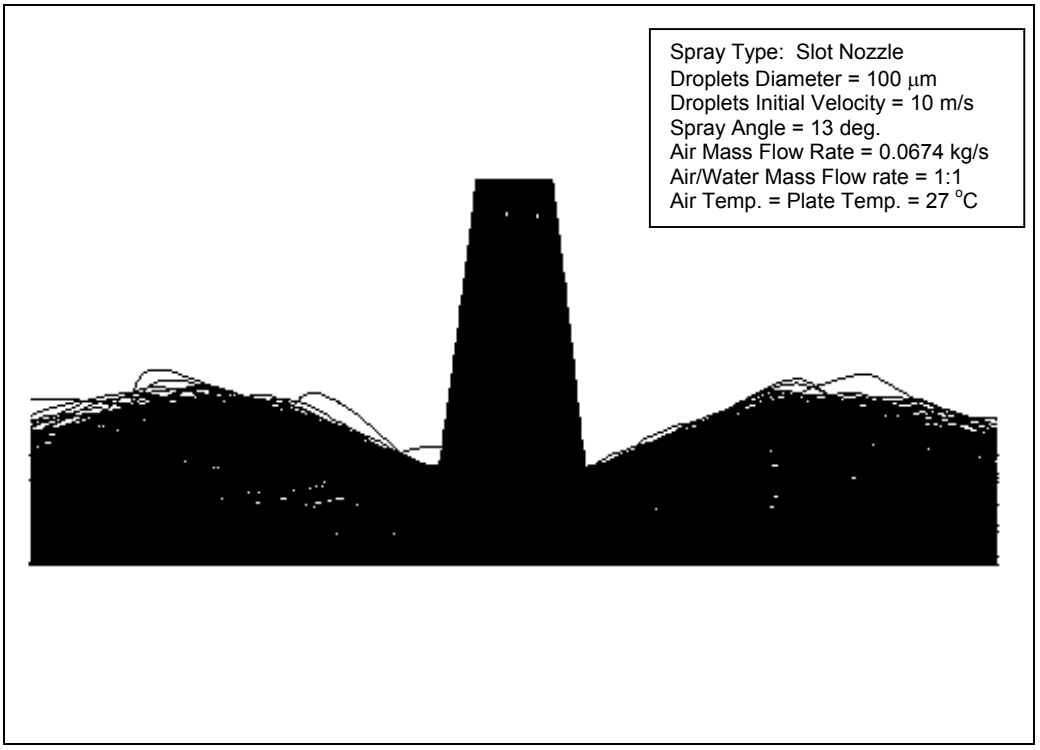

Figure 5.3 Full conical spray (13^o cone)

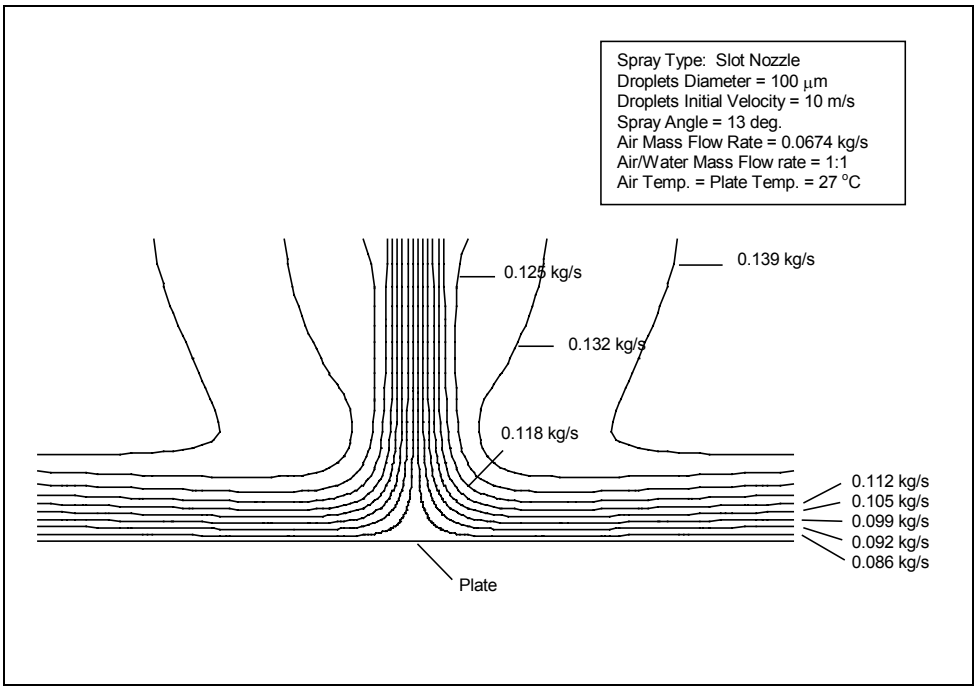

Figure 5.4 Flow streamlines

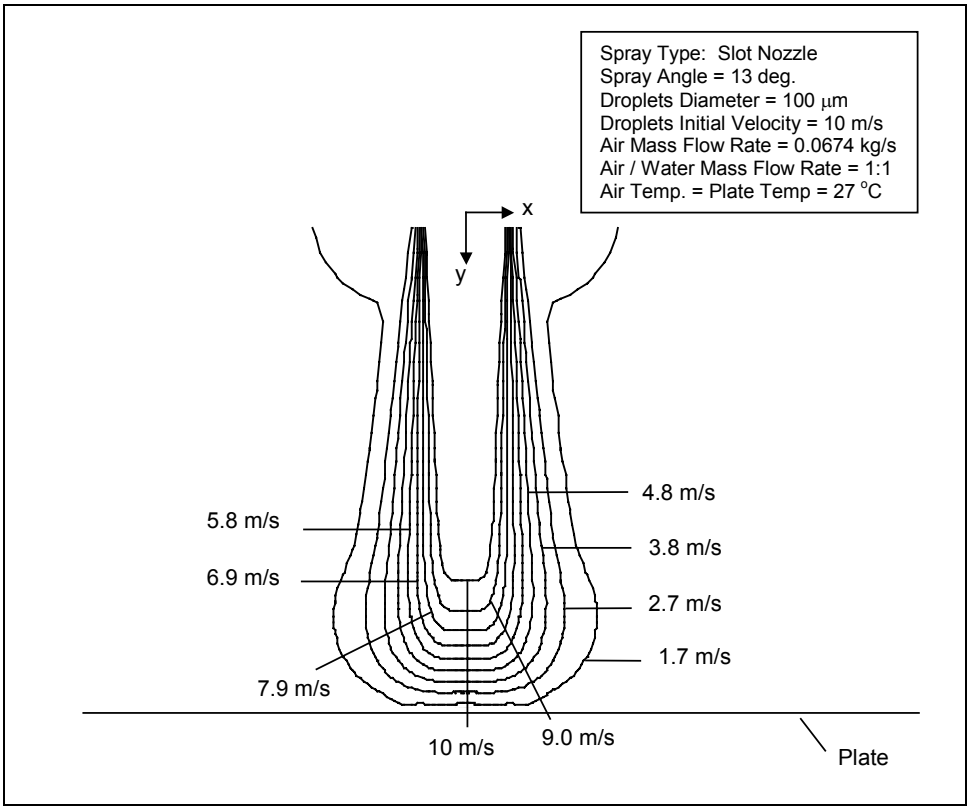

Figure 5.5 Contour of the air velocity profile in the vertical direction

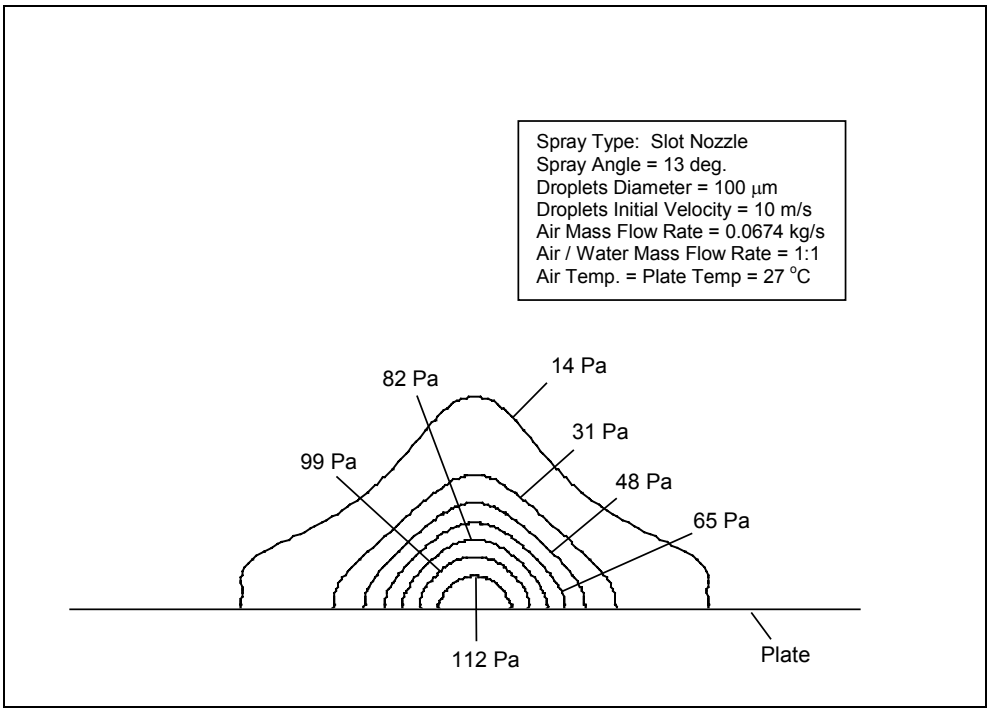

Figure 5.6 Static contact pressure for bulk-air spray

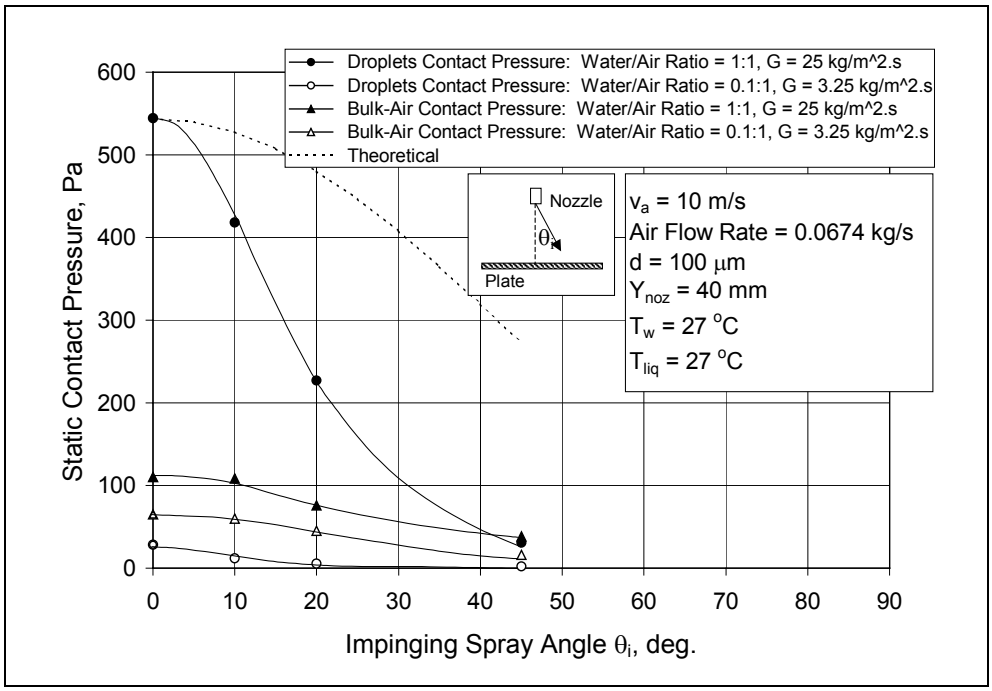

Figure 5.7 Contact pressure for droplets and bulk air

5.2 Heat Transfer Phenomena

5.2.1 Thermal Boundary Layer for Single Droplets

The development of the thermal boundary layer depends on the amount of water vapor generated at the heated surface. Figures 5.8 (a) through 5.8 (d) show the effect of the size of a single droplet on the development of the thermal boundary layer. This is the case where a single droplet is injected at a very low incoming speed, and the surface temperature is low so that perfect wetting occurs. The droplet trajectory is terminated at the surface where the droplet completely evaporates. Because the vapor specific volume is greater than the water specific volume by a factor of about one thousand, there is a tremendous amount of vapor generated at the wall. Figure 5.8 shows four cases for different single droplet diameters. The thermal boundary layer starts to bulge for large droplet diameters, up to a certain point where the boundary layer bursts and the thermal plume overshoots. This overshooting phenomenon has a localized effect on the medium in the vicinity of the wall as compared to a much wider surface spread effect before bursting occurs.

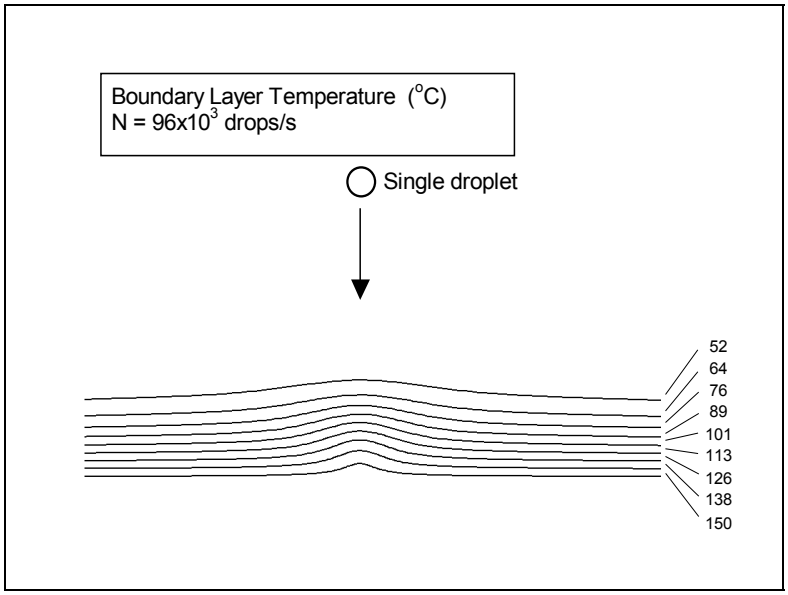

Figure 5.8 (a) Thermal boundary layer developed from a single droplet evaporated at impact (d = 100 μm)

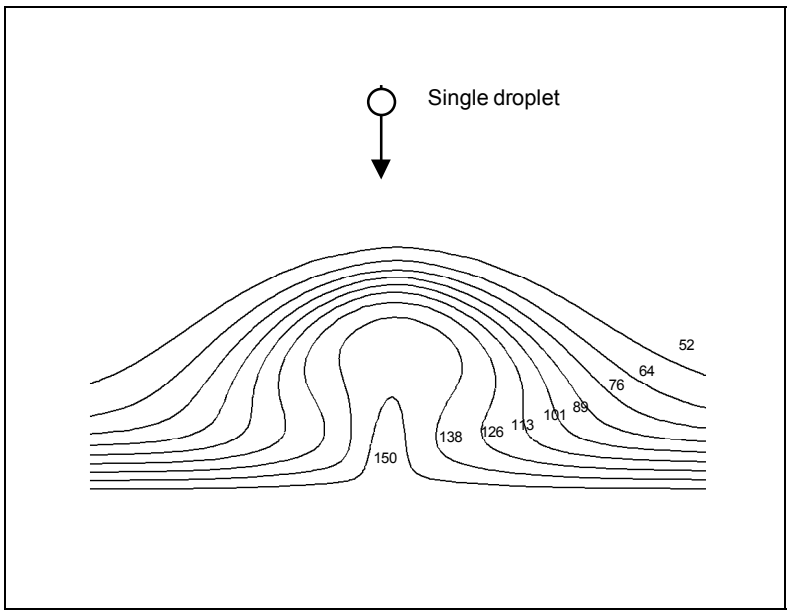

Figure 5.8 (b) Thermal boundary layer developed from a single droplet evaporated at impact (d = 150 μm)

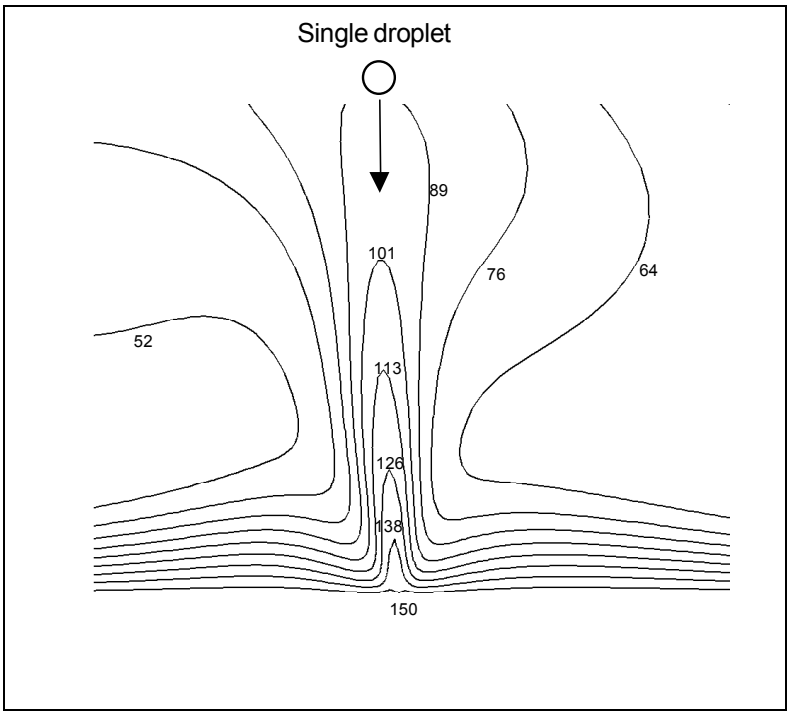

Figure 5.8 (c) Thermal boundary layer developed from a single droplet evaporated at impact (d = 200 μm)

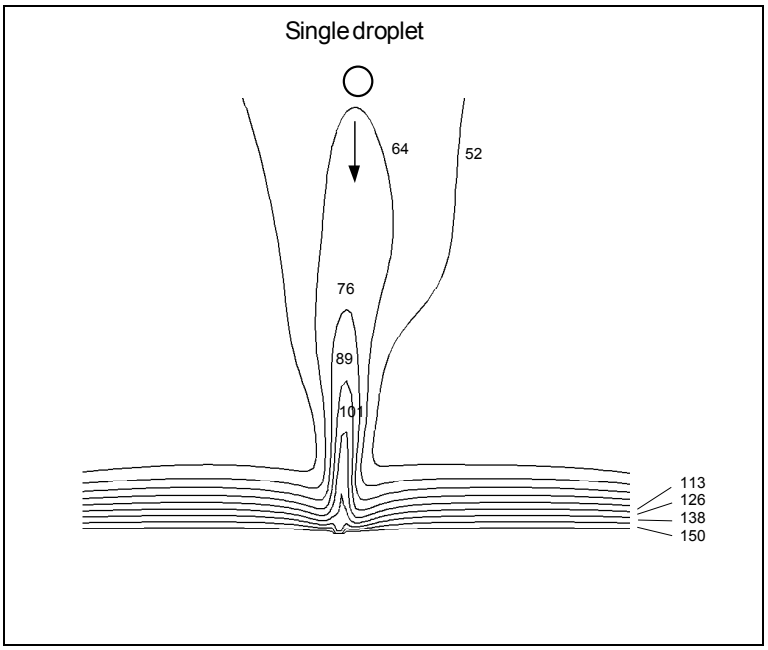

Figure 5.8 (d) Thermal boundary layer developed from a single droplet evaporated at impact (d = 300 μm)

5.2.2 Thermal Boundary Layer for a Full Spray

Using a full spray, the profile of the thermal boundary layer shows a minimum at the stagnation point. Simulation results are presented in Figure 5.9 for a full conical spray with mono-size droplets (uniform droplets) of 400 μm impinging on a heated metal plate. The thermal boundary layer is shown to have a minimum thickness beneath the spray center, but increases towards the edges. This is due to two factors: the maximum flow flux at the plate center that results in maximum cooling, and the fact that the generated steam is being pushed further away from the plate center by the newly incoming droplets.

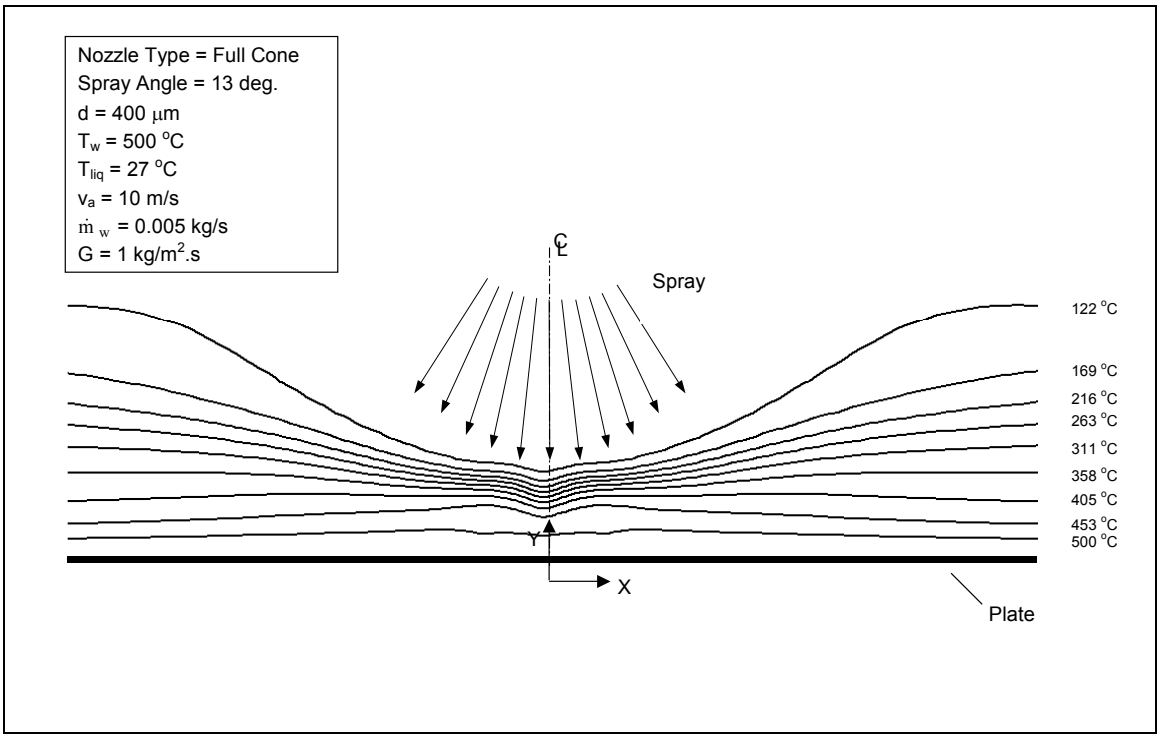

Figure 5.9 Thermal boundary layer for a full spray

5.3 Comparison with Experimental Data

5.3.1 Droplet Distribution in the Spray

The current model for the droplet contact heat transfer and dynamic interaction with the wall was developed based on empirical correlations for a single stream of water droplets. It would be then interesting to simulate an actual full spray test to compare the results, and to check against the validity of the model. The model is tested by simulating the spray experiment that was conducted by Chang and Yao [18]. In this experiment, a full conical spray was injected on a stainless steel plate of 101.6 mm in diameter, and 1 mm in thickness. Figure 5.10 shows a schematic of the nozzle system. It consists of an air-mist nozzle by Spraying Systems, surrounded by an air chamber. The reason for the extra air flow is to produce finer droplet size in the spray. The nozzle was situated at a distance of 40 mm above the plate. The air velocity exiting the air chamber ranged between 0 and 50 m/s. The liquid flow flux at the plate center (stagnation point) ranged between 2.5 and 7.5 kg/m^2s. For these flow parameters, the nozzle spray angle was 13^o. The spray angle was found to increase slightly with the increase in either the liquid or air flow rate. The plate was heated to 525 ^oC.

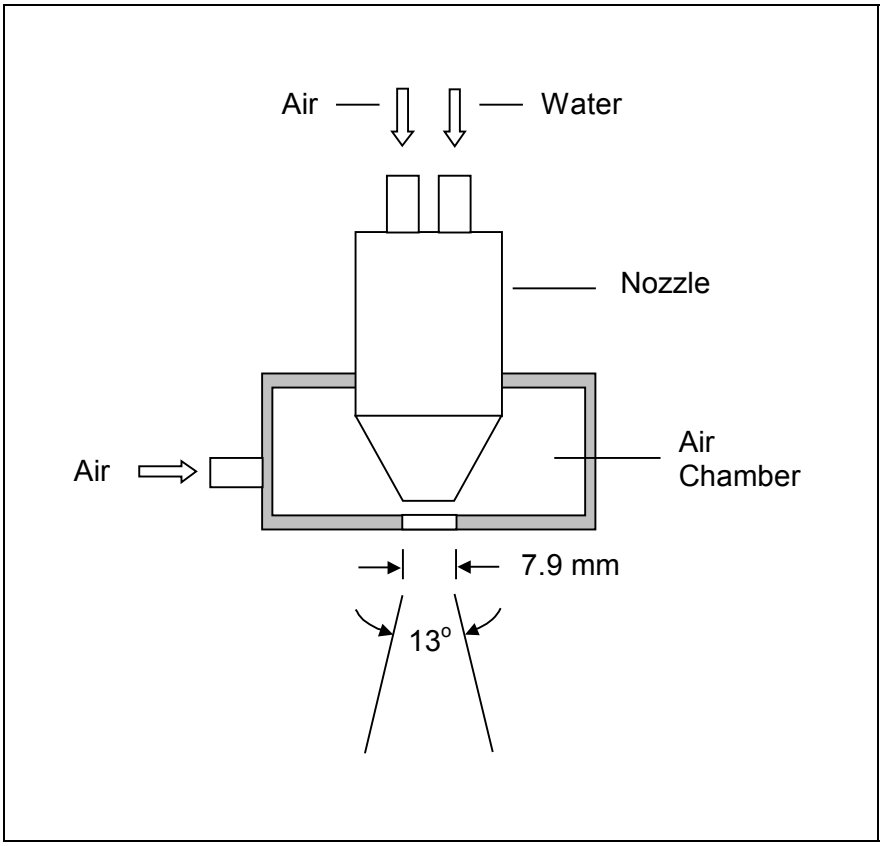

Figure 5.10 Schematic of the nozzle used in the experiment by Chang and Yao [18]

The droplet distribution count in this spray was experimentally determined by Sozbir and Yao [17] and is shown in Figure 5.11. This droplet distribution corresponds to an operating air and water gauge pressures of 14 and 10 psig, respectively. Based on the droplet size count, the average droplet diameter by volume was estimated to be about 19.2 μm, while the average Rosin-Rammler diameter was 40 μm. The Rosin-Rammler droplet distribution is based on the assumption of an exponential relationship between the droplet diameter d and the mass fraction, M_d, of droplets with diameter greater than d. This mass fraction relationship is given by the following expression [60]:

$$M_d = e^{-(d/\bar{d})^n} \tag{5-1}$$

Where n is defined as the spread parameter for the Rosin-Rammler distribution. Based on the droplet spray distribution, n was calculated to be 2.3. Figure 5.12 shows the Rosin-Rammler distribution of the droplets.

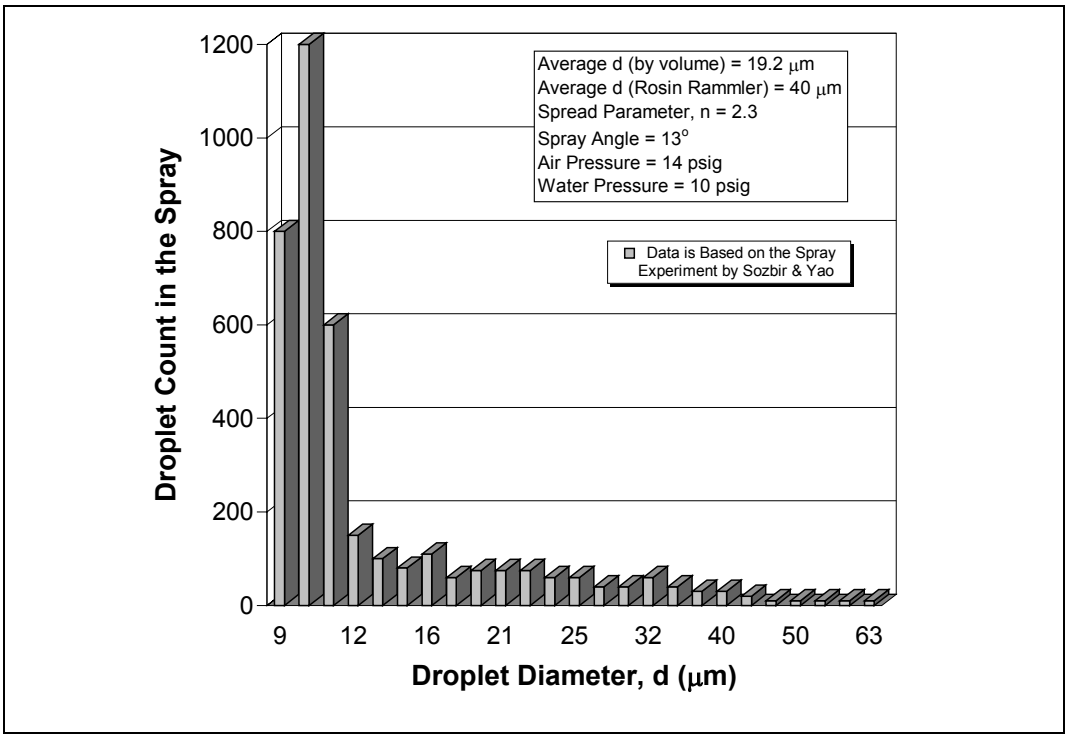

Figure 5.11 Droplet count distribution (Based on the experiment by Sozbir and Yao [17])

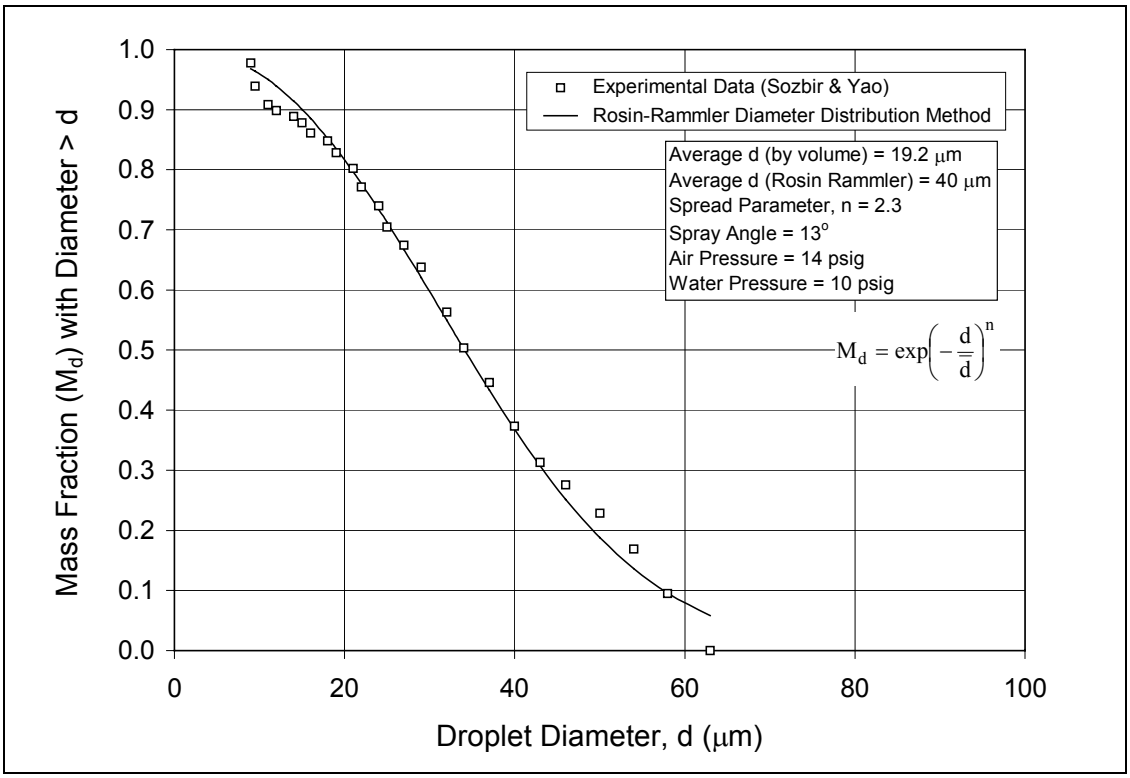

Figure 5.12 Rosin-Rammler distribution of the spray shown in Figure 5.11

5.3.2 A Detailed Comparison for the Heat Transfer Using a Full Conical Spray

Figures 5.13 shows a comparison between the simulated test and Chang's experimental data. The model was first tested to simulate the bulk air heat transfer coefficient as function of the air velocity at the stagnation point. As shown in Figure 5.13, the model's results compared very well with Chang's experimental data and with the correlation for air flow by Graham and Ramadhyani [62] which is given by the following expression:

$$h_a = \frac{k_a}{d_{noz}}\left(Re^{0.5}\, Pr_a^{0.4}\right) \tag{5-2}$$

Where,

$$Re = \frac{v_a d_{noz}}{\nu_a} \tag{5-3}$$

Next, water droplets were injected in an air stream (Figure 5.14), and the results were also promising. The only deviation in the data occurred towards the edge of the plate where the model predicted fewer droplets to surface interaction. The mist heat transfer coefficient was calculated by subtracting from the total heat transfer coefficient the contribution due to radiation and bulk-air heat transfer. Figure 5.15 shows a comparison between the mist heat transfer coefficient as calculated using the model versus the test data by Chang and Yao for different liquid mass fluxes. The deviation between the calculated and test data occurred at higher liquid mass fluxes (~8 $kg/m^2.s$) due to the flooding that becomes more significant at higher liquid mass fluxes.

Figure 5.16 shows a comparison between the experimental data and the model simulation using: 1) the real nozzle spray with non-uniform (multi-size) droplet diameter distribution (Figure 5.11), and 2) a mono-size droplets spray of 15, 20 and 50 μm. For the mono-size droplets spray, the cooling is non-uniform and fine droplets cannot make direct contact below the jet impingement point due to the air drift. The finer the droplet size, the further away from the jet impingement point they contact the wall. However, for the real non-uniform (multi-size) droplet distribution spray the droplets will make contact at random locations with the largest droplets hitting in the vicinity of the jet impingement point and the smaller droplets hitting further away, resulting in very uniform cooling. Figure 5.17 shows the effect of using a spray with non-uniform droplet distribution (multi-size droplets) on the cooling profile. For a spray with non-uniform droplet distribution but the average droplet size is large (such as the case of a multi-size droplet distribution with an average droplet size of 60 μm, as shown in Figure 5.17), for the same mass flux, the droplet density will be low and the droplets will contact the wall at scarce locations with the largest droplets in the vicinity of the jet impingement point (stagnation

point) because of the high droplet inertia. Thus, the heat transfer profile will be non-uniform with extreme cooling around the jet impingement point. On the other hand, for the same mass flux but with a smaller average droplet size (such as the case of a multi-size droplet distribution with an average droplet size of 19 μm, as shown in Figure 5.17), the droplet number density will be much higher and so would be the droplet surface to wall surface contact area. Therefore, the cooling will be more uniform.

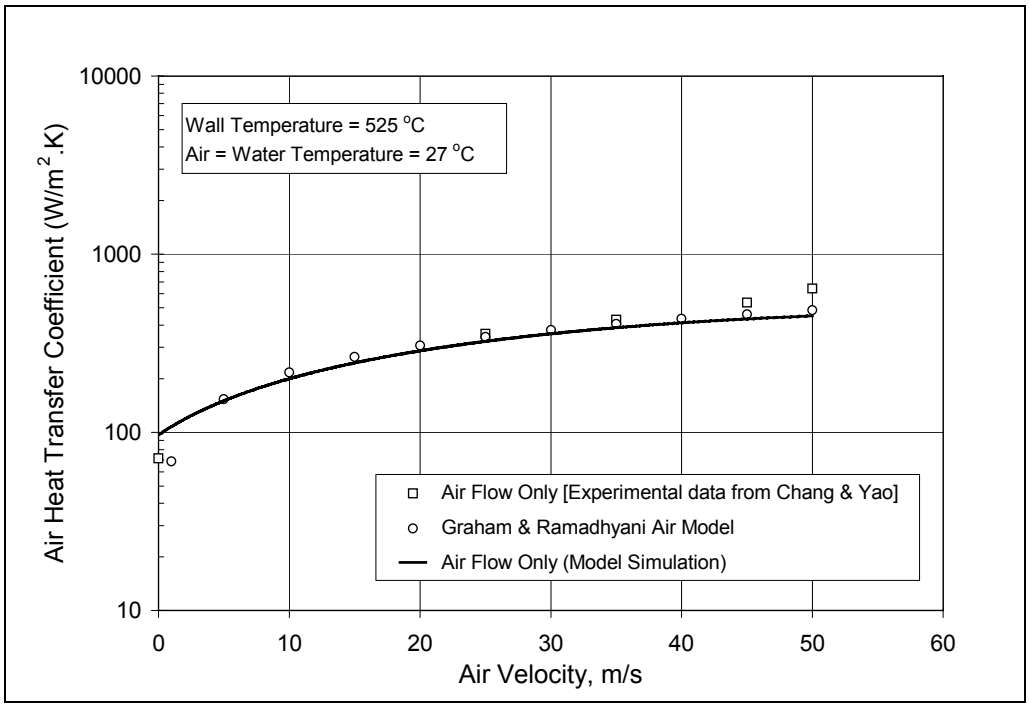

Figure 5.13 Simulation of the air heat transfer coefficient versus actual test data for a conical spray

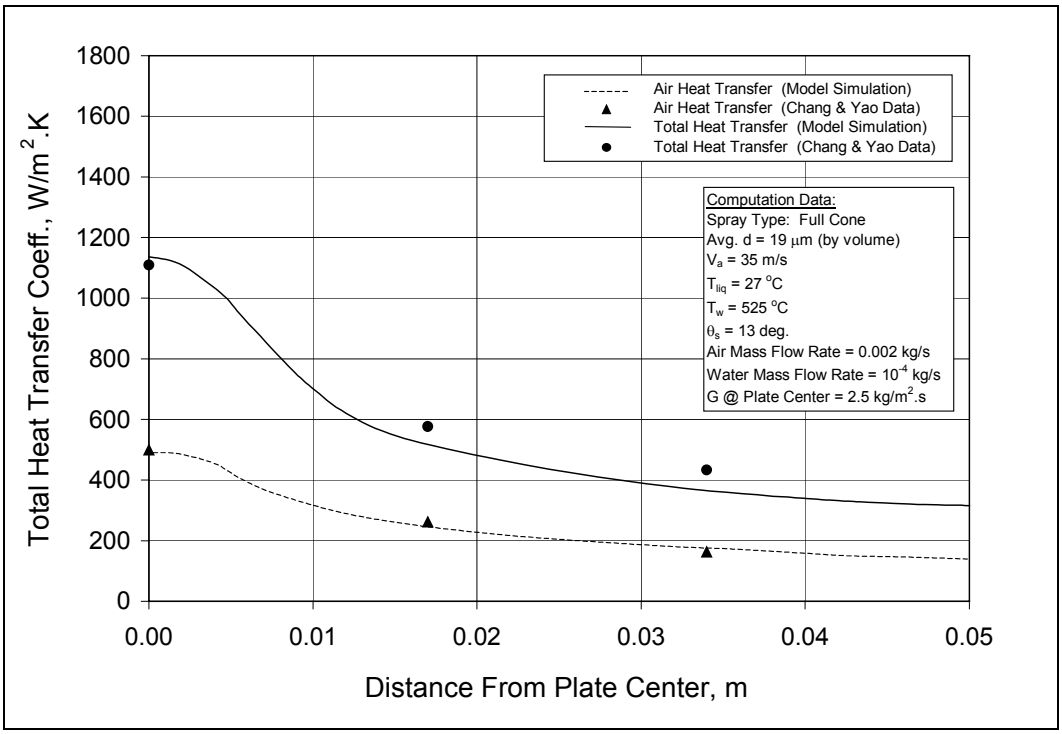

Figure 5.14 Simulation of the total heat transfer coefficient versus actual test data for a conical spray

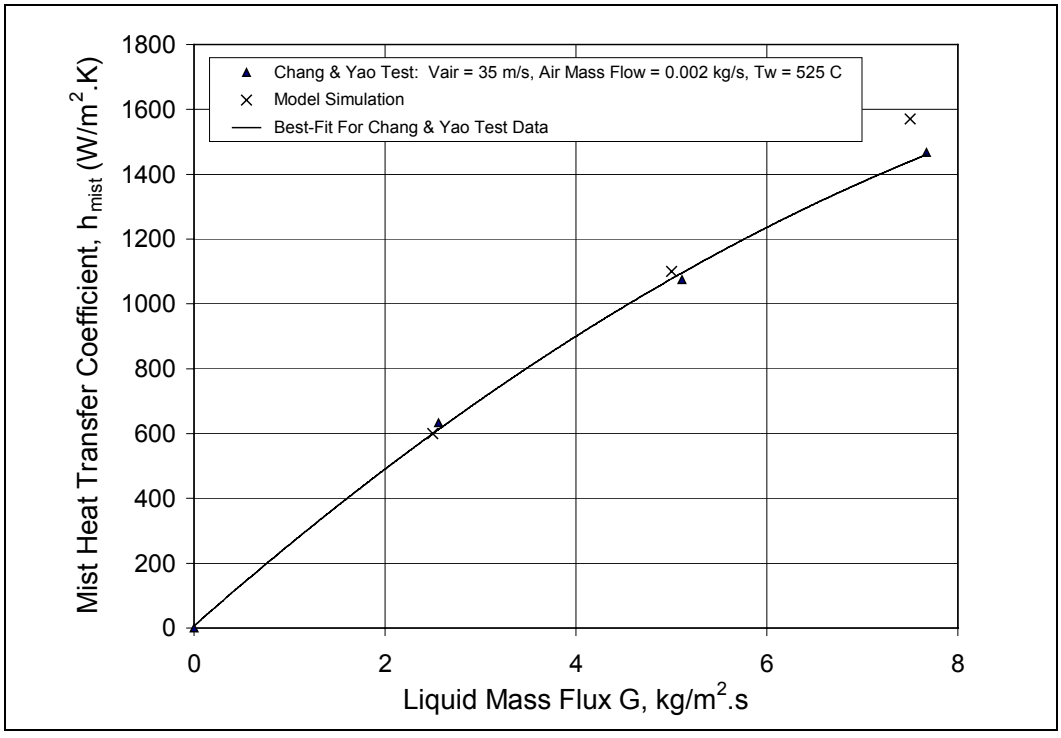

Figure 5.15 Mist heat transfer versus liquid mass flux

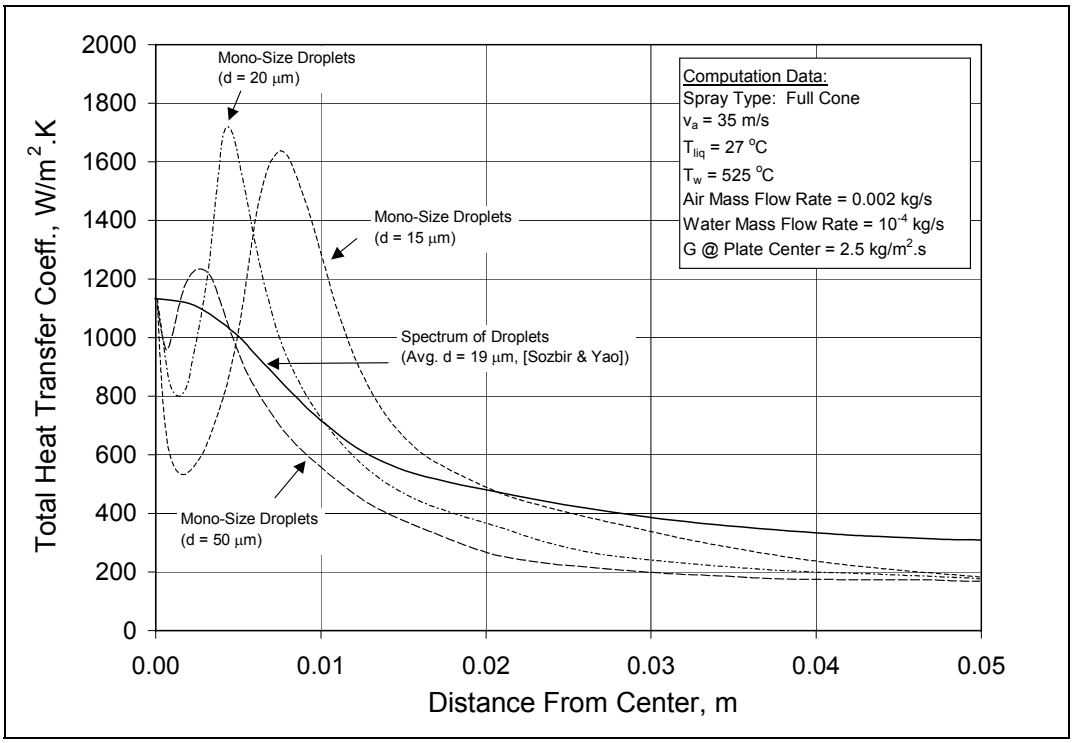

Figure 5.16 Comparison in heat transfer coefficient using a spectrum of spray droplets versus a mono-size droplet spray

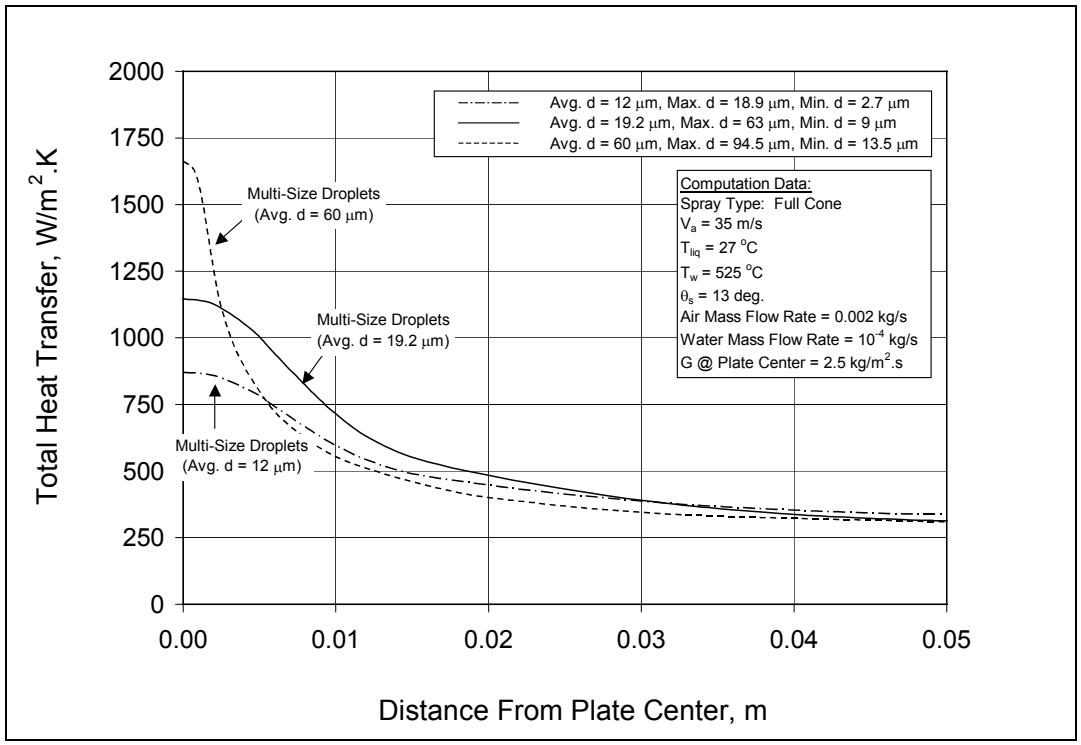

Figure 5.17 Effect of various multi-size droplets spray on the cooling profile

5.3.3 Mist Heat Transfer for a Wide Range of Spray Densities

For a further validation of the model, model simulations for a wide range of spray densities were also compared against experimental data from a variety of sources. Ortiz and Gonzalez [19], and Ohkubo and Nishio [20] have experimentally determined the total heat flux for certain spray operating conditions as shown in Figure 5.18. The total heat flux presented here is the sum of the radiation, bulk air, and droplet contact heat fluxes. A base-line case was created from the averaged conditions (nozzle exit We = 230, d = 100 μm, T_w = 150 ^oC) and was simulated for dilute and dense sprays. According to Deb and Yao classification of sprays [47], a spray is considered dilute if the mass flow flux is less than 2 $kg/m^2.s$, and dense if it is greater than that. The experimental data and the model prediction for the base-line case were plotted against the liquid mass flux. The model predictions below 2 $kg/m^2.s$ were quite satisfactory. Above 2 $kg/m^2.s$, the model slightly over predicted the heat flux. This is because the experimental data shows a trend of heat transfer saturation at higher mass fluxes caused by the droplet-to-droplet interaction at dense sprays. This phenomenon was not accounted for in the current numerical model. Also shown in Figure 5.18 are the model predictions for the maximum possible heat flux. This condition is a theoretical one, and only exists for perfect wetting where all the droplets evaporate at impact.

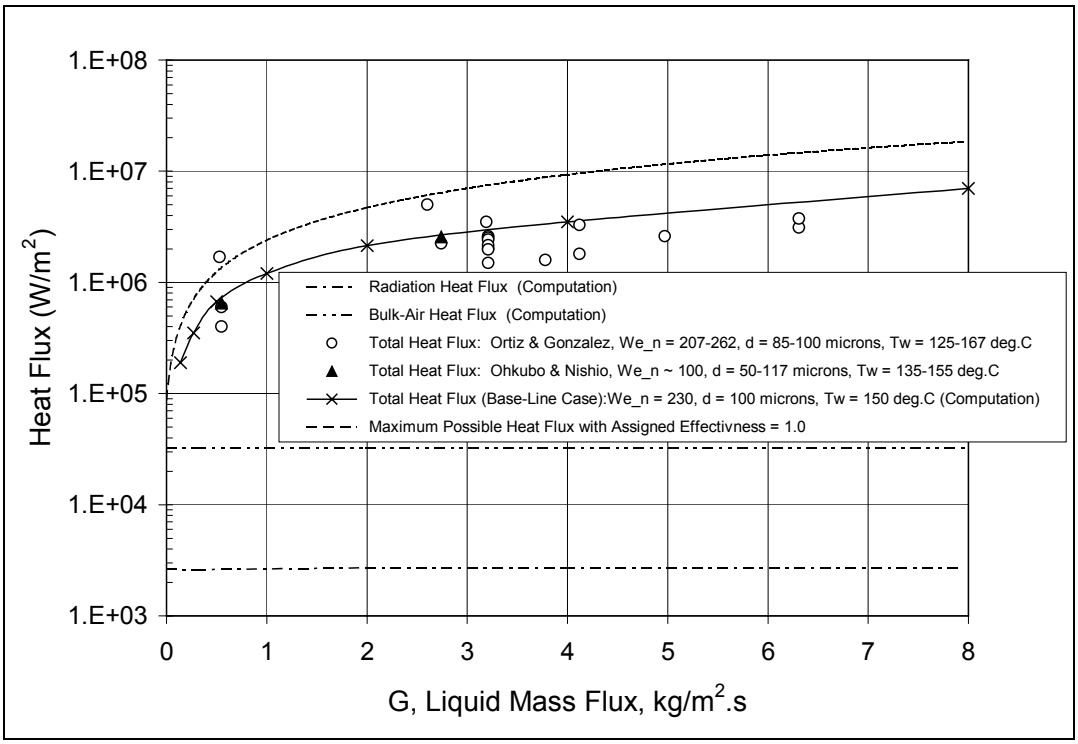

Figure 5.18 Experimental versus computational heat flux for various liquid mass fluxes

6.0 NUMERICAL SIMULATION FOR HIGH AND SUB-ATMOSPHERIC PRESSURE CONDITIONS

6.1 Thermal Boundary Layer

The development of the thermal boundary layer is strongly affected by the ambient pressure. Figures 6.1 (a) through 6.1 (d) show the thermal boundary layer developed from the complete evaporation of a single droplet (150 μm in diameter) on a heated wall at ambient pressures of 0.1, 1, 5, and 10 atmospheres. The vapor that is generated from the droplet evaporation results in a thermal plume that is well developed at atmospheric and sub-atmospheric pressures, but is more suppressed as the ambient pressure increases. This is because of the fact that as the pressure increases so does the vapor density, which results in a decrease in the specific volume of the vapor in the flowing plume. As a result, the thermal plume becomes more confined to the wall proximity; thus, a much thinner thermal boundary layer thickness develops at higher pressures. Figures 6.2 (a) through 6.2 (d) show the thermal boundary layer developed from the complete evaporation of a larger droplet size of 300 μm in diameter. With the larger diameter, more vapor is generated such that an eruption in the thermal boundary layer occurs. At lower pressures, the eruption is narrowly focused over a smaller area and overshoots with much higher speed, while at higher pressures the eruption diffuses at a slower rate over a larger area but remains in a closer proximity to the heated wall. As the hot gas (thermal plume) is ejected away from the wall, colder air circulates to displace the hot gas. This results in an increase in the

thermal gradient across the wall, which causes an increase in the wall heat flux and, therefore, improves the cooling efficiency.

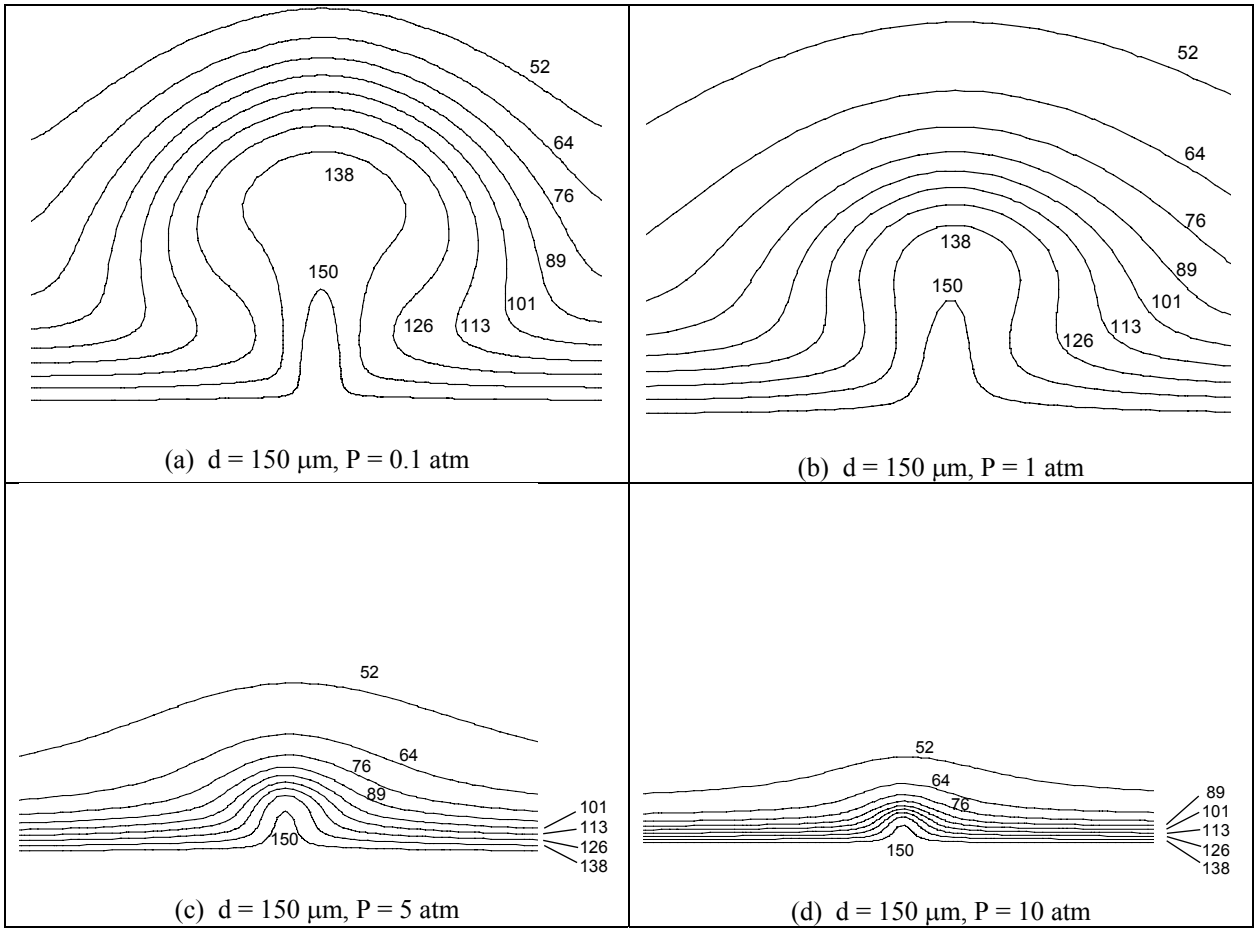

Figure 6.1 Thermal boundary layer developed from single droplet evaporation (Temperature in ^{o}C)

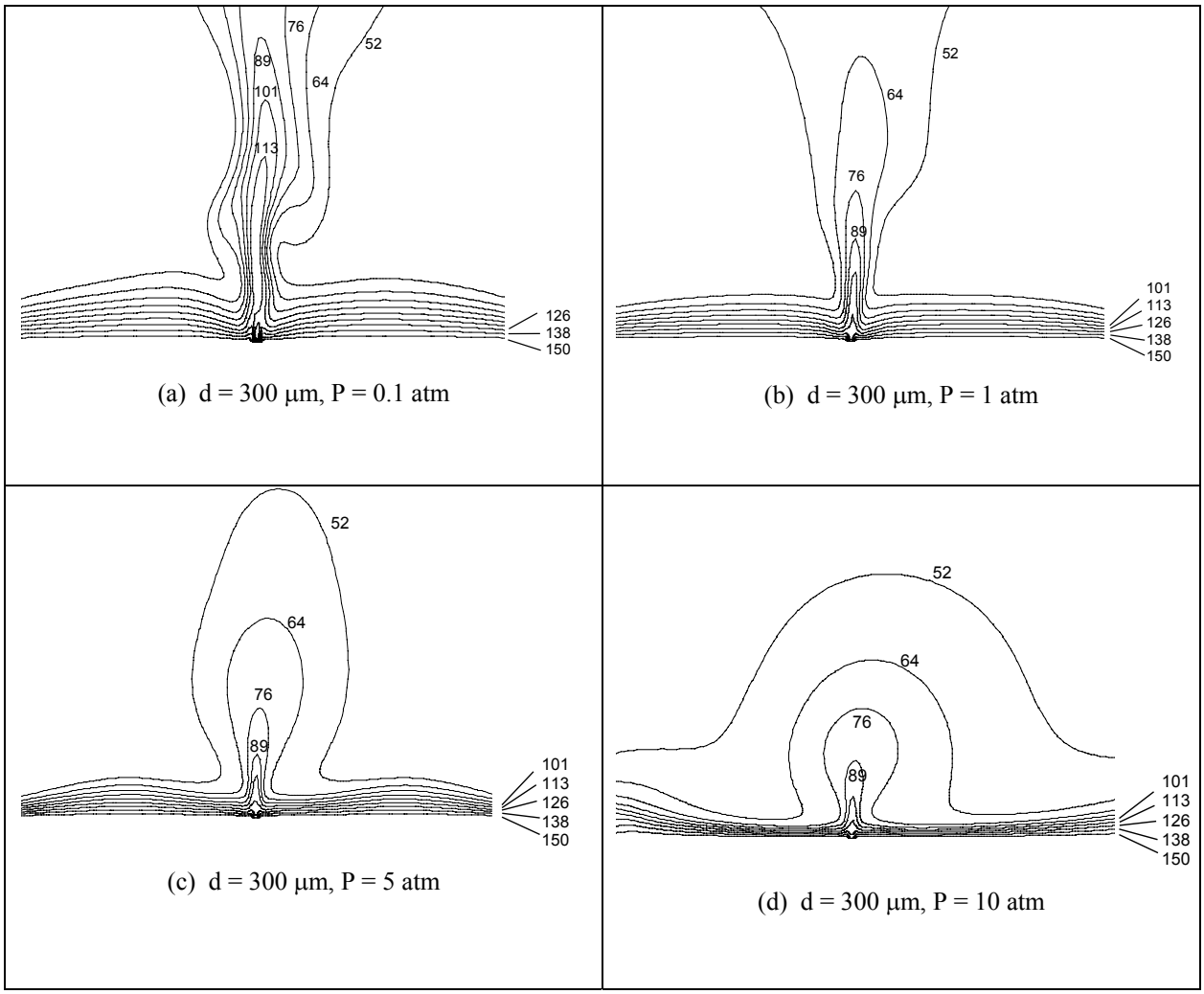

Figure 6.2 Thermal boundary layer developed from single droplet evaporation (Temperature in ^{o}C)

6.2 Droplet-Wall Interaction for Stream Impingements

Figures 6.3 (a) through 6.3 (f) show the model's simulation of the droplet evaporation history as it impinges on a heated surface under different ambient pressures. In this case, the droplet is ejected with an initial diameter of 200 μm, and the surface temperature is held at 525 ^{o}C. During its trajectory, the droplet undergoes transient heating. As the pressure increases, the water at the droplet surface evaporates more easily due to the much-reduced latent heat of vaporization. As a result, the droplet size reduces quickly during the flight, as the figures show. It should also be noted that as the pressure increases, the heat transfer mode also changes. For the case of 1 atm (Figure 6.3 (b)), the droplet impinges on the surface with non-wetting contact (film boiling). As the pressure increases while keeping the surface temperature held at 525 ^{o}C (Figures 6.3 (c) through 6.3 (f)), the droplet contact heat transfer mode shifts closer to the wetting regime. This causes an increase in the droplet heat transfer effectiveness, and the droplet to evaporate faster. On the other hand, as the pressure decreases to sub-atmospheric levels (Figure 6.3 (a)), the heat transfer mode shifts further into the film boiling regime, and therefore, the droplet contact heat transfer effectiveness may decrease more.

It is also shown in Figures 6.3 (a) through 6.3 (f) that the droplet velocity reduces significantly as the pressure increases. This is due to the increase in the ambient density, and therefore to the increase in the drag force acting on the droplet. At higher pressures, the droplet is kept closer to the wall, and the frequency of the droplet impingements increases. The reason for this is that the droplet does not lose a lot of momentum as it impinges on the wall at higher pressures because the droplet Weber number is so small that the droplet impaction is close to an elastic one (where the droplet normal coefficient of restitution ~ 1). This causes an increase in the number of impingements until the droplet eventually completely evaporates.

A stream of droplets with the following diameters: 10, 48, 86, 124, 162 and 200 μm were injected into an air stream. The air and water mass flow rates were 0.028 and 1.2×10^{-3} kg/s, respectively. The surface temperature was held at 525 ^{o}C. Simulation was generated for the following ambient pressures: 0.5, 1, 2, 5, 10 and 30 atm. Figures 6.4 (a) through 6.4 (f) show the interaction between the droplet stream and the heated wall for the different ambient pressures. In all the cases, the 10 μm droplet was too small to make it to the surface. As a result, it drifted along the streamlines and evaporated. The evaporation occurred much quicker as the pressure increased because of the decrease in the latent heat of vaporization. With the increase in ambient pressure, droplets with larger diameters also completely evaporated. For instance, it was observed that at 10 and 30 atm, all the droplets completely evaporated on the surface, and that the evaporation occurred much quicker with higher pressures. As discussed earlier, more vapor was also generated at impaction due to the shift in the droplet contact boiling regime from film boiling at atmospheric pressure to nucleate boiling regime at high pressures. It was also noticed that for all the droplet sizes, the larger the droplet, the higher was the rebound height because larger droplets had higher inertia. It was shown that for all the droplets, the rebound height decreased with the increase in pressure due to the higher vapor density and higher dynamic viscosity of the air.

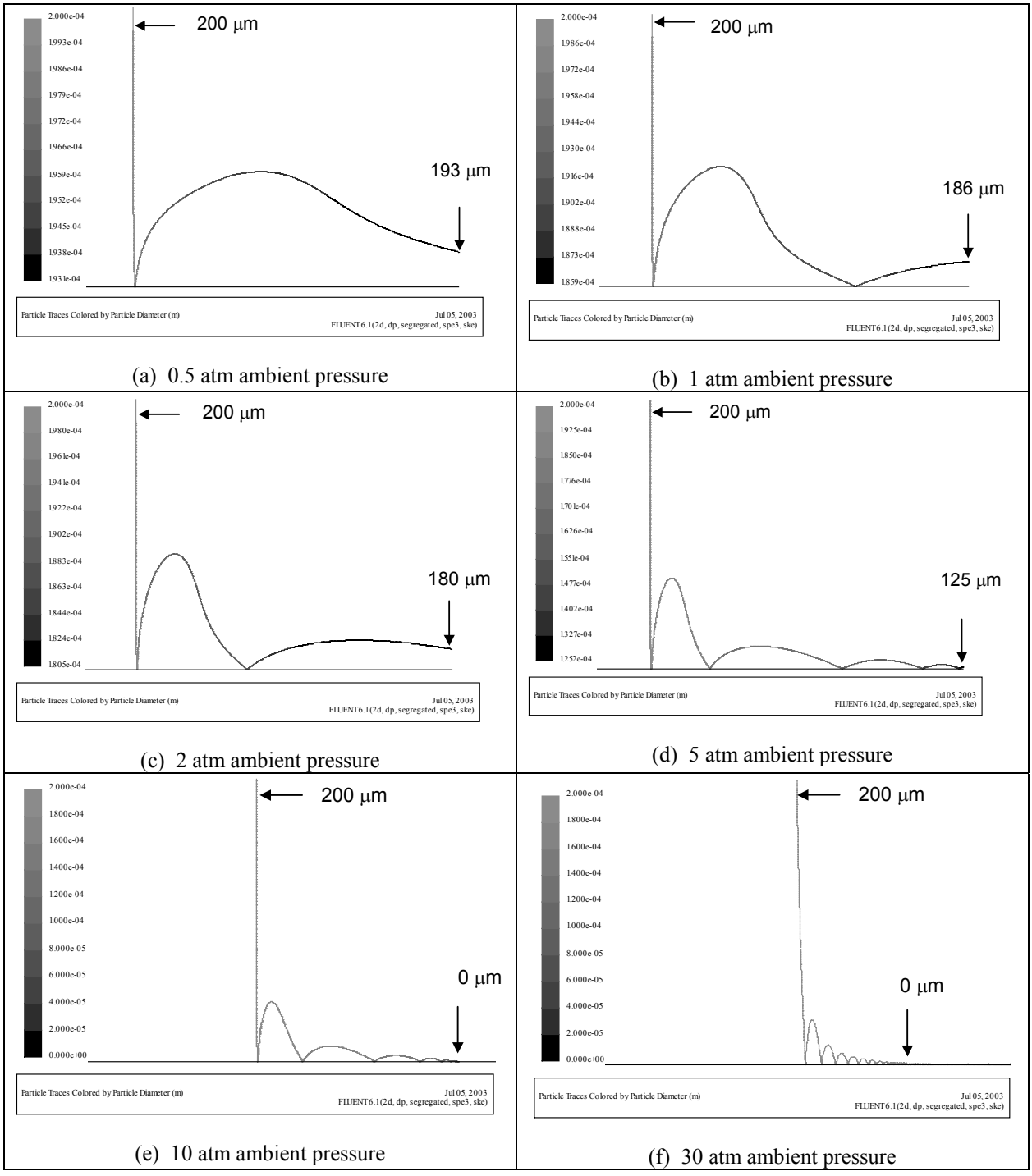

Figure 6.3 Droplet bounce and evaporation for d = 200 μm, T_w = 525 ^oC

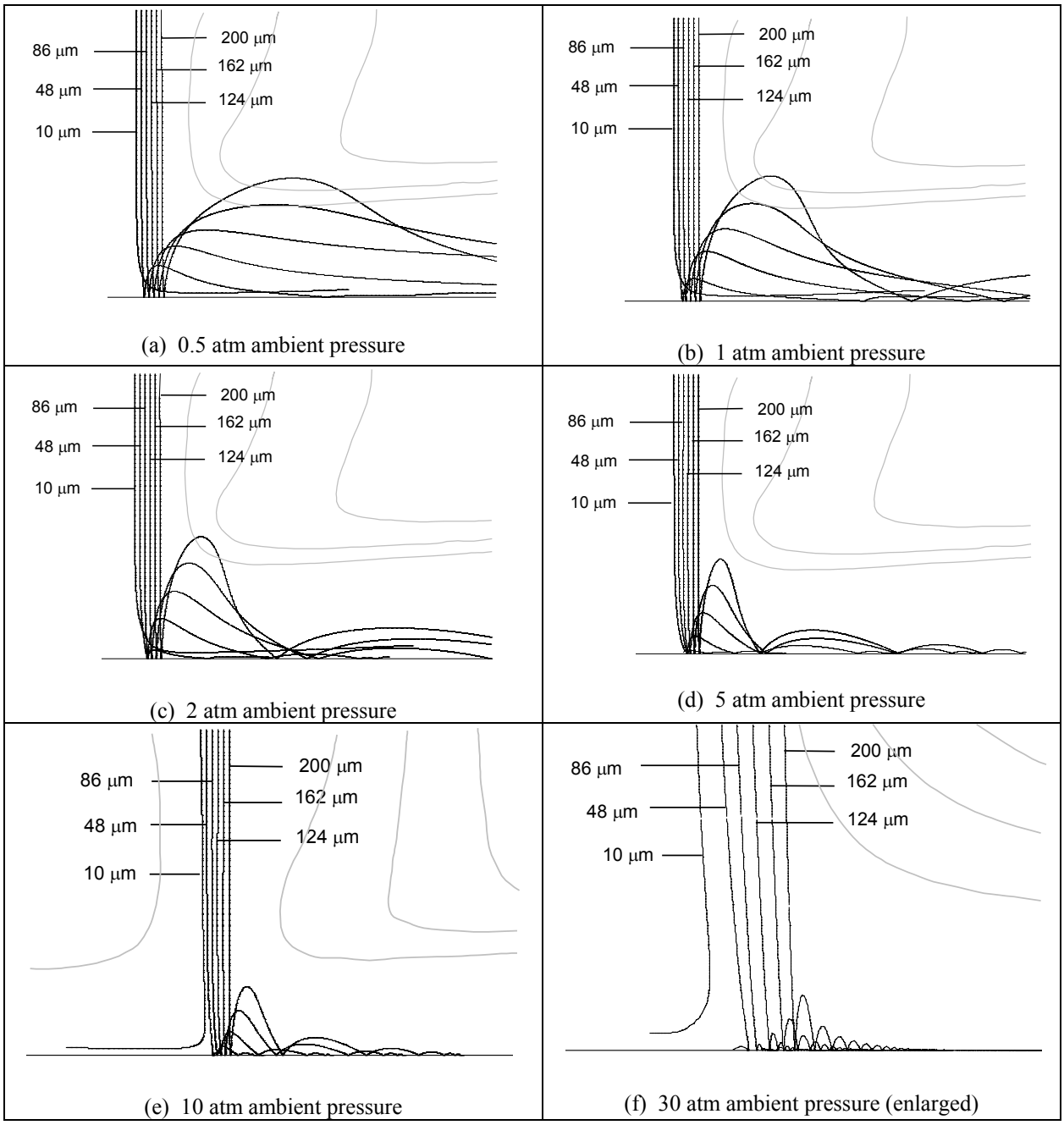

Figure 6.4 Droplet-wall interaction using multiple streams of droplets (T_w = 525 ^oC, mass flow: air = 0.028 kg/s, water = $1.2x10^{-3}$ kg/s)

6.3 Heat Transfer for Single Stream Impingements

New sets of droplet contact boiling curves were developed for various high and sub-atmospheric pressure conditions based on the literature review for droplet impingements. Typical examples for droplet contact boiling curves were shown in Figures 3.17, 3.18 and 3.19 for 0.1, 5 and 50 atmospheres. Incorporating these boiling curves into the numerical model, high pressure and sub-atmospheric pressure conditions can now be simulated. This is implemented with the FLUENT code as an extension of our previous simulation for atmospheric pressure applications.

In order to check for the sensitivity and the validity of the model to the various operating pressures, the spray experiment conducted by Halvorson [22] was simulated. In this experiment, a single stream of droplets impinges on a heated plate with wetting contact. The droplet injections were done in a pressurized chamber using three different gauged needles that produced droplet diameters ranging from 2.3 mm to 3.9 mm. The droplet impact average velocity was about 1.3 m/s, and the droplet mass flux ranged from 0.15 $kg/m^2.s$ to 1.6 $kg/m^2.s$. The heated surface was nickel-plated. The model was simulated for the following chamber pressures: 0.1, 0.5, 1, 2, 5 10, 30 and 50 atmospheres. Experimental data by Halvorson were available for comparison at 0.1, 0.5, 1, and 2 atm. At 5, 10, 30 and 50 atm, the results were based on the model predictions for high operating pressure conditions. Figures 6.5 through 6.8 show the droplet total heat flux (at the critical heat flux point) as function of the mass flow flux for both the experimental data and the model predictions. The total heat flux accounts for the mist heat flux, radiation, and air convection arising from the local evaporation at the surface. Figure 6.9 shows point-to-point comparison between the experimental data and the model predictions. The results reveal a good agreement between Halvorson experimental data and the model predictions.

The almost linear relationship between the critical heat flux and the mass flux shows the spray behaves like an ideal one. The likelihood of the droplets interaction and flooding on the surface is very small at those relatively low mass fluxes (i.e., dilute spray conditions). Figure 6.10 shows the model predictions at 5, 10, 30 and 50 atmospheres (in addition to the results from Figures 6.5 through 6.8) for the total heat flux as function of the mass flow flux. Figure 6.11 shows the total heat flux and droplet contact heat transfer effectiveness at the mass flow flux of 2 $kg/m^2.s$ for the simulated pressures. This mass flux corresponds to the stagnation point in the spray along the wall. The 50 atm ambient pressure was found to produce a 73% increase in the critical heat flux from that at atmospheric pressure for the same mass flux, while the 0.1 atm pressure results in a 60% decrease in the critical heat flux. At 50 atm, the peak in the droplet contact heat flux is very close to the maximum that can be achieved. According to experimental data for pool boiling (shown in Figure 3.16), the peak in the critical heat flux was found to occur somewhere between 1/4 to 1/3 of the critical pressure for water (which is between 54 and 73 atm). For single droplet impaction, the peak in the droplet contact heat flux is also assumed to occur between 1/4 to 1/3 of the critical pressure.

The droplet contact heat transfer effectiveness, which is the ratio of the actual heat transfer induced by the droplet contact to the maximum possible heat transfer that can be achieved, decreases from 0.45 at 1 atm to 0.25 at 0.1 atm, but increases to 0.6 at 50 atm. There was no noticeable change in the heat transfer effectiveness from 30 atm to 50 atm. The reason for this is that based on our definition of the effectiveness, the actual droplet heat transfer and the maximum possible heat removal by the droplet have both increased in similar proportions at these high pressures. The actual droplet contact heat transfer was calculated based on the extrapolation from experimental data (shown in Fig. 3.15). The maximum possible heat removal

by the droplet was calculated based on equation 3-6. At high pressures, as shown in Figure 6.12, the sub-cooling of the droplet has a significant effect on the absorption of heat. This is because of the fact that with the increase in pressure, the saturation temperature also increases, and therefore a large portion of heat is needed to increase the droplet temperature towards the saturation temperature. Figure 6.12 shows that at 50 atm, the droplet sub-cooling accounts to 35% of the maximum possible heat removal by the droplet, compared to 11% at atmospheric pressure and to 3% at a sub-atmospheric pressure of 0.1 atm. The increase in droplet sub-cooling is also accompanied by a decrease in the latent heat of vaporization making droplet evaporation much easier at higher pressures.

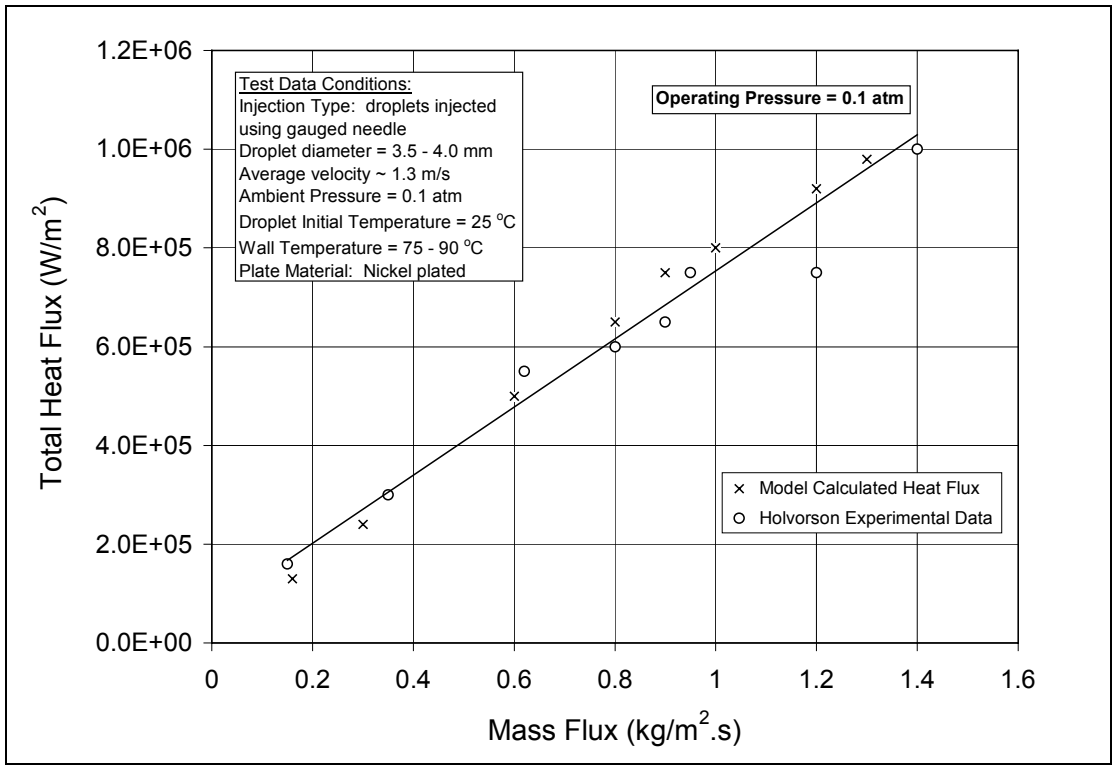

Figure 6.5 Total heat flux versus liquid mass flux for single stream injection at 0.1 atm

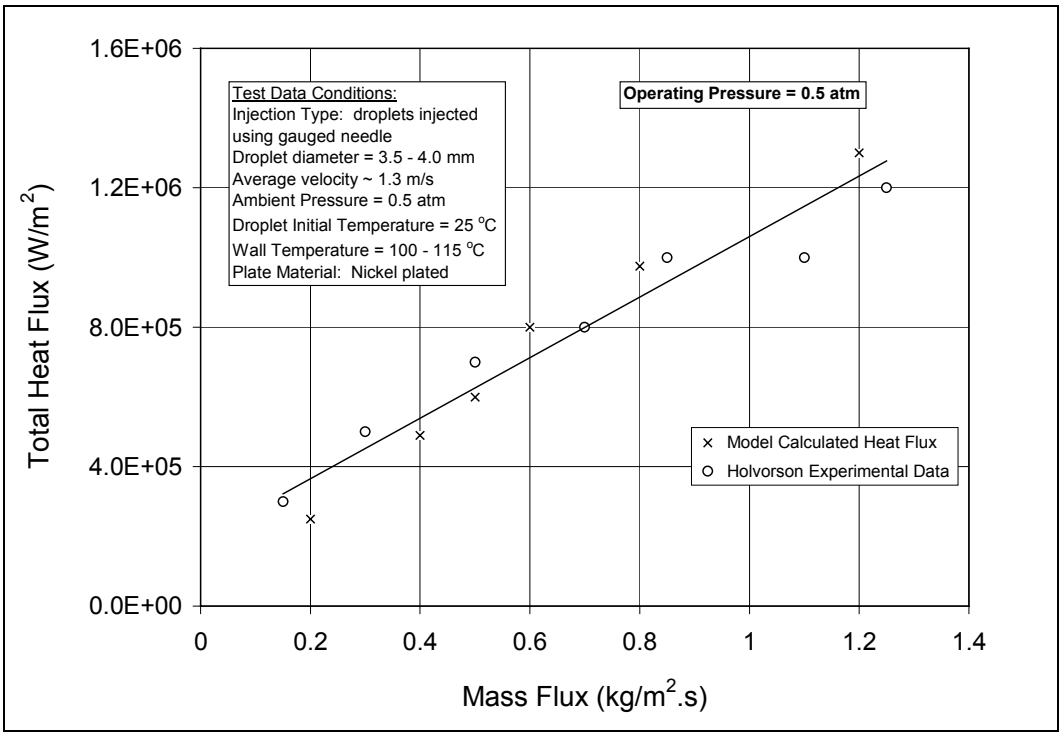

Figure 6.6 Total heat flux versus liquid mass flux for single stream injection at 0.5 atm

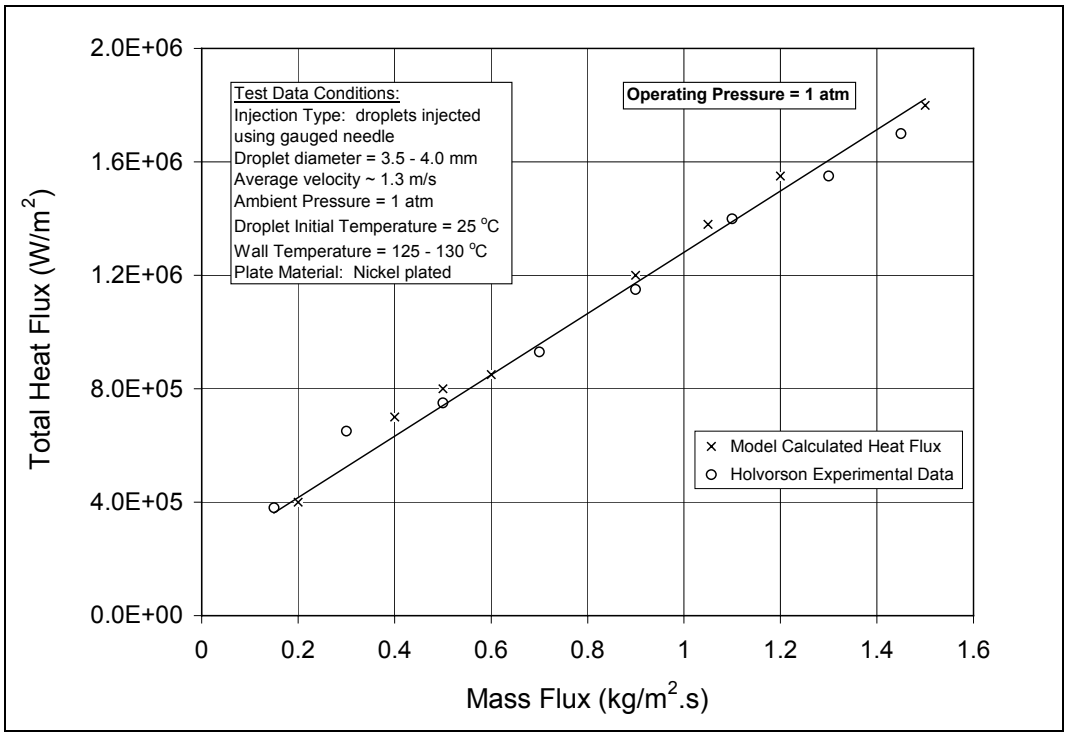

Figure 6.7 Total heat flux versus liquid mass flux for single stream injection at 1 atm

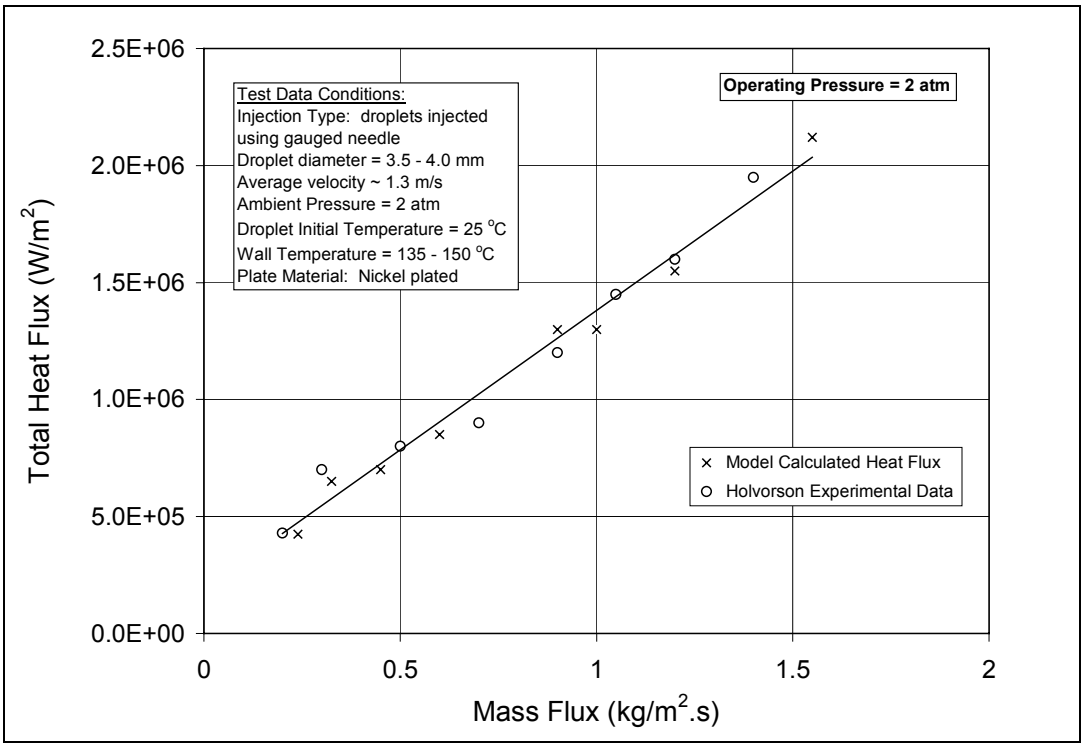

Figure 6.8 Total heat flux versus liquid mass flux for single stream injection at 2 atm

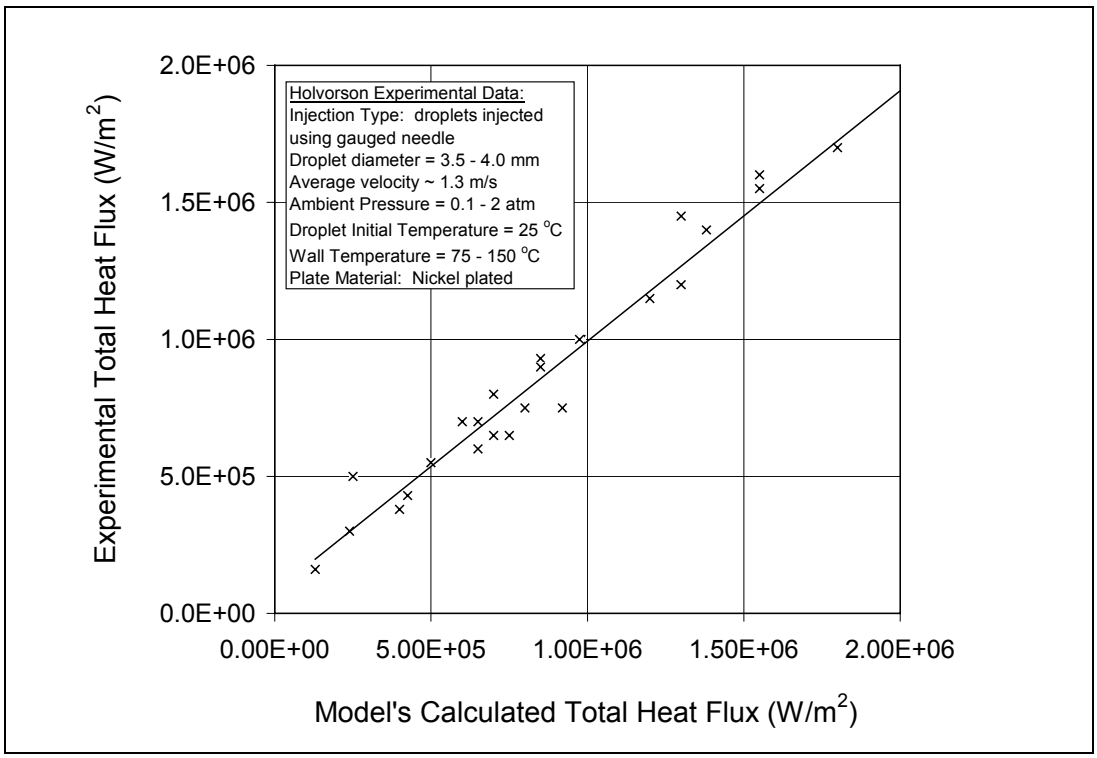

Figure 6.9 Model predictions versus experimental data for single stream injection

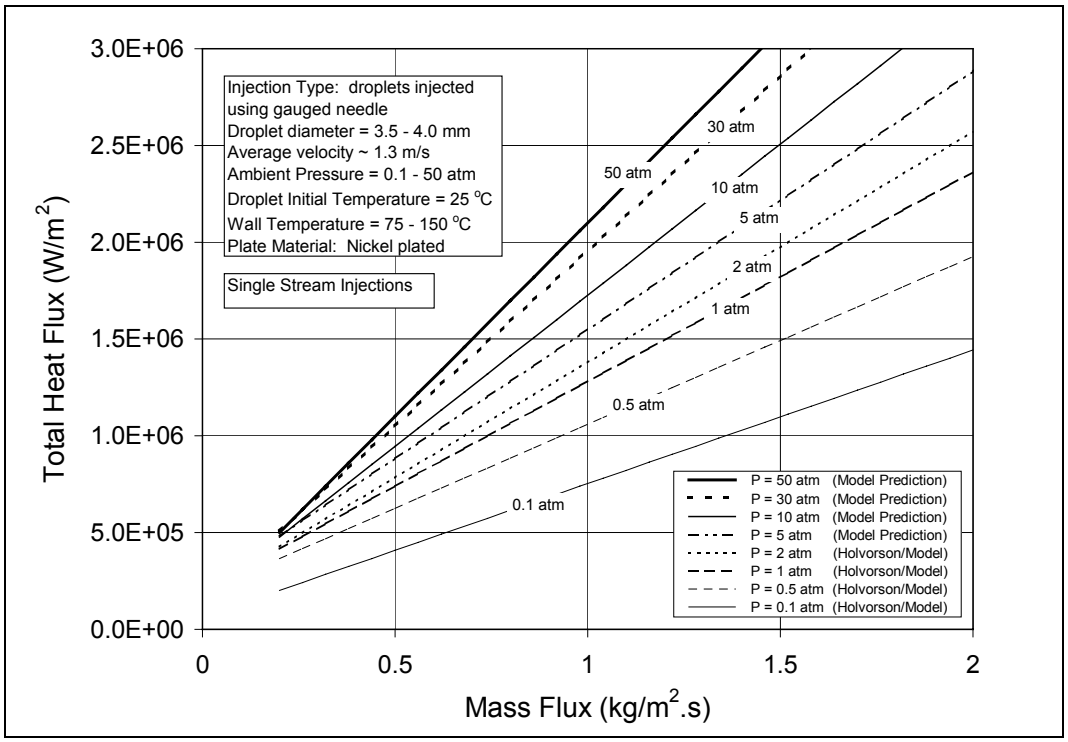

Figure 6.10 Comparison between the total heat flux at various ambient pressures

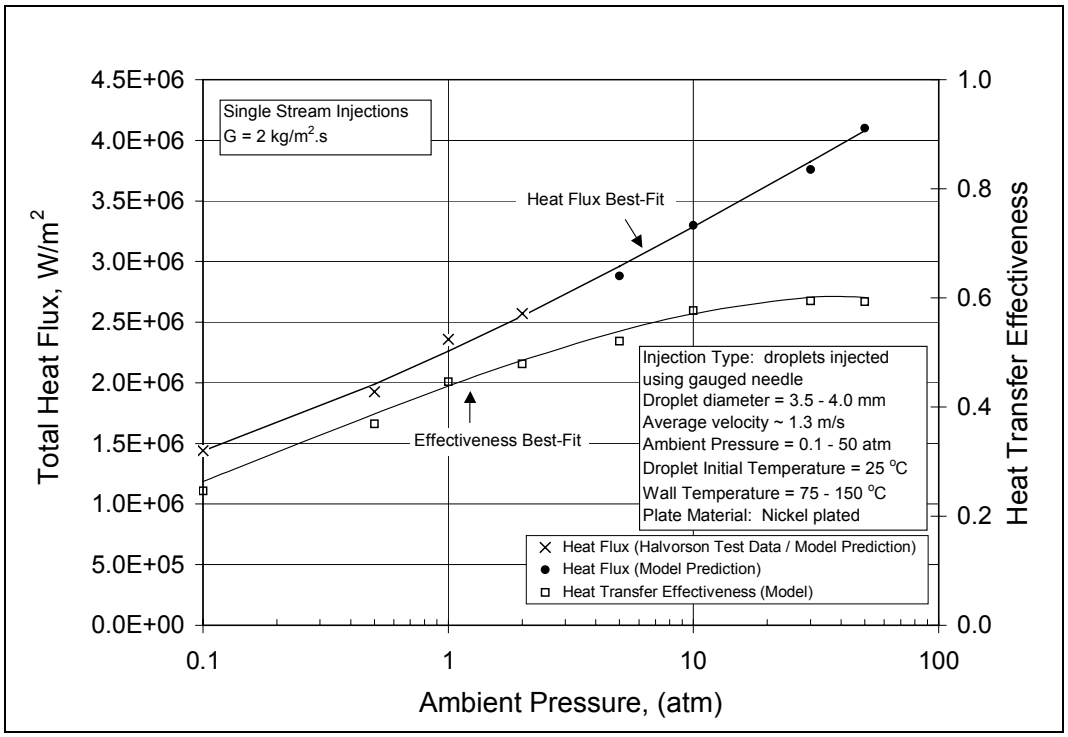

Figure 6.11 Total heat flux and droplet contact heat transfer effectiveness at 2 kg/m^2.s for various ambient pressures

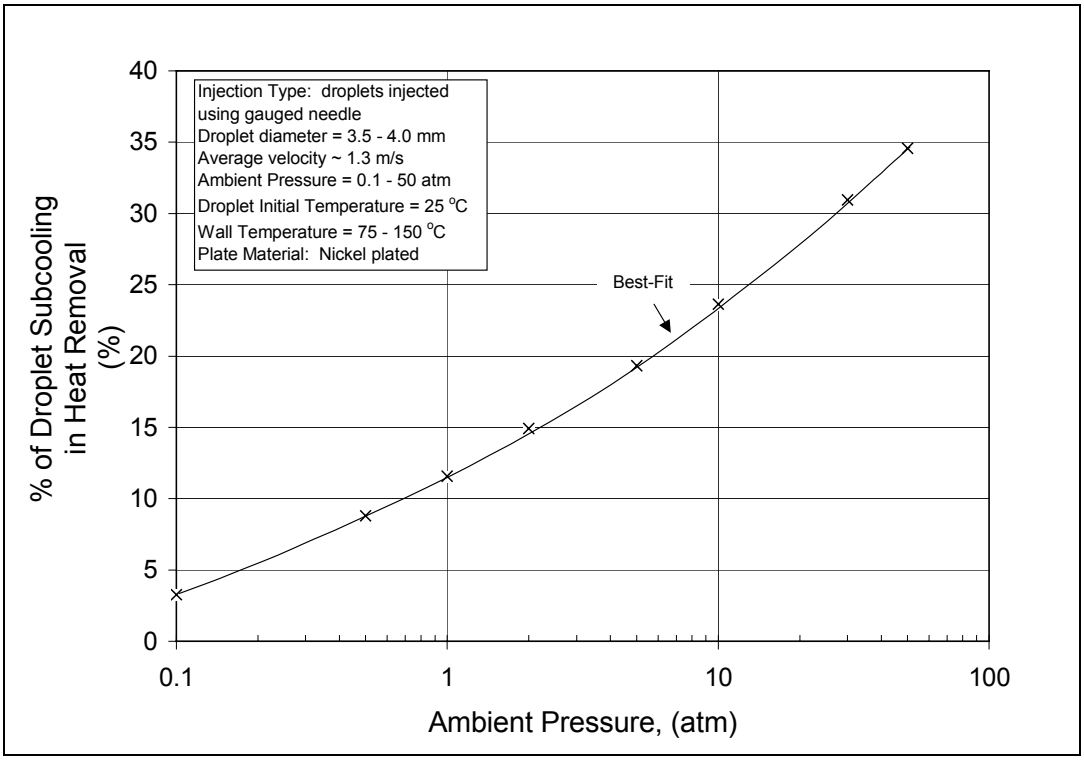

Figure 6.12 Droplet sub-cooling versus ambient pressure

6.4 Heat Transfer for a Full Spray

One of the challenges in air mist cooling is to understand the effect of the droplet size on the heat transfer enhancement and the uniformity of cooling. The droplet size is an important factor because it affects the amount of deposition on the surface. It will be shown that the desirable droplet size to be used in the spray depends strongly on the system pressure.

Figure 6.13 shows the spray mist heat transfer coefficient for the following ambient pressures: 0.5, 1 and 10 atm. In this case a full conical spray type is injected onto a stainless steel plate at 525 ^{o}C. The initial air and droplet temperature is 27 ^{o}C. For all ambient pressures cases, the air and water mass flow rates are $2x10^{-3}$ and 10^{-4} kg/s, respectively. The spray has a spectrum of droplet diameters with an average of 19.2 μm by volume (see Figure 5.11).

Compared to the case at 1 atm, and for the same air and water mass flow rate, simulation of the spray at 10 atm ambient pressure shows the droplets to impinge on the surface at a much-reduced velocity due to the 10 times increase in the air density. The reduction in the droplet speed causes the droplets to scatter over a wide area with more droplets drifting away. Figure 6.14 shows the spray mist at 10 atm, and Figure 6.15 shows the spray mist at 1 atm. Simulation also shows that at 10 atm the droplets evaporate much easier than at 1 atm as they flow through the air stream. Simulation shows that about 65% of the original spray mass evaporated at 10 atm, compared to 15% at 1 atm. This is due to the reduction in the enthalpy of vaporization at 10 atm. Therefore, droplets that make it to the surface, impinge with both a much lower velocity and smaller diameter compared to the case at 1 atm. As a result, the droplet impinging Weber number decreases sharply which in turn causes a drastic decrease in the droplet contact heat transfer effectiveness (as shown in Figure 6.13).

For the low sub-atmospheric pressure of 0.5 atm, and for the same air and water mass flow rate, the droplets are injected with a velocity 2 times greater than that at 1 atm. This is because the air density at 0.5 atm is 50% of that at 1 atm. With a much higher injection velocity at 0.5 atm and with a much less air drag acting on the droplets, the droplets reach the surface with a much higher velocity than the case at 1 atm. This causes a drastic increase in the droplet momentum, and the droplets hit mostly at the jet impingement point. The result is a non-uniform cooling of the surface, with high cooling occurring at the plate center, and a sharp decrease in the cooling further away from the center (Figure 6.13). Figure 6.16 shows the spray mist at 0.5 atm. Simulation shows that about 9.4% of the original spray mass evaporated at 0.5 atm, compared to 15% at 1 atm. This is because at sub-atmospheric pressure, it is more difficult for the droplet to evaporate due to the increase in the enthalpy of vaporization. Therefore, with higher impinging

velocity and with a larger droplet size at impact, the impinging droplet Weber number increases drastically in comparison with the case at 1 atm. The increase in the droplet Weber number causes an increase in the droplet contact heat transfer effectiveness (as was shown in Figure 6.13).

Figure 6.17 shows the mist heat transfer coefficient at 0.5, 1, and 10 atm, whereas in this case, larger droplets size are used in the spray at 10 atm, and finer droplets are used at 0.5 atm. The spray at 10 atm has an average droplet size by volume of 60 μm (min d = 28 μm, max d = 198 μm), while the spray at 0.5 atm has an average droplet size of 7.6 μm (min d = 3.6 μm, max d = 25 μm). At 10 atm ambient pressure, for the same amount of air and water mass flow rate used earlier, and with larger droplets (60 μm compared to 19.2 μm), the spray has lower droplet number density but a higher droplet momentum. Figure 6.18 shows the spray mist at 10 atm. More droplets make impact at the center of the plate (Figure 6.17) than when finer droplets are used (Figure 6.13), and the number of droplets that drift decreases sharply. With larger droplets, the impinging Weber number increases, and the chances that the droplets would make multiple impingements also increases. This causes an increase in the droplet contact heat transfer effectiveness.

On the other hand, with the decrease in the droplets average size from 19.2 μm to 7.6 μm at the 0.5 atm case, and for the same water and air mass flow rate, the spray has a higher droplet number density but a lower droplet momentum. As a result, the droplets would hit at the jet impingement point with lower impacting Weber numbers. Therefore, the cooling will be less at the center but more uniform and spreads out to a larger area (as seen in Figure 6.19). The decrease in the droplet Weber number at the jet impingement point would cause a decrease in the heat transfer effectiveness. This can be seen by comparing Figure 6.17 with Figure 6.13. Figure

20 shows the effect of increasing the water mass flow rate (while keeping the air mass flow rate the same) on the mist heat transfer coefficient for different ambient pressures. The model predicts linear dependency because it does not account for the flooding that occurs on the surface. Also seen is that higher pressures lead to higher mist heat transfer in the spray, thus causing an enhancement in the cooling process.

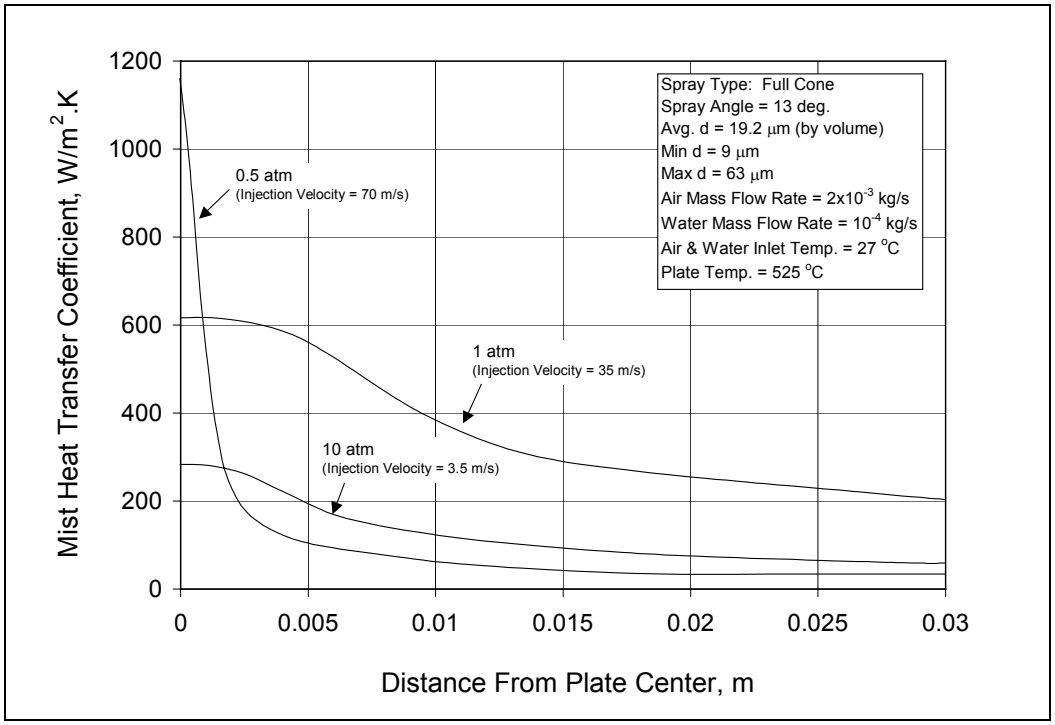

Figure 6.13 Mist spray heat transfer coefficient profile versus ambient pressure

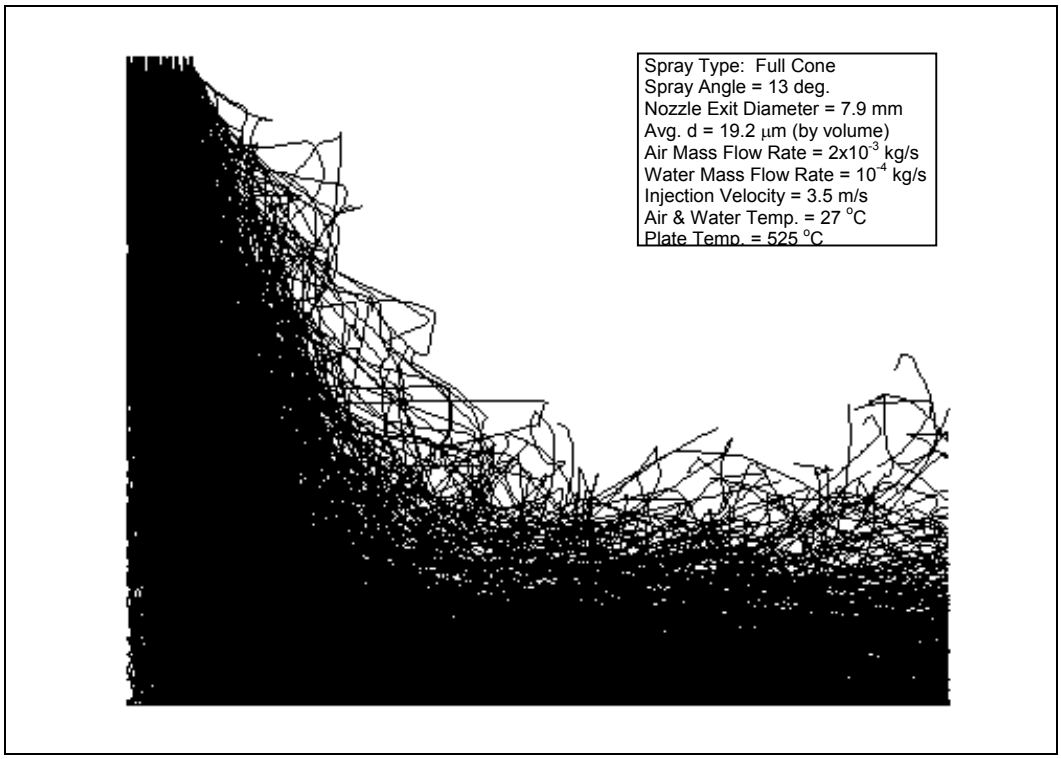

Figure 6.14 Mist spray pattern at 10 atm ambient pressure (Avg. d = 19.2 μm by volume)

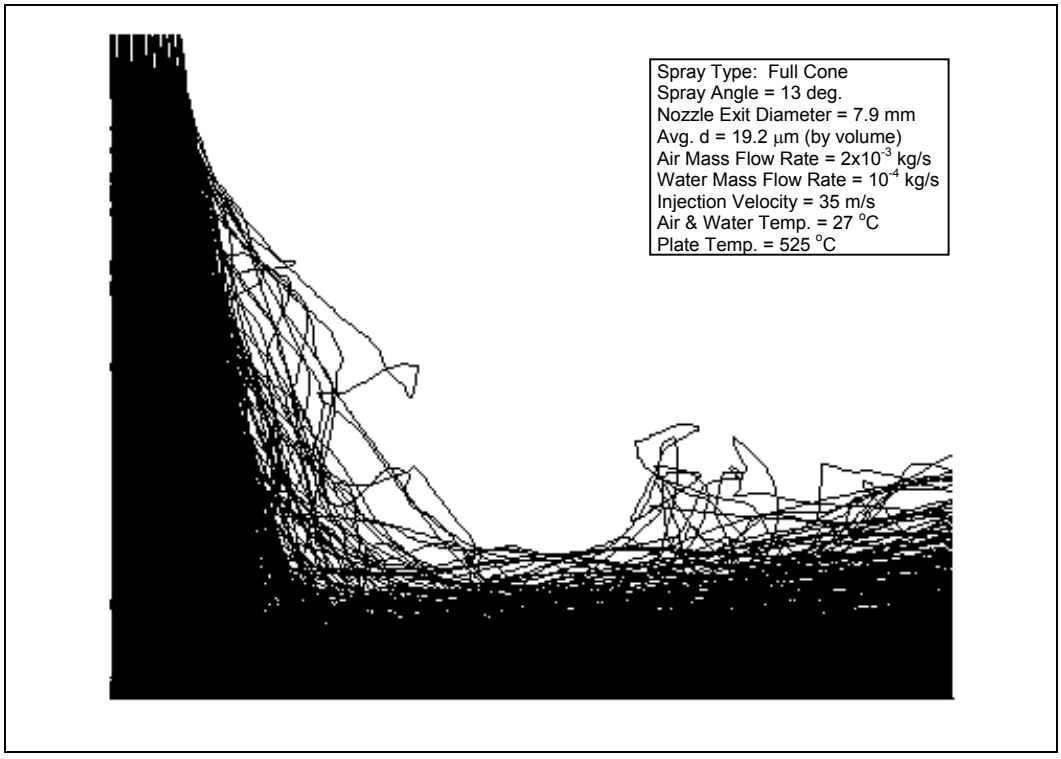

Figure 6.15 Mist spray pattern at 1 atm ambient pressure (Avg. d = 19.2 μm by volume)

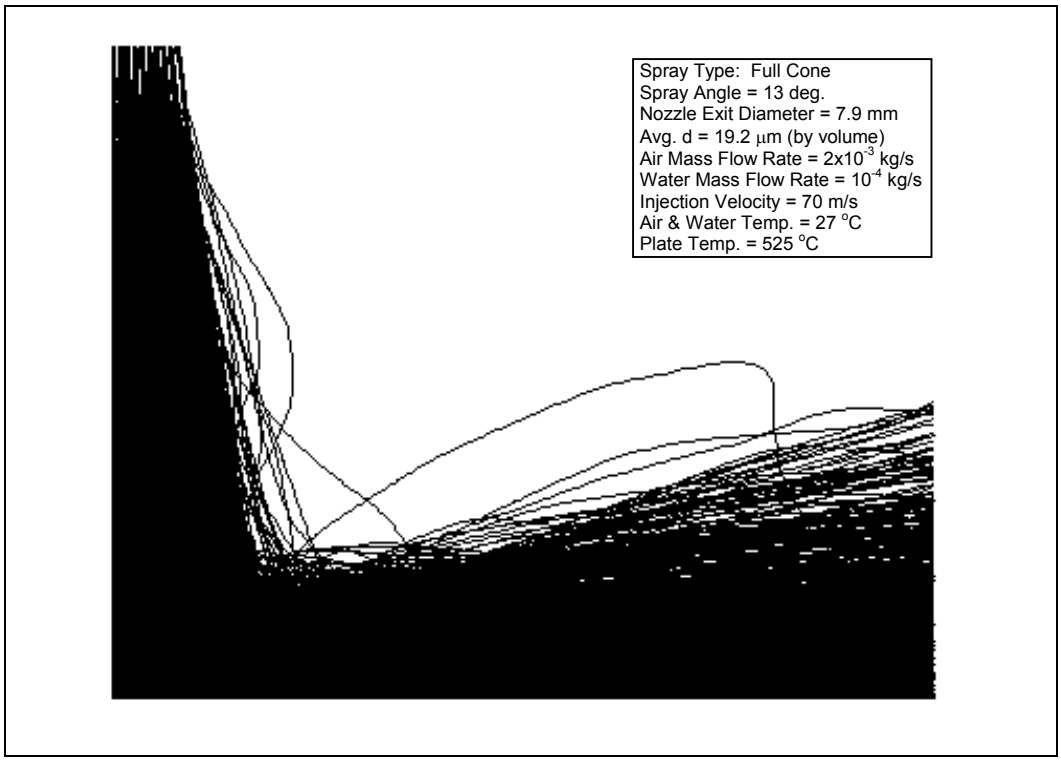

Figure 6.16 Mist spray pattern at 0.5 atm ambient pressure (Avg. d = 19.2 μm by volume)

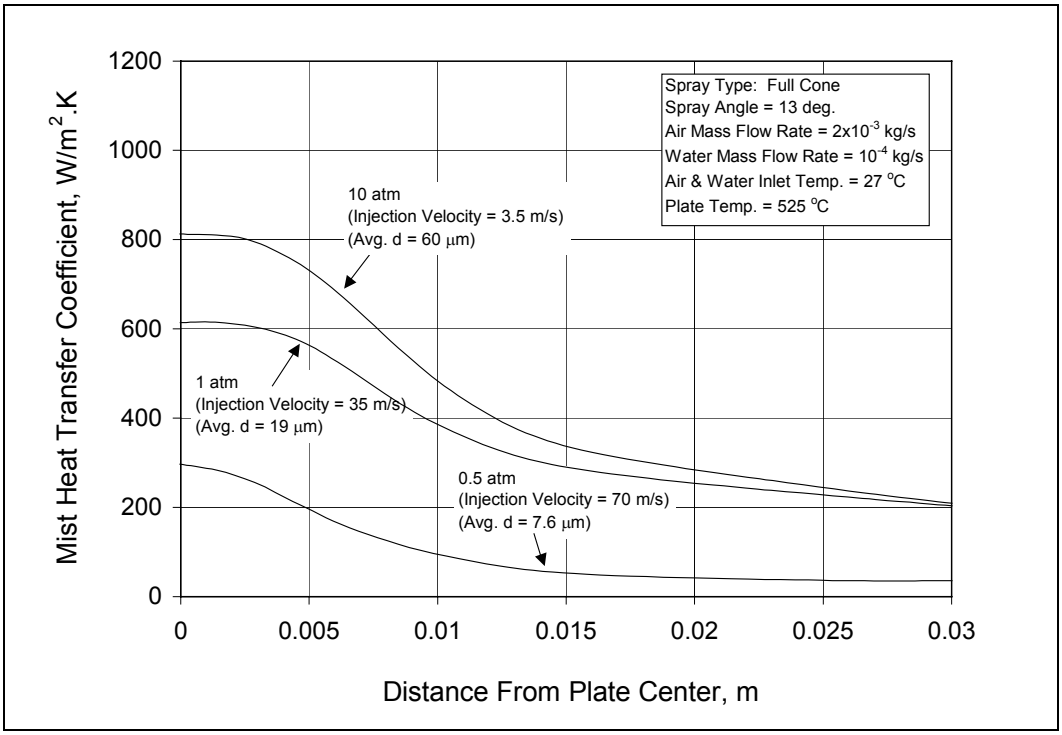

Figure 6.17 Mist spray heat transfer coefficient versus ambient pressure using larger drop size for high pressure and smaller drop size for low pressure

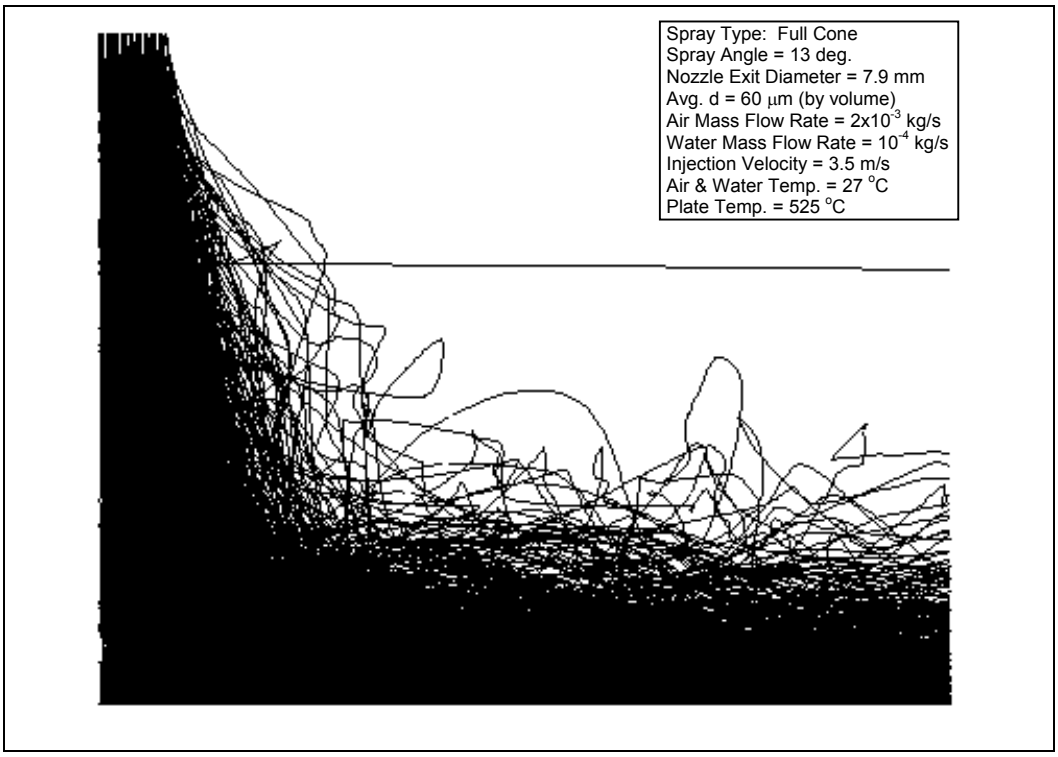

Figure 6.18 Mist spray pattern at 10 atm ambient pressure (Avg. d = 60 μm by volume)

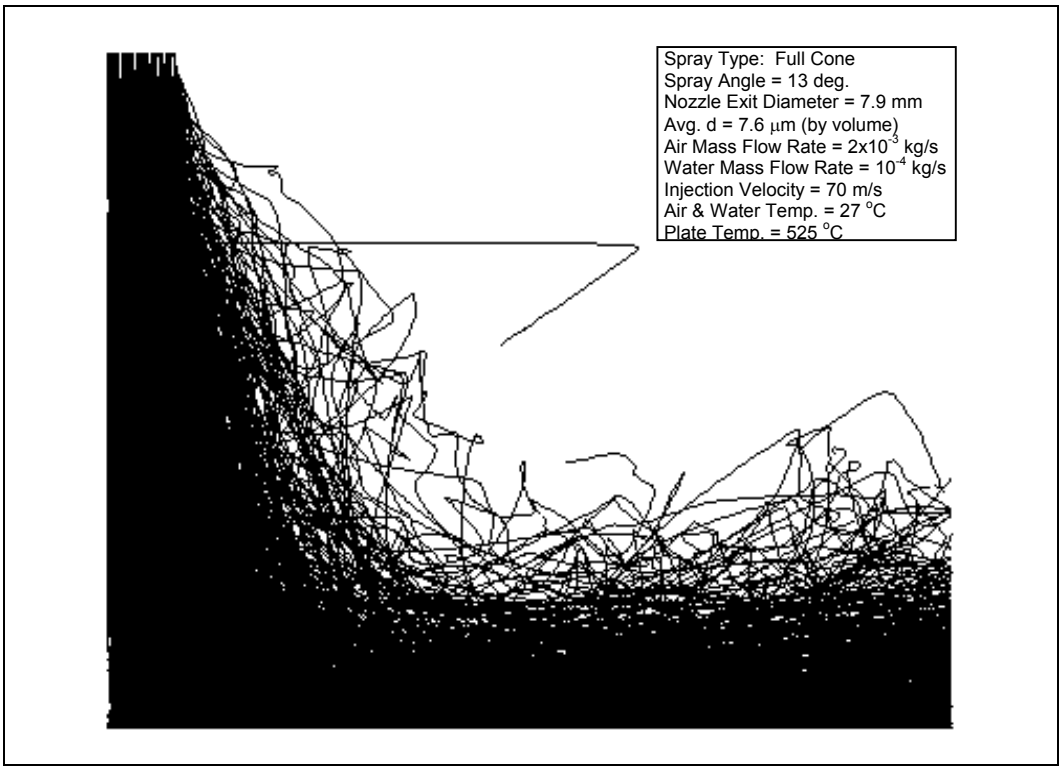

Figure 6.19 Mist spray pattern at 0.5 atm ambient pressure (Avg. d = 7.6 μm by volume)

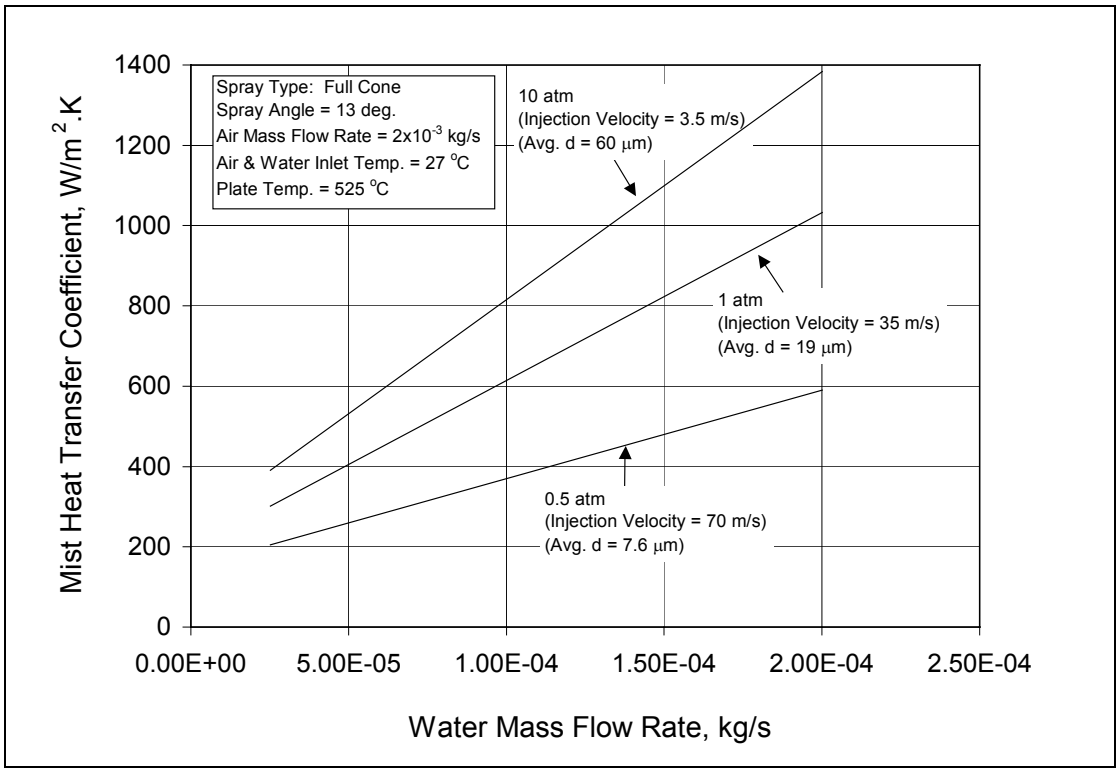

Figure 6.20 Effect of liquid loading on the mist spray heat transfer coefficient for different ambient pressures

6.5 Spraying in Engine-Like Conditions

For the last decade or so, a variety of experiments have been conducted on the fuel spray impingement for diesel engine applications. Those experiments provided a great deal of detail on the structure of the impinging sprays, and on the interaction of the spray with the wall at high operating pressures. Sakane et al. [26], Mirza [27], Katsura et al. [28], Fujimoto et al. [63], Senda et al. [29], Saito et al. [30], and Guerrasi and Champoussin [31] are among the researchers who have been studying diesel spray-wall impingement. In the majority of those tests, the experimental setup and the spray operating conditions were similar. A single nozzle with a diameter ranging between 0.2 and 0.3 mm was often used. The nozzle to wall distance ranged between 24 and 50 mm, with the chamber being pressurized between 1 atm and 30 atm. The

spray average diameter ranged between 19 and 40 μm. The average velocity of the droplets in the flow ranged from 30 to 40 m/s. The only disadvantage in all those experiments is that they were conducted with the wall temperature being at room temperature (~ 20 ^{o}C). Nevertheless, the information those experiments provide such as the sensitivity of the spray height to the variation in the operating pressure is very valuable. Figure 6.21 is a summary of compiled data from diesel spray research showing the variation in the spray height as function of the ambient pressure. It is shown that as the ambient pressure increases, the impinging spray height increases, but only slightly (about 15% increase in the spray height as the pressure increases from 1 to 30 atm). One possible explanation for this is that as the pressure increases, the increase in the drag force against the droplets results in a reduction in the velocity of the impinging droplets, making more droplets rebound from the wall. This happens because the droplets retain more of the momentum they had before the impact, and therefore rebound with a slightly higher velocity that leads to a slight increase in the rebound height. Using the above engine-like spray settings and operating conditions, simulations were conducted using our model. Figures 6.22 through 6.24 show the non-evaporative spray-wall impingement at 0.1, 1, and 30 atm ambient pressures for a nozzle dispersing multi-size (non-uniform) droplets with an average droplet diameter of 30 μm by volume (min d = 14.4 μm, max d = 100.8 μm). The sub-atmospheric pressure of 0.1 atm was simulated just for a comparison purpose. For the same initial spray velocity of 35 m/s, the droplets were seen to reflect with a slightly higher velocity (11.1 m/s compared to 8.19 m/s) as the pressure increases from 1 atm to 30 atm resulting in a slight increase in spray height. More droplets are also seen to drift along side the wall at 30 atm. For the engine-like conditions at 30 atm, the simulation was in agreement with what was observed experimentally by the researchers mentioned earlier regarding to the reflected spray height. On

the other hand, in sub-atmospheric conditions (0.1 atm), the drag force acting on the droplets is lower due to the lower ambient density. This causes the droplets to impinge ballistically; thus, resulting in much higher rebound as shown in Figure 6.22. The droplet rebound velocity was about 5.98 m/s compared to 8.19 m/s at 1 atm.

Figure 6.25 shows the evaporative spray-wall impingement at 30 atm on a surface heated to 300 ^{o}C. With a heated surface, the droplet rebound velocity is seen to decrease to 9.73 m/s compared to 11.1 m/s for the non-heated surface. This is because for the operating flow conditions, about 12% of the spray mass evaporates. With less mass, the droplets rebound with less momentum, and therefore, lower rebound velocities and rebound heights. A comparison between the evaporative and the non-evaporative cases shows a slight increase in the droplet drift for the evaporative case which is attributed to the reduced droplets size.

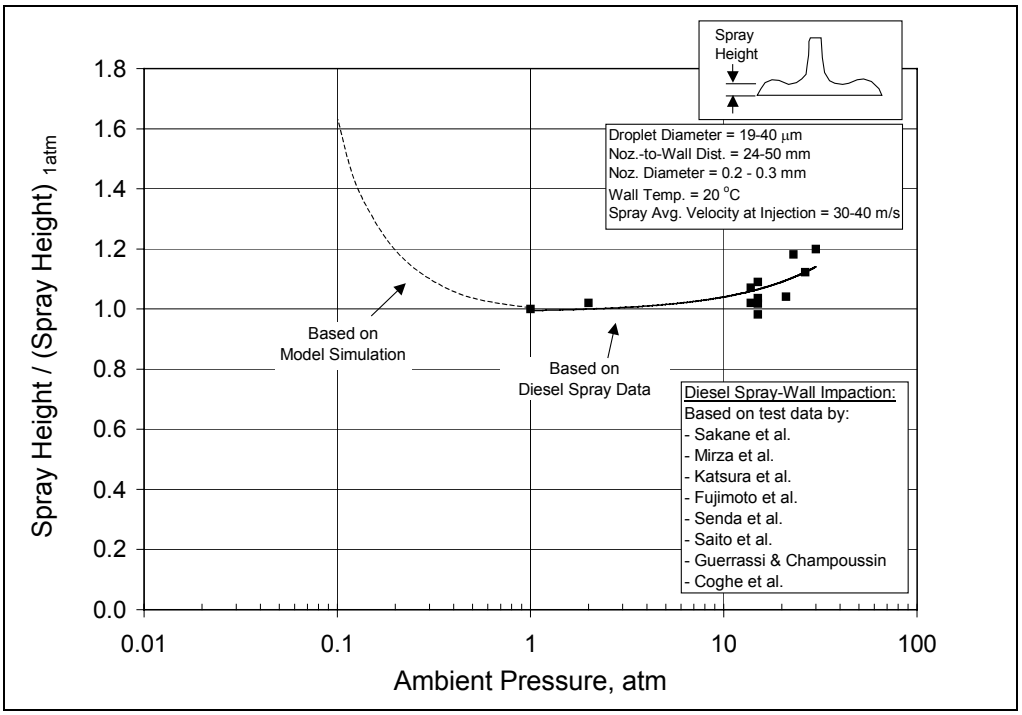

Figure 6.21 Spray height versus ambient pressure in engine-like conditions

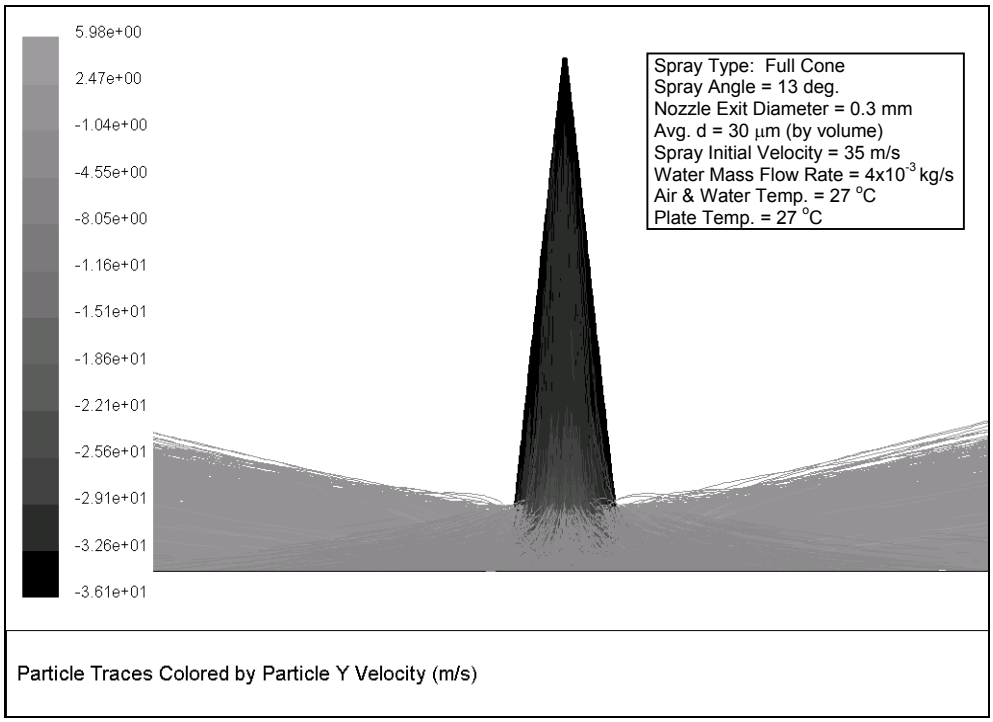

Figure 6.22 Non-evaporative mist spray pattern at 0.1 atm

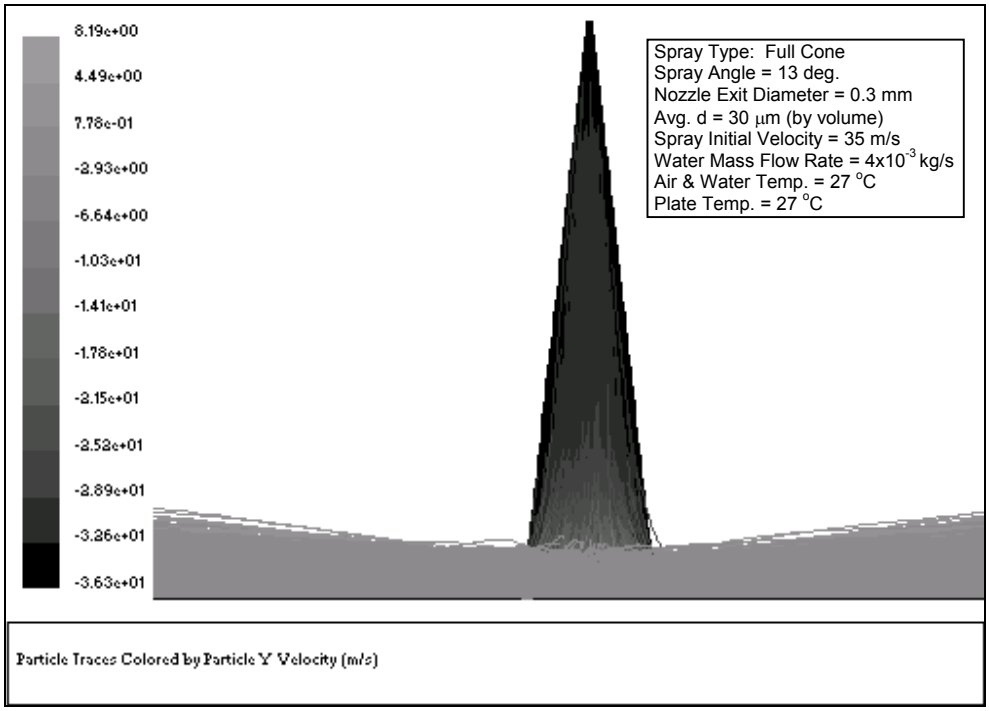

Figure 6.23 Non-evaporative mist spray pattern at 1 atm

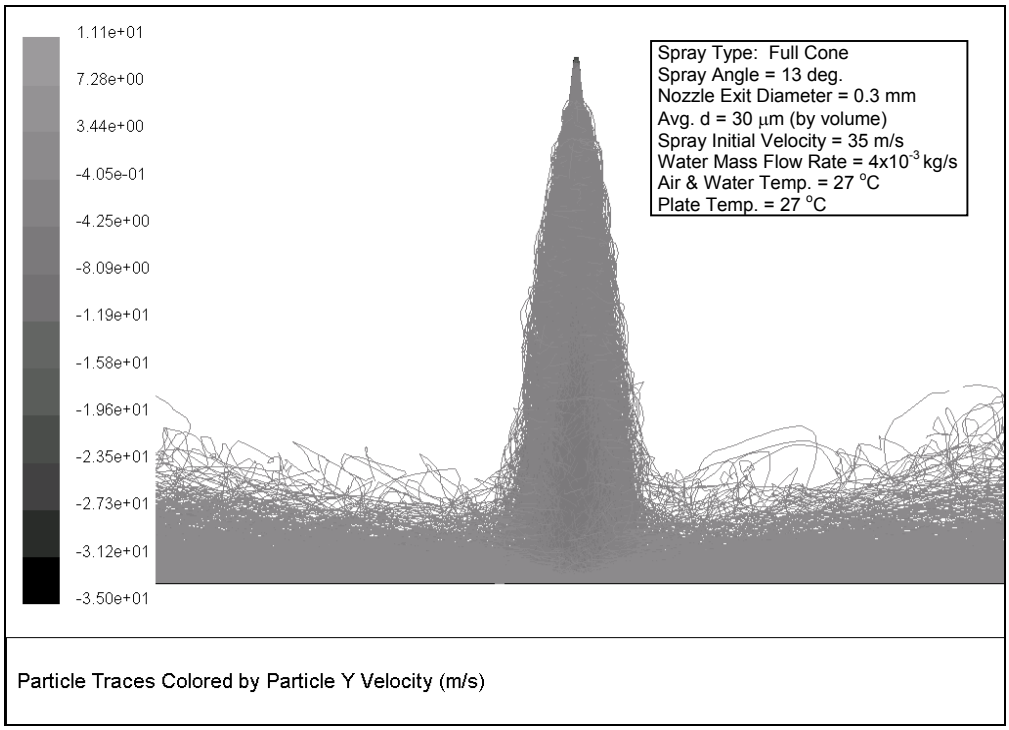

Figure 6.24 Non-evaporative mist spray pattern at 30 atm (engine-like conditions)

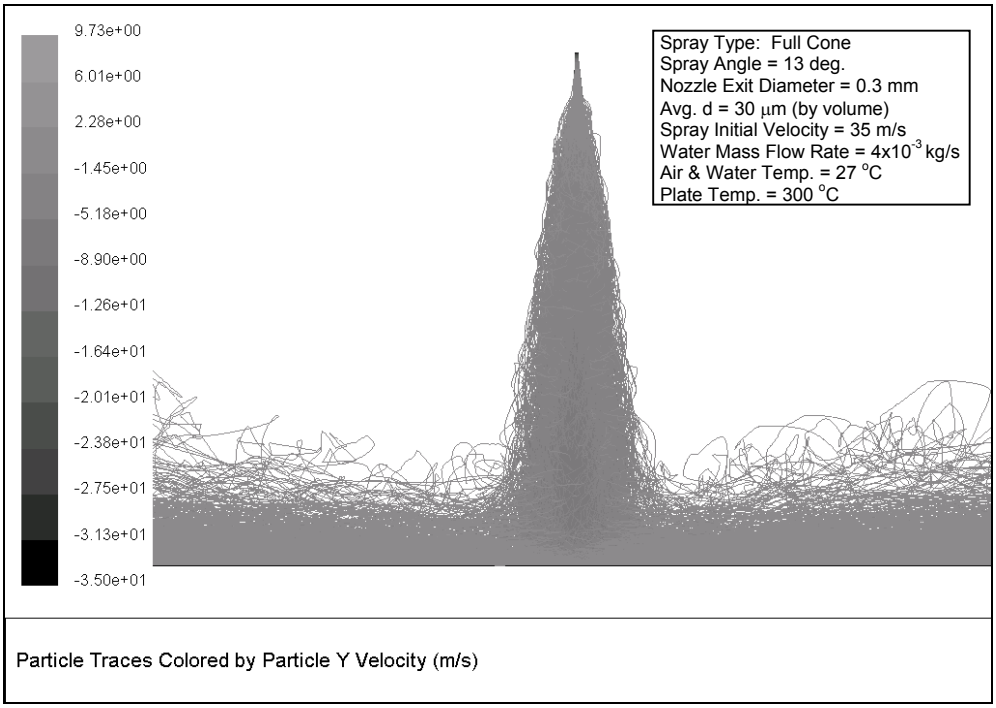

Figure 6.25 Evaporative mist spray pattern at 30 atm (engine-like conditions)

7.0 CONCLUSIONS

7.1 Major Contributions

A numerical model based on the Lagrangian tracking of droplets was developed for the purpose of studying the mist cooling on metallic surfaces heated in the temperature range between nucleate and film boiling. The model simulates the droplet-wall interaction, and the droplet contact heat transfer as function of the impinging droplet Weber number. The model was tested at atmospheric pressure using experimental data for nozzles that dispense a spectrum of non-uniform droplets. Favorable comparison with the experimental data was demonstrated.

The model's capability was also extended to simulate high and sub-atmospheric pressure conditions by properly accounting for the droplet-wall impaction and the air-mist heat transfer mechanism as function of the ambient pressure. With the lack of experimental data performed using full sprays, the model was tested against available experiments that have been conducted using single stream droplet impactions at various ambient pressures. The model's simulation and the experimental data also compared well.

The attempt of numerically modeling the droplet-wall impaction dynamics and contact heat transfer has not been addressed before. This is the first time a model is developed to simulate the dynamic behavior of the droplets with multiple droplet-wall collisions, and also the first time a model considers the effect of droplet impinging Weber number on the droplet contact heat transfer effectiveness with a realistic comparison to experimental results.

Spray simulation conducted for a wide range of pressures reveals the following primary key issues regarding to the droplet dynamics, heat transfer and vaporization:

1) Droplet Dynamics. At higher pressures, the larger the droplet size the better is the droplet-wall impaction. With the increase in the drag force (due to the increase in the ambient density), droplet-drifting behavior increases. Therefore, at higher pressures larger droplets are able to hit the surface and spread better at impaction. On the other hand, for sub-atmospheric pressures, larger droplets have a detrimental effect due to their ballistic and localized impaction near the stagnation point. This is caused by the much reduced air resistance due to the lower ambient density. For all ranges of pressure, a spray dispersing a spectrum of non-uniform droplets always have the larger droplets impinge closer to the center (due to the higher momentum), while the smaller droplets impinge further away due to the lower momentum associated with smaller droplets.
2) Droplet Heat Transfer. At higher pressures, the Leidenfrost point shifts to a higher temperature. This leads to an increase in the wetting capability of the droplets at impaction, and therefore, to a higher droplet contact heat transfer effectiveness.
3) Droplet Vaporization. At high ambient pressures, more vapor is generated at each droplet impaction on the surface. This is due to the much-reduced latent heat of vaporization at higher pressures. The result is an increase in the droplet contact heat transfer effectiveness.

Simulations also reveal the following secondary issues:

- The cooling profile depends on the size of the dispersed droplets in the air-mist spray. Sprays with mono-size droplets can result in a non-uniform cooling pattern, and fine

droplet sizes can hit further away from the jet impingement point due to the air drift. On the other hand, sprays dispersing a wide spectrum of droplet sizes will contact the wall at random locations; thus resulting in a much uniform cooling profile.

- The droplet cooling effectiveness is a strong function of the ambient pressure, and increases quite rapidly with the pressure at lower pressures. This effect decreases as the ambient pressure approaches the critical peak at which maximum droplet cooling can be achieved.
- For the same amount of liquid loading, and for low-pressure applications, larger droplets result in a more non-uniform cooling profile than smaller droplets. This is because the ballistic impaction of larger droplets causes a sharp increase in the heat transfer near the stagnation point. On the other hand, for high-pressure applications, larger droplets result in better heat transfer profile than smaller droplets, since larger droplets are more able to impact the wall, and drift less.
- The profile of the thermal boundary layer depends on the amount of water vapor generated from the droplet evaporation at the wall, and also on the ambient pressure. The evaporation of larger droplets causes a violent eruption in the thermal boundary layer. With larger droplets, the higher the thermal plume is ejected away from the wall. Also, with the increase in ambient pressure, the ejected thermal plume diffuses over a wider region but remains closer to the wall.

7.2 Suggestions for Further Research

The following topics are suggested for further research:

- Investigate the spray-wall impaction using diesel fuel. This is applicable to the spray direct injection in diesel engines. Diesel fuel has distinct thermo-physical properties than water. Moreover, the wall temperature in the engine cylinder is much lower than that of the strip in the strip cooling applications. Therefore, the bouncing behavior of diesel droplets on the cylinder wall may be different.
- Investigate the diesel-spray heat transfer effectiveness based on single droplet multiple impactions using the current model with the proper modification done to the model. Empirical correlations for the droplet contact heat transfer similar to those generated for water droplets, can also be developed for diesel fuel as function of the cylinder compression pressure and wall temperature. The model can then be validated against experiments that have already been conducted and published in the diesel-spray research.
- The current research of this dissertation can also be expanded to simulate the high-pressure air-mist cooling through gas turbine airfoils. This shall provide more insight into the optimal flow conditions, droplet size distribution, and liquid loading for best heat transfer enhancement of the gas turbine airfoils. The predictions by this model can be compared with the results of well-instrumented high-pressure air-mist experiments conducted on the gas turbine airfoils.

APPENDIX A

APPENDIX A

CALCULATION OF THE DROPLET VAPOR MASS

The droplet vapor mass released at the heated wall during impaction can be calculated from the droplet enthalpy change (difference between the droplet enthalpy before and after impact). In order to calculate for the vapor mass, we need to know the amount of heat transferred during:

1) Complete droplet evaporation, and
2) Partial droplet evaporation.

1. Complete Droplet Evaporation ($\varepsilon = 1$)

This is the case where the droplet trajectory is terminated at the surface and the droplet completely evaporates. The undergoing process is as follows. An impinging liquid droplet of temperature T_d would transform into vapor when its temperature reaches saturation (T_{sat}). The vapor, which is in the vicinity of the wall, would now superheat to the wall temperature (T_w). The figure below illustrates the enthalpy change of the droplet during this process.

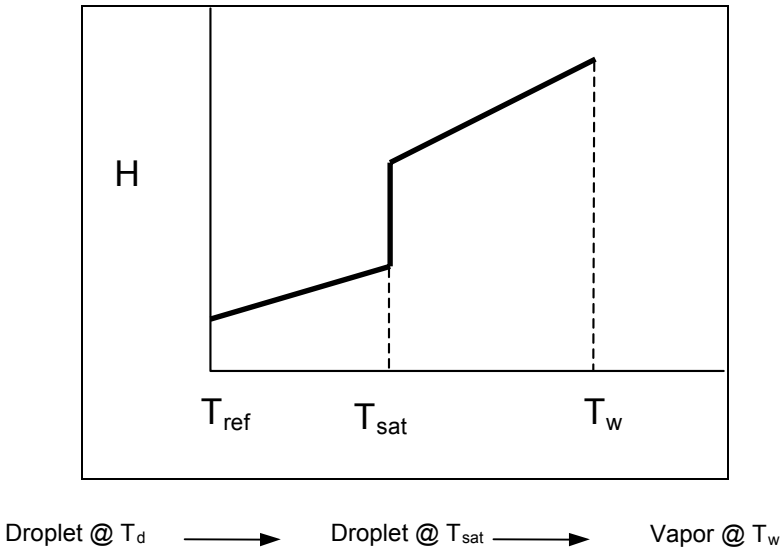

Figure A-1 Droplet enthalpy change before and after impact
(Complete droplet evaporation)

a) Droplet Enthalpy before Impact:

Let T_{ref} be the reference temperature for the calculation of the enthalpy change of the droplet. The droplet enthalpy before impact is:

$$H_1 = m_d \int_{T_{ref}}^{T_d} c_{p,d} dT = m_d c_{p,d} T_d \qquad (T_d < T_{sat}) \quad \text{(A-1)}$$

b) Droplet Enthalpy after Impact:

The droplet enthalpy after impact is:

$$\begin{aligned} H_2 &= m_v \left\{ \int_{T_{ref}}^{T_d} c_{p,d} dT + \int_{T_d}^{T_{sat}} c_{p,d} dT + \Delta h_{fg} + \int_{T_{sat}}^{T_w} c_{p,v} dT \right\} \\ &= m_v \left\{ c_{p,d} T_d + c_{p,d} \left(T_{sat} - T_d \right) + \Delta h_{fg} + c_{p,v} \left(T_w - T_{sat} \right) \right\} \end{aligned} \qquad \text{(A-2)}$$

c) Droplet Enthalpy Change:

The droplet enthalpy change is calculated by subtracting the droplet enthalpy after impact from the droplet enthalpy before impact. The change in enthalpy is the actual amount of heat transferred during this process (complete droplet evaporation).

$$\begin{aligned} q_{100\%} &= H_2 - H_1 \\ &= m_d \left\{ c_{p,d}\left(T_{sat} - T_d\right) + \Delta h_{fg} + c_{p,v}\left(T_w - T_{sat}\right) \right\} \end{aligned} \tag{A-3}$$

2. Partial Droplet Evaporation ($\varepsilon < 1$)

For the case of partial droplet evaporation, the process is slightly different. A fraction of the impinging droplet mass (m_d) will be converted to vapor (m_v) which will be heated to the saturation temperature (T_{sat}) and subsequently the vapor will superheat to the wall temperature (T_w). The remaining mass of the droplet ($m_d - m_v$) will remain as liquid at temperature T_{sat}. The following figure illustrates this process.

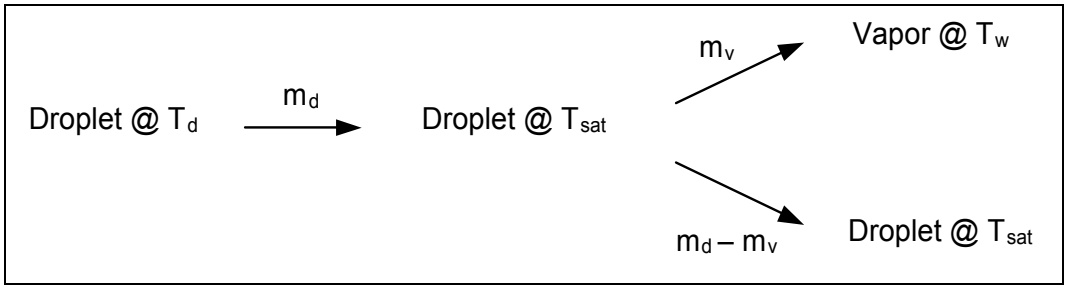

Figure A-2 Droplet enthalpy change before and after impact (Partial droplet evaporation)

a) Droplet Enthalpy before Impact:

The droplet enthalpy before impact is similar to that calculated in section 1.

$$H_1 = m_d \int_{T_{ref}}^{T_d} c_{p,d} dT = m_d c_{p,d} T_d \qquad (T_d < T_{sat}) \qquad \text{(A-4)}$$

b) Droplet Enthalpy after Impact:

The droplet enthalpy after impact has two contributions: vapor part, and a liquid part.

Vapor Part

$$\begin{aligned} H_2 &= m_v \left\{ \int_{T_{ref}}^{T_d} c_{p,d} dT + \int_{T_d}^{T_{sat}} c_{p,d} dT + \Delta h_{fg} + \int_{T_{sat}}^{T_w} c_{p,v} dT \right\} \\ &= m_v \left\{ c_{p,d} T_d + c_{p,d} (T_{sat} - T_d) + \Delta h_{fg} + c_{p,v} (T_w - T_{sat}) \right\} \end{aligned} \qquad \text{(A-5)}$$

Liquid Part

$$\begin{aligned} H_3 &= (m_d - m_v) \left\{ \int_{T_{ref}}^{T_d} c_{p,d} dT + \int_{T_d}^{T_{sat}} c_{p,d} dT \right\} \\ &= (m_d - m_v) \left\{ c_{p,d} T_d + c_{p,d} (T_{sat} - T_d) \right\} \end{aligned} \qquad \text{(A-6)}$$

c) Droplet Enthalpy Change:

The amount of heat transferred for partial droplet evaporation is calculated by subtracting the droplet enthalpy before impact from the droplet enthalpy after impact as follows:

$$\begin{aligned} q_{partial} &= H_3 + H_2 - H_1 \\ &= (m_d - m_v) \left\{ c_{p,d} T_d + c_{p,d} (T_{sat} - T_d) \right\} \\ &\quad + m_v \left\{ c_{p,d} T_d + c_{p,d} (T_{sat} - T_d) + \Delta h_{fg} + c_{p,v} (T_w - T_{sat}) \right\} - m_d c_{p,d} T_d \\ &= m_d c_{p,d} (T_{sat} - T_d) + m_v \Delta h_{fg} + m_v c_{p,v} (T_w - T_{sat}) \end{aligned} \qquad \text{(A-7)}$$

d) Calculation of the Vapor Mass:

The portion of the droplet mass that is released as vapor during impact is calculated by considering the heat that is released during partial evaporation to be a fraction of the maximum possible heat can be released when complete droplet evaporation occurs. We refer to this fractional factor by the droplet heat transfer effectiveness, ε.

$$q_{partial} = \varepsilon \; q_{100\%}$$

$$\Rightarrow m_v = \frac{(\varepsilon - 1) m_d c_{p,d} (T_{sat} - T_d) + \varepsilon m_d \Delta h_{fg} + \varepsilon m_d c_{p,v} (T_w - T_{sat})}{c_{p,v} (T_w - T_{sat}) + \Delta h_{fg}} \qquad \text{(A-8)}$$

APPENDIX B

APPENDIX B

DROPLET CONTACT HEAT TRANSFER EFFECTIVENESS

The droplet contact heat transfer effectiveness is calculated as function of the ambient pressure as follows. For impinging normal Weber numbers that are between the upper and lower bounds, the heat transfer effectiveness is interpolated.

0.1 atm Ambient Pressure

@ $We_n \leq 19$,

$$\varepsilon = 0.075 + 0.0555\cos\left(\frac{\pi}{445.7}[(T_w - T_d) - 74.3]\right) \quad \text{(B-1)}$$

@ $We_n = 483$,

$$\varepsilon = 0.285 + 0.175\cos\left(\frac{\pi}{445.7}[(T_w - T_d) - 74.3]\right) \quad \text{(B-2)}$$

0.2 atm Ambient Pressure

@ $We_n \leq 19$,

$$\varepsilon = 0.095 + 0.075\cos\left(\frac{\pi}{449}[(T_w - T_d) - 89.6]\right) \quad \text{(B-3)}$$

@ $We_n = 483$,

$$\varepsilon = 0.355 + 0.245\cos\left(\frac{\pi}{449}[(T_w - T_d) - 89.6]\right) \quad \text{(B-4)}$$

0.5 atm Ambient Pressure

@ $We_n \leq 19$,

$$\varepsilon = 0.115 + 0.095\cos\left(\frac{\pi}{463.6}[(T_w - T_d) - 109.7]\right) \quad \text{(B-5)}$$

@ $We_n = 483$,

$$\varepsilon = 0.45 + 0.32\cos\left(\frac{\pi}{463.6}[(T_w - T_d) - 109.7]\right) \quad \text{(B-6)}$$

1 atm Ambient Pressure

@ $We_n \leq 19$,

$$\varepsilon = 0.113 + 0.138\cos\left(\frac{\pi}{470}[(T_w - T_d) - 130]\right) \quad \text{(B-7)}$$

@ $We_n = 483$,

$$\varepsilon = 0.535 + 0.355\cos\left(\frac{\pi}{470}[(T_w - T_d) - 130]\right) \quad \text{(B-8)}$$

2 atm Ambient Pressure

@ $We_n \leq 19$,

$$\varepsilon = 0.155 + 0.115\cos\left(\frac{\pi}{495.6}[(T_w - T_d) - 151.7]\right) \quad \text{(B-9)}$$

@ $We_n = 483$,

$$\varepsilon = 0.615 + 0.345\cos\left(\frac{\pi}{495.6}[(T_w - T_d) - 151.7]\right) \quad \text{(B-10)}$$

5 atm Ambient Pressure

@ $We_n \leq 19$,

$$\varepsilon = 0.17 + 0.12\cos\left(\frac{\pi}{514.7}[(T_w - T_d) - 195.9]\right) \quad \text{(B-11)}$$

@ $We_n = 483$,

$$\varepsilon = 0.685 + 0.315\cos\left(\frac{\pi}{514.7}[(T_w - T_d) - 195.9]\right) \quad \text{(B-12)}$$

10 atm Ambient Pressure

@ $We_n \leq 19$,

$$\varepsilon = 0.18 + 0.12\cos\left(\frac{\pi}{523.8}[(T_w - T_d) - 242.2]\right) \quad \text{(B-13)}$$

@ $We_n = 483$,

$$\varepsilon = 0.715 + 0.285\cos\left(\frac{\pi}{523.8}[(T_w - T_d) - 242.2]\right) \quad \text{(B-14)}$$

30 atm Ambient Pressure

@ $We_n \leq 19$,

$$\varepsilon = 0.18 + 0.11\cos\left(\frac{\pi}{522.2}[(T_w - T_d) - 345.1]\right) \quad \text{(B-15)}$$

@ $We_n = 483$,

$$\varepsilon = 0.74 + 0.26\cos\left(\frac{\pi}{522.2}[(T_w - T_d) - 345.1]\right) \quad \text{(B-16)}$$

50 atm Ambient Pressure

@ $We_n \leq 19$,

$$\varepsilon = 0.17 + 0.1\cos\left(\frac{\pi}{512.3}[(T_w - T_d) - 407.6]\right) \quad \text{(B-17)}$$

@ $We_n = 483$,

$$\varepsilon = 0.725 + 0.255\cos\left(\frac{\pi}{512.3}[(T_w - T_d) - 407.6]\right) \qquad \text{(B-18)}$$

APPENDIX C

APPENDIX C

BASIC PROGRAM STRUCTURE

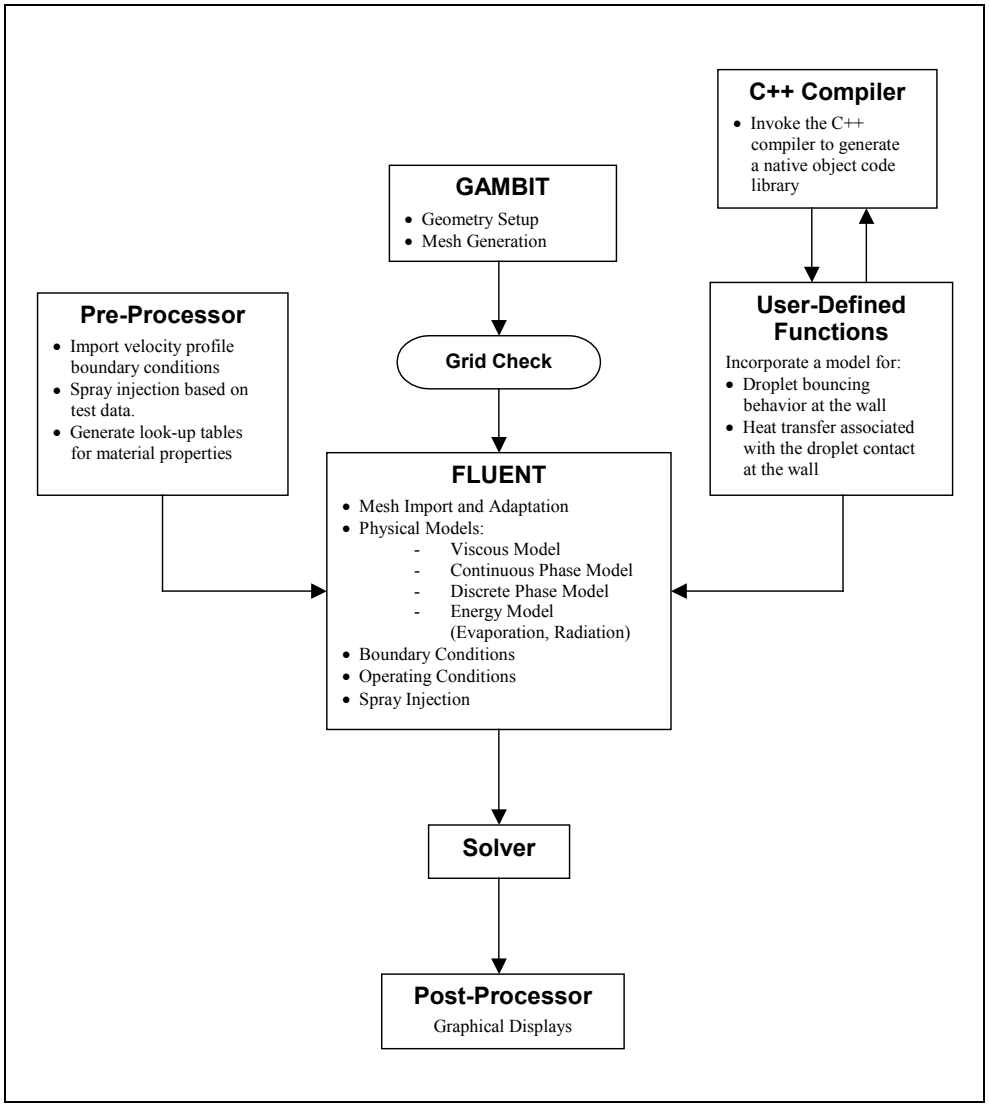

Figure C-1 Basic program structure

BIBLIOGRAPHY

BIBLIOGRAPHY

[1] Evans, J. F., et al., "Numerical Modelling of Hot Strip Mill Runout Table Cooling", Iron and Steel Engineer, pp. 50-55, 1993.

[2] Ishida, R., et al., "Basic Characteristics of Pipe Nozzle Cooling with Retaining Water on Plate", ISIJ International, v 29, n 4, pp. 339-344, 1989.

[3] Hadrian, U. T., "The Cooling Efficiency of Laminar-Orthogonal Water (LOW) Curtains in Hot Strip Mills", Metallurgical Plant and Technology, v 6, pp. 44-49, 1984.

[4] Auzinger, D., et al., "Process Optimization for Laminar Cooling", MPT International, v 5, pp. 68-75, 1996.

[5] Nirmalan, N. V., et al., "An Experimental Study of Turbine Vane Heat Transfer with Water-Air Cooling", J. of Turbomachinery, v 120, no. 1, pp. 50-62, 1998.

[6] Wang, T., et al., "Mist/Steam Heat Transfer with Jet Impingement onto a Concave Surface", Proceedings of ASME Turbo Expo 2002, Amsterdam, The Netherlands, June 3-6, 2002.

[7] Bohn, D., et al., "Experimental and Numerical Investigation of a Steam-Cooled Vane", Proceedings of ASME Turbo Expo 2002, Amsterdam, The Netherlands, June 3-6, 2002.

[8] Guo, T., et al., "Mist/Steam Cooling in a 180^{o} Tube Bend", ASME Journal of Heat Transfer, vol. 122, pp. 749-756, 2001.

[9] Yao, S. C., et al., "Impact Spray Boiling for Thermal Control of Electronic Systems", ASME HTD-Heat Transfer in Electronics, v 111, pp. 129-133, 1989.

[10] Yao, S. C., et al., "MEMS Enabled Micro Spray Cooling System for Thermal Control of Electronic Chips", ASME, IMECE, 2001.

[11] Mudawar, I., and Estes, K. A., "Comparison of Two-Phase Electronic Cooling Using Free Jets and Sprays", Advances in Electronic Packaging, Proceedings of International Electronic Packaging Conference, v 2, pp. 975-987, 1995.

[12] Industrial Spray Products by Spraying Systems Company, Catalog no. 55.

[13] Pedersen, C. O., "An Experimental Study of the Dynamic Behavior and Heat Transfer Characteristics of Water Droplets Impinging Upon a Heated Surface", International Journal of Heat and Mass Transfer, v 13, 1970.

[14] Kendall, G. E., and Rohsenow, W. M., "Heat Transfer to Impacting Drops and Post Critical Heat Flux Dispersed Flow", Technical Report No. 85694-100, Heat Transfer Laboratory, Massachusetts Institute of Technology, 1978.

[15] Senda, J., et al., "The Heat Transfer Characteristics of a Small Droplet Impinging upon a Hot Surface", JSME International Journal, Series II, v 31, n 1, 1988.

[16] McGinnis, F. K. III, and Holman, J. P., "Individual Droplet Heat Transfer Rates for Splattering on Hot Surfaces", International Journal of Heat and Mass Transfer, v 12, 1969.

[17] Sozbir, N., and Yao, S. C., "Experimental Investigation of Water Mist Cooling for Glass Tempering", ASME-IMECE Conference, 2002.

[18] Chang, Y. W., and Yao, S. C., "Studies of Water Mist Cooling on Heated Metal Surfaces", Proceedings of NHTC'00, 34th National Heat Transfer Conference, 2000.

[19] Ortiz, L., and Gonzalez, J. E., "Experiments on Steady-State High Heat Fluxes using Spray Cooling", Experimental heat Transfer, v 12, n 3, pp. 215-233, 1999.

[20] Ohkubo, H., and Nishio, S., "Study on Transient Characteristics of Mist-Cooling Heat Transfer from a Horizontal Upward-Facing Surface", Heat Transfer – Japanese Research, v 21, n 6, pp. 543-555, 1992.

[21] Pais, M. R., et al., "Surface Roughness and Its Effects on the Heat Transfer Mechanism in Spray Cooling", Journal of Heat Transfer, v 114, pp. 211-219, 1992.

[22] Halvorson, P. J., "On the Heat Transfer Characteristics of Spray Cooling", Ph.D. Thesis, Georgia Institute of Technology, 1994.

[23] Testa, P., and Nicotra, L., "Influence of Pressure on the Leidenfrost Temperature and on Extracted Heat Fluxes in the Transient Mode and Low Pressure", Journal of Heat Transfer, v 108, pp. 916-921, 1986.

[24] Emmerson, G. S., and Snoek, C. W., "The Effect of Pressure on the Leidenfrost Point of Discrete Drops of Water and Freon on a Brass Surface", Journal of Heat and Mass Transfer, v 21, pp. 1081-1086, 1978.

[25] Emmerson, G. S., "The Effect of Pressure and Surface Material on the Leidenfrost Point of Discrete Drops of Water", Journal of Heat and Mass Transfer, v 18, pp. 381-386, 1975.

[26] Sakane, A., et al., "Behaviour of Diesel Spray Impinging on a Wall", Journal of Mechanical Engineering Society of Japan, v 54, 1988.

[27] Mirza, R., "Studies of Diesel Spray Interacting with Cross-Flow and Solid Boundaries", Ph.D. Thesis, University of Manchester, Manchester, UK, 1991.

[28] Katsura, N., et al., "Characteristics of a Diesel Spray Impinging on a Flat Wall", SAE Paper No. 890264, 1989.

[29] Senda, J., et al., "Modeling of Diesel Spray Impingement on a Flat Wall" SAE Paper No. 941894, pp. 1918-1931, 1994.

[30] Saito, A., et al., "Analysis of Impinging Spray Characteristics Under High Pressure Fuel Injection (1st Report, Measurements of Impinging Spray Characteristics)", Transactions of Japan Society of Mechical Engineers B, v 59, 1993.

[31] Guerrassi, N., and Champoussin, J. C., "Experimental Study and Modeling of Diesel Spray/Wall Impingement", SAE Paper No. 960864, pp. 1319-1328, 1996.

[32] Stanton, D. W., and Rutland, C. J., "Multi-Dimensional Modeling of Thin Liquid Films and Spray-Wall Interactions Resulting from Impinging Sprays", International Journal of Heat and Mass Transfer, v 41, pp. 3037-3054, 1998.

[33] Makino, K., and Michiyoshi, I., "The Behavior of a Water Droplet on Heated Surfaces", International Journal of Heat and Mass Transfer, v 27, n 5, pp. 781-791, 1984.

[34] Chandra, S., and Avedisian, C. T., "On the Collision of a Droplet with a Solid Surface", Proceedings of the Royal Society of London A, v 432, pp. 13-41, 1991.

[35] Wachters, L. H. J., and Westerling, N. A. J., "The Heat Transfer from a Hot Wall to Impinging Water Drops in the Spheroidal State", Chemical Engineering Science, v 21, 1966.

[36] Hatta, N. et al., "Experimental Study of Deformation Mechanism of a Water Droplet Impinging on Hot Metallic Surfaces above the Leidenfrost Temperature", Transactions of the ASME, v 119, September 1997.

[37] Hatta, N., et al., "Collision Dynamics of a Water Droplet Impinging on a Rigid Surface above the Leidenfrost Temperature", ISIJ International, v 35, 1995.

[38] Naber, J. D., and Farrell, P. V., "Hydrodynamics of Droplet Impingement on a Heated Surface", SAE Publication no. 930919, March 1993.

[39] Karl, A., et al., "Comparison of New Numerical Results for Droplet Wall Interactions with Experimental Results", The American Society of Mechanical Engineers, 1996 Fluids Engineering Division Conference, v 1, 1996.

[40] Karl, A., and Frohn, A., "Experimental Investigation of Interaction Processes Between Droplets and Hot Walls", American Institute of Physics, pp. 785-796, 2000.

[41] Lee, S. H., and Ryou, H. S., "Development of a New Spray/Wall Interaction Model", International Journal of Multiphase Flow, v 26, pp. 1209-1234, 2000.

[42] Matsumoto, S., and Saito, S., "On the Mechanism of Suspension of Particles in Horizontal Conveying: Monte Carlo Simulation Based on the Irregular Bouncing Model, J. Chem. Engng, Japan 3, pp. 83-92, 1970.

[43] Ford, R. E., and Furmidge, C. G. L., "Impact and Spreading of Spray Drops on Foliar surfaces", Wetting, Soc. Chem. Industry Monograph, v 25, 1967.

[44] Fiedler, R., and Naber, J., Spring Meeting, Central States Section, Combustion Institute, April 30 to May 2, Dearborn, Michigan, 1989.

[45] Akao, F., et al., "Deformation Behaviors of a Liquid Droplet Impinging onto Hot Metal Surface", Transactions of Iron and Steel Institute of Japan, v 20, pp. 737-743, 1980.

[46] Ueda, T., et al., "Heat Transfer Characteristics and Dynamic Behavior of Saturated Droplets Impinging on a Heated Vertical Surface", Bulletin of the JSME, v 22, pp. 724-732, 1979.

[47] Deb, S., and Yao, S. C., "Analysis on Film Boiling Heat Transfer of Impacting Sprays", Int. J. Heat Mass Transfer, v 32, n 11, pp. 2099-2112, 1989.

[48] Yao, S. C., and Cox, T. L., "Investigation into the Use of Large-Drop Sprays for Hot Strip Rolling Mills", 40th MWSP Conf. Proc., ISS, v XXXV, 1998.

[49] Shi, M. H., et al., "Dynamic Behavior and Heat Transfer of a Liquid Droplet Impinging on a Solid Surface", Experimental Thermal and Fluid Science, 1993.

[50] Cichelli, M. T., and Bonilla, C. F., "Heat Transfer to Liquids Boiling Under Pressure", American Institute of Chemical Engineers, v 42, n 2, pp. 755-787, 1946.

[51] Bonilla, C. F., and Perry, C. W., "Heat Transmission to Boiling Binary Liquid Mixtures", Transactions of American Society of Chemical Engineers, v. 37, pp. 685-705, 1941.

[52] Bai, C., and Gosman, A. D., "Development of Methodology for Spray Impingement Simulation", SAE Paper No. 950283, 1995.

[53] Liu Z., et al., "Modeling Drop Drag Effects on Fuel Spray Impingement in Direct Injection Diesel Engines", SAE Paper No. 970879, pp. 1377-1390, 1997.

[54] Wang, D. M., and Watkins, A. P., "Numerical Modeling of Diesel Spray Wall Impaction Phenomena", International Journal of Heat and Fluid Flow, v 14, n 3, pp. 301-312, 1993.

[55] Gavaises, M., et al., "Modeling Wall Impaction of Diesel Sprays", International Journal of Heat and Fluid Flow, v. 17, pp. 130-138, 1996.

[56] Jin, J. D., and Borman, G. L., "A Model for Multicomponent Droplet Vaporization at High Ambient Pressures", SAE Paper No. 850264, pp. 2.483-2.493, 1986.

[57] Al-Roub, M., et al., "Near Wall Interaction in Spray Impingement", SAE Paper No. 960863, pp. 1304-1318, 1996.

[58] Stanton, D. W., and Rutland, C. J., "Modeling Fuel Film Formation and Wall Interaction in Diesel Engines", SAE Paper No. 960628, pp. 808-824, 1996.

[59] Patankar, S. V., Numerical Heat Transfer and Fluid Flow, Hemisphere Publishing Corporation, 1980.

[60] FLUENT User Manual.

[61] Morsi, S. A., and Alexander, A. J., "An Investigation of Particle Trajectories in Two-Phase Flow Systems", Journal of Fluid Mechanics, v 55, n 2, pp. 193-208, 1972.

[62] Graham, K. M., and Ramadhyani, S., "Experimental and Theoretical Studies of Mist Jet Impingement Cooling", ASME Journal of Heat Transfer, v 118, pp. 343-349, 1996.

[63] Fujimoto, H., et al., "Characteristics of a Diesel Spray Impinging on a Flat Wall", Proc. COMODIA 90, International Symposium on Diagnostics and Modeling of Combustion in I.C. Engines, Kyoto, Japan, pp. 193-198, 1990.